Diplomarbeit

Quality Assurance and Data Analysis for the Belle II Silicon-Vertex Detector

ausgeführt zum Zwecke der Erlangung des akademischen Grades eines Diplom
Ingenieurs unter der Leitung von

Doz. DI Dr. Christoph Schwanda
Institut für Hochenergiephysik

Betreuer : *DI Dr. Markus Friedl*
Institut für Hochenergiephysik

eingereicht an der Technischen Universität Wien
Fakultät für Physik

von

Lukas Bulla Bsc.

Matrikelnummer: 0627932
Pfänderweg 25
6900 Bregenz

Wien, im Winter 2016

Abstract

The Institute of High Energy Physics (HEPHY), which is a part of the Austrian Academy of Sciences (ÖAW), is participating in the Belle 2 experiment. A major objective is to develop and construct the Silicon Vertex Detector (SVD) which is an inner tracking detector of Belle II. Belle II is a highly advanced B-physics experiment and therefore requires an ingenious SVD detector which is unique in his construction and application. Thus ongoing tests for functionality and quality assurance have to be conducted. These tests comprise in-house small-scale ladder checks up to high energy particle beam tests. This master thesis is about data analysis from single ladders to fully configured telescope tests and the developed test environment. Thus the thesis contains signal analysis and first tracking tests with a fully assembled L5 ladder in the final SVD configuration at CERN-SPS as well as the development of a Ladder-Test-System (LTS). The LTS aimed at testing the functionality of the fully assembled ladder with a ^{90}Sr source. Moreover, an open CO_2 cooling device (ACBC) was developed for cooling-tests after mounting the ladders on the final setup.

Kurzfassung

Das Institut für Hochenergie Physik (HEPHY), welches Teil der Österreichischen Akademie der Wissenschaften (ÖAW) ist, beteiligt sich an dem internationalen Teilchenphysik-Experiment Belle II. Die Hauptaufgabe des HEPHY ist es den Silicon-Vertex-Detektor (SVD), welcher ein Tracking-Detektor ist, zu entwickeln und zu konstruieren. Ein an die Grenzen der B-Physik gehendes Experiment, wie Belle II, erfordert einen technisch sehr hochentwickelten und in seiner Ausführung einzigartigen Detektor. Um diesen hohen technischen Anforderungen gerecht zu werden, müssen fortlaufend Tests zur Qualität und Funktionalität durchgeführt werden. Zu diesen Tests gehören kleine lokale Ladder Überprüfungen sowie hochenergetische Teilchenstrahlen-Tests. Die Aufgabe dieser Masterarbeit war es Daten von den einzelnen Ladder-Tests, bis hin zu Teleskop-Messungen bei der voll bestückten Ladder am Cern-SPS zu analysieren und erste Tracking-Tests durchzuführen. Außerdem war die Aufgabe ein Ladder Test System (LTS) zu entwickeln, das die ganze Ladder auf ihre physikalische Funktionalität mit einer ^{90}Sr Quelle testet. Des Weiteren wurde ein offenes CO_2 Kühlsystem, welches während der Montage der Ladders gebraucht wird, entwickelt und gebaut.

Contents

Contents

1 Belle II

1.1 Introduction

The Belle II experiment is an upgrade of the former Belle Experiment.It is located at the KEK(High Energy Accelerator Research Organization) in Tuskuba Japan. Belle has been running for ten years and collected about 772 million B meson decays while investigating CP-Violation. The experiment was operated at the KEKB(KEK-B-Factory) which was an asymmetric e^- e^+ particle-collider. KEKB consists of two storage rings, LER(Low-Energy-Ring) and HER(High-Energy-Ring) which accelerates electrons and positrons up to 3,5 GeV and 8 GeV. The length of each storage ring is 3016 m and has only one intersection point. KEKB is a B-Factory due to the e^-e^+ annihilation at $\Upsilon(4S)$ resonance (10.58 GeV). The Belle achievements and discoveries during the Belle lifetime have been breakthrough successes:

- Observation of the CP-Violation in B-Meson Systems

- Observation of $B \to Kl^+l^-$ and $b \to d\gamma$ and other Penguin decays

- Measurement of the CKM quark mixing matrix elements $|V_{ub}|$ and $|V_{cb}|$

- Luminosity record of $2 * 10^{34} cm^{-2}s^{-1}$ with KEKB

In addition the physicists Kobayashi and Masukawa [21] were awarded with the Nobel prize for their work about the Charged Parity Violation (CPV) including the Cabibbo-Kobayashi-Maskawa-Matrix (CKM-Matrix V_{CKM}) and their prediction of a 3rd generation of Quarks. As a consequence the Japanese government agreed to upgrade Belle to Belle II. The upgrades include SuperKEKB, an improved version of KEKB. The SuperKEKB is a next generation positron electron collider which is based on the idea of a super B factory with acceleration energies of 4GeV and 7GeV [2]. That means that because of the high density of the colliding particle bunches, caused by the very small beam cross section (nano beam), the B mesons pairs are produced in incredibly large numbers. The aim is to get a target luminosity of $8 * 10^{35} cm^{-2}s^{-1}$ which is 40 times higher than the highest reached luminosity of the former BELLE accelerator KEKB. In order to handle the higher luminosity accordingly, the Belle II detector is being built. The BELLE II detector consists of:

- two layers of pixelated silicon sensors (PXD) and four layers of double sided silicon strip sensors (SVD) that measure decay vertex positions of B-mesons and other particles

- a central drift chamber (CDC) that measures trajectories, momenta and dE/dx information of charged particles

- a barrel-shaped array of Time-Of-Propagation (TOP) counters that reconstruct, in spatial and time coordinates, the ring-image of Cherenkov light cones emitted from charged particles passing through quartz radiator bars, another ring-imaging Cherenkov counter with aerogel radiator in the forward end-cap (A-RICH)

- an electromagnetic calorimeter (ECL) comprised of scintillator crystals located inside a superconducting solenoid coil that provides a 1.5 Tesla magnetic field

- an iron flux-return located outside of the coil which is instrumented to detect K0L mesons and to identify muons (KLM)

1.2 Physics at Belle II

1.2.1 Motivation

The most famous theories of the origin of the universe is the Big Bang Theory. The theory proceeds from the assumption that 13.8 billion years ago matter, space and time emerged from a singularity. After a short time, called inflation (10^{-35}s), of exponential growth, the universe existed of quark-gluon plasma and some other elementary particles of extreme densities and temperatures. During this short period of time a process, which is not fully understood, called baryogenesis took place and caused an asymmetry in baryons and anti baryons produced in that state of the early universe. The possible follow up of this asymmetry results in the matter dominated universe as we know it today. Andrei Sakharov proposed 3 conditions[26] for the matter domination in the universe:

- **Baryon number violation** which is satisfied by theories that unify strong- and elctro-weak-interaction

- **Thermodynamic imbalance** which if not given would reverse the asymmetry between baryon and anti-baryon

- **Violation of C- (Charge)** and P- (Parity) symmetry (Charge-parity)

All three conditions are necessary to explain a dynamic asymmetry between matter and anti-matter annihilation. For this reason they have to be examined and verified by modern physics. the CP Violation especial is subject to many particle physics experiments as well as in Belle II. In order to understand the CP-violation, however, we need to take a closer look into fundamental interactions.

1.2.2 A brief digression to fundamental forces

In particle physics, as far as known, there are four fundamental forces in nature which describe the way particles interact with each other. Each force is specified by its own theory and has its own characteristics. Therefore, it is necessary to introduce the Quantum Field theory and the Lagrange formalism, the basic task of which is to express functions in space and time (e.g. $\phi_i(x, y, z, t)$). Whereby latter is a function of the coordinates q_i and their t derivatives q_i'.

Gravitational forces classical theory is Newtons law. It is based on the attraction of masses. The relativistic alternative to Newtons law is Einstein's general theory of relativity. In particle physics it is mostly irrelevant because it is too weak and thus not taken into account.

Electromagnetic Fundamental Force describes the interaction between charged particles and all its containing phenomena such as electric and magnetic fields. In the classical way it is characterized by the Maxwell-equations[22] which - combined with the theory of relativity - is called electrodynamics. When it comes to elementary particles the electrodynamic potentials are treated as field operators which can create or annihilate Photons. Photons are the mediating particles in this interaction. The very theory is called Quantum Electrodynamics and is one of the most verified theories in particle physics. All quantum electrodynamics processes are referable to a fundamental vertex and its interacting Lagrangian (eq. 1.1). This is an interaction of the Dirac-spinors, e^- and the $\hat{A}_\mu(x)$ vector field operator or gauge field. The latter acts as the four-vector-potential of the classical field and as an operator of the photon. This yields to the Lagrange density (eq. 1.2) which characterizes the QED interaction.

$$\mathcal{L}_{QED} = \bar{\psi}(i\gamma^\mu D_\mu - m)\psi - \frac{1}{4}F_{\mu\nu}F^{\mu\nu} \tag{1.1}$$

$$\mathcal{L}_{INT} = \sum_j Q_j e\hat{\bar{\psi}}_j(x)\gamma^\mu \hat{A}_\mu(x)\hat{\psi}_j(x) \tag{1.2}$$

$\hat{\psi}$ are the spin 1/2 Dirac-spinors, Q represents coupling constant in the case of a vertex (figure 1.2) it is the electric charge of the particle. γ_μ is the gamma matrix.

It has to be mentioned that at a QED-vertex the type of the spin 1/2 particle is conserved. If a spin 0 particle interacts with a photon there are 2 vertices which specify the interaction.

Strong interaction force explains how hardrons (Bayrons, Mesons) are holding together. Its descriptive theory is Quantum-Chromo-Dynamic (QCD). The idea is that hadron consist of quarks-, three of which are in Baryons, two in Mesons and all can interact. Each quark carries a special type of charge which is interpreted as colors (r,g,b) and which also has six different flavors that are not distinguished by QCD. Quarks interact via gluons, which is gauge boson, carrying -both color and anti-color and changing the color charge of quarks and of other gluons. This yields to the Lagrangian of the QCD:
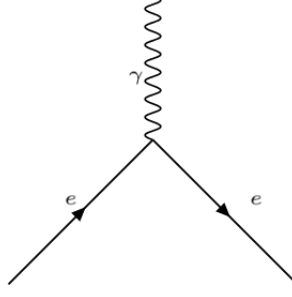
Figure 1.1: Fundamental QED-vertex

$$\mathcal{L}_{\text{QCD}}(q, A) = \bar{q}\left(i\gamma^{\mu}D_{\mu} - m\right)q - \frac{1}{4}F^{a}_{\mu\nu}F^{\mu\nu}_{a} \tag{1.3}$$

The three fundamental Vertices of QCD reveal that the glouns can interact with each other.
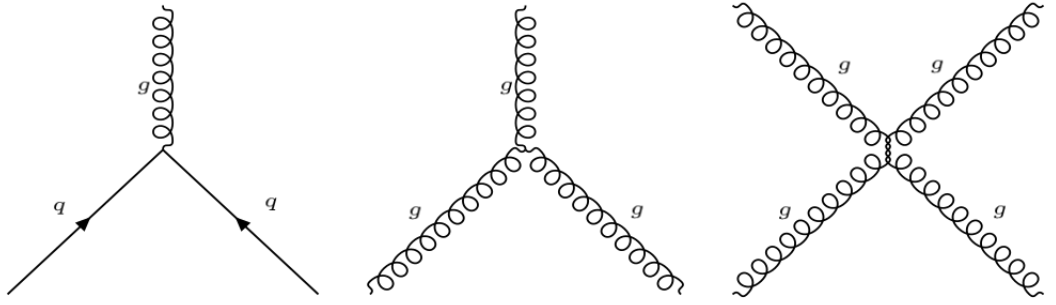

Figure 1.2: Fundamental QCD-vertex

Weak force is mainly recognizable in transmutation or decays. Leptons for example do not have a color charge thus they do not take part in the QCD. Neutrinos do not have any charge so they do not participate in QED but they all join in the weak interactions. As in the QED and QCD the weak force interacts via gauge bosons. In particular there are two different types of interactions called neutral and charged interaction (current). They are mediated by Z- (neutral) and the W-boson (charged). Neutral currents do not changes the flavor of any quark or lepton (f). An example is the neutrino- proton scattering $(\nu_{\mu} + p \rightarrow \nu_{\mu} + p)$. The charged current however change the flavor but keeps the generation of leptons(e.g. e^{-}converts to μ_{e}). An example for charged currents is the decay of a myon $(\mu^{-} \rightarrow e^{-} + \nu_{\mu} + \bar{\nu}_{e})$. In the Standard-model the weak and the electromagnetic forces are represented as two different aspects of one combined force,the Electroweak-force. The descriptive formalism of Electroweak-interactions is the Glashow, Salam and Weinberg model [18] which unifies weak and electromagnetic interactions.
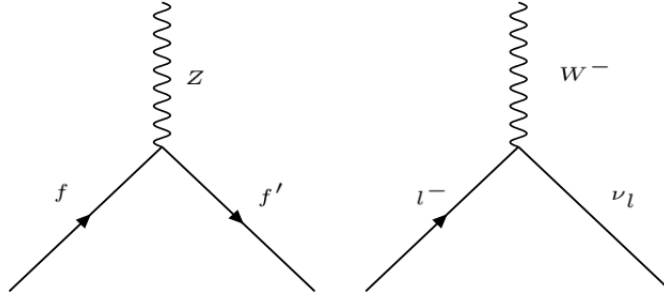
Figure 1.3: Fundamental Weak interaction vertices

Force	Relative Strength	Range
Strong (nuclear)	1	$10^{-15}m$
Weak (radioactive decay)	10^{-6}	$10^{-18}m$
Electromagnetic	$\alpha(10^{-2})$	infinite
Gravitational	10^{-38}	infinite

Table 1.1: Fundamental forces

1.2.3 Standard-Model

The Standard-model unifies three of the four fundamental forces mentioned in 1.2.2 which are the electro-, weak- and strong force(GCD) by combining their gauge field theories. As it combines gauge-field theories the SM itself is also a gauge-field theory. A gauge theory can be defined as covariant derivative from which a field strength tensor can be generated. With the field tensor a Lagrangian-density and further action can be defined. Through Variational-methods also the equation of motion and conserved quantities are determined. The SM combines two of these called gauge- or symmetry groups (tab 1.2), and as far as modern physic can tell, the SM describes all particles and their corespondent gauge bosons(fig 1.4). Even the spontaneous symmetry breaking which leads to the Higgs-mechanism is respected. But that is not the end of the rope there are many open questions such as, how to include gravity, the masses of neutrinos, dark matter and so on, which cannot be explained by the Standard-model. A popular visualization of the SMś fundamental particles is shown in figure 1.2.3. The generations are separated by the first three columns. The flavors of Quarks (purple) and leptons (green) flavors are separated by rows. The fourth column present the corresponding gauge bosons. Hence the SM counts $6 \times 2 = 12$ leptons (with antiparticles), $6 \times 2 \times 3 = 36$ quark (including 3 colors and antiparticles), four electroweak mediating bosons($\gamma, Z, W^{\pm}$) and eight strong force mediating gluons ($N^2 - 1; SU(3)$).

1.2.4 Symmetries and conservations laws

In particle physics there are two important symmetry transformation groups called global and local. While global symmetries consider all values in spacetime, the values for local

Group name	Properties
$SU(3)_c$	Strong Interactions, c refers to the "color" coupling
$SU(2)_I \times U(1)_Y$	Electroweak Interactions, I and Y refers to the Isospin and Hyper-charge

<div align="center">Table 1.2: symmetry groups included in the Standard-model</div>
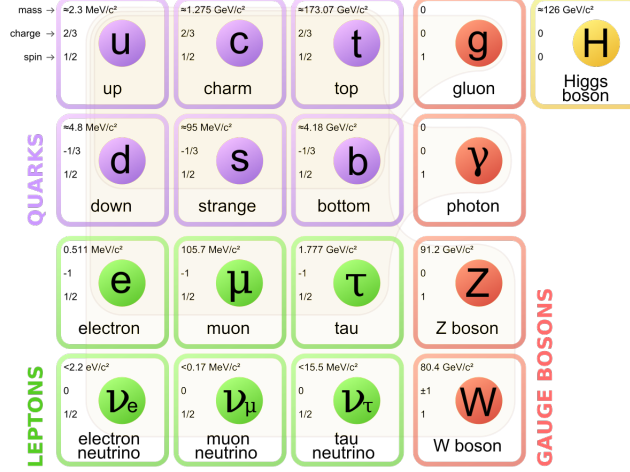

<div align="center">Figure 1.4: Standard Model of Elementary Particles [23]</div>

symmetries varies. Local transformations are the foundation of the gauge theory and are therefore responsible for the characterization of all fundamental interaction. An important requirement for the gauge theory is that the local transformation is invariant. Thus the Lagrangian has to fulfill this requirement as well. An example for the impact of the local invariance (e.g. U(1)) is the generation of the Lagrangian QED interaction term (eq. 1.2). Furthermore these transformations exist under symmetry groups which are continuous or discrete.

Continuous Symmetries

The Noether-Theorem [25] says, every continuous symmetry leads to a conservation law that has a conserved quantity. As regards the Lorenz-transformation, a space time transformation, its conservation values are energy and momentum. Some continuous symmetries and their corresponding conservation values are well known. For example the total momentum is constant for a closed system. Therefore, the total momentum is the conservation value for translations. Continuous symmetries have unlimited numbers of symmetric operations. A list of known symmetry groups is presented in table 1.4.

Discrete Symmetries

As seen continuous symmetries are important in the field theory, but there are also discrete symmetries such as Parity. Parity transformation of the position vector $\vec{r}$ to $-\vec{r}$

Group name	Dimension	Characteristics
$U(n)$	$n \times n$	unitary
$SU(n)$	$n \times n$	unitary, determinant 1

Table 1.3: symmetry groups

Conserved Quantity	theory	groups
Lepton number (L)	QED,QCD,GWS	$U(1)$
Baryon number (B)	QED,QCD,GWS	$SU(3)$
Flavor	QCD	$SU(3)$
Isospin (I_3)	QED,QCD	$SU(2)$
Hyper-charge (Y)	QCD	$U(1)$

Table 1.4: continuous symmetries and their conserved quantities

$((t, x, y, z) \rightarrow (t, -x, -y, -z))$. These symmetries picture non continuous changes of a system. That also leads to multiplicative instead of additive quantum numbers similar to continuous symmetries. Table 1.5 lists important discrete symmetries.

Conserved Quantity	theory	groups
Parity (P)	QED,QCD	$SU(3) \times U(1)$
charge (C)	QED,QCD,GWS	$SU(3) \times SU(2) \times U(1)$
Time reversal	QED,QCD	$SU(2)$

Table 1.5: Discrete symmetries and their conserved quantities

A special characteristic of the weak force is to violate the global symmetries of the QCD and the QED. For example charge and parity are not invariant with the weak interaction. Parity is maximally violated by the weak force which was discovered by Wu-experiment [32].C also is violated by the weak force. That can be shown with neutrinos, when a left-handed conjugated neutrino charge turns into a left-handed anti-neutrino, which does not exist.

1.2.5 CP symmetry and its violation

As mentioned in 1.2.2 charged weak interactions do not change the generation of leptons. When it comes to coupling $W^{\pm}$ to quarks, the behavior is different (e.g. semileptonic decay $\overline{K}^0 \rightarrow \pi^+ + \mu^- + \overline{\nu}_\mu$). Therefore, Cabbibo [8] introduced new weak- (d',s')instead of the flavor eigenstates (d,s). The weak eigenstates are superpositions of the flavor eigenstates and rotated by the angle $\theta_C = 13, 15°$.

$$\begin{pmatrix} d' \\ s' \end{pmatrix} = \begin{pmatrix} cos\theta_C & sin\theta_c \\ -sin\theta_C & cos\theta_C \end{pmatrix} \begin{pmatrix} d \\ s \end{pmatrix} \tag{1.4}$$

Kobayashi and Maskawa [21] expanded this model, to three generations of quarks, to explain the CP violation found in neutral kaon decays and attributed that to the quark

sector. Hence there is a 3×3 matrix needed with the complex phase ϕ which is the CP violating phase. This is justified because ϕ is the only complex phase in the SM Lagrangian and therefore the only source of CP-Violation.

$$\begin{pmatrix} u \\ d' \end{pmatrix}, \begin{pmatrix} c \\ s' \end{pmatrix}, \begin{pmatrix} t \\ b' \end{pmatrix} \tag{1.5}$$

$$\begin{pmatrix} d' \\ s' \\ b' \end{pmatrix} = \underbrace{\begin{pmatrix} V_{ud} & V_{us} & V_{ub} \\ V_{cd} & V_{cs} & V_{cb} \\ V_{td} & V_{ts} & V_{tb} \end{pmatrix}}_{V_{CKM}} \begin{pmatrix} d \\ s \\ b \end{pmatrix} \tag{1.6}$$

$$V_{CKM} = \begin{pmatrix} 1 & 0 & 0 \\ 0 & c_{23} & s_{23} \\ 0 & -s_{23} & c_{23} \end{pmatrix} \begin{pmatrix} c_{13} & 0 & s_{13}e^{-i\phi} \\ 0 & 1 & 0 \\ -s_{13}e^{i\phi} & 0 & c_{13} \end{pmatrix} \begin{pmatrix} c_{12} & s_{12} & 0 \\ -s_{12} & c_{12} & 0 \\ 0 & 0 & 1 \end{pmatrix} \tag{1.7}$$

$$c_{ij} = cos(\theta_{ij}), s_{ij} = sin(\theta_{ij}), \theta_{12} = \theta_C \tag{1.8}$$

$$V_{ud}V_{ub}^* + V_{cd}V_{cb}^* + V_{td}V_{tb}^* \tag{1.9}$$

$$V_{CKM} = \begin{pmatrix} 1\frac{\lambda^2}{2} & \lambda & A\lambda^3(\rho - i\eta) \\ -\lambda & 1\frac{\lambda^2}{2} & A\lambda^2 \\ A\lambda^3(1 - \rho - i\eta) & -A\lambda^2 & 1 \end{pmatrix} + O(\lambda^4) \tag{1.10}$$

Moreover, the V_{CKM} matrix is a unitary ($V_{CKM} * V_{CKM}^\dagger = 1$) and with the relation 1.9 one obtains a unitary triangle in the complex plane. To represent the triangle in the complex plane the measured values of V_{CKM} are expressed in the Wolfenstein parametrization [31] (see 1.10). This is an approximation of the standard parametrization (see 1.7) to the order λ^3. All four parameters (A,λ, η and ρ) are real.
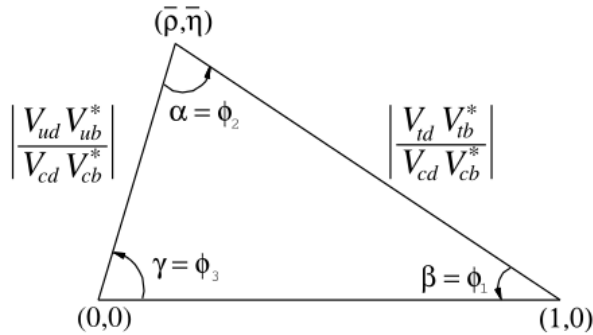

Figure 1.5: Unitary triangle [5]
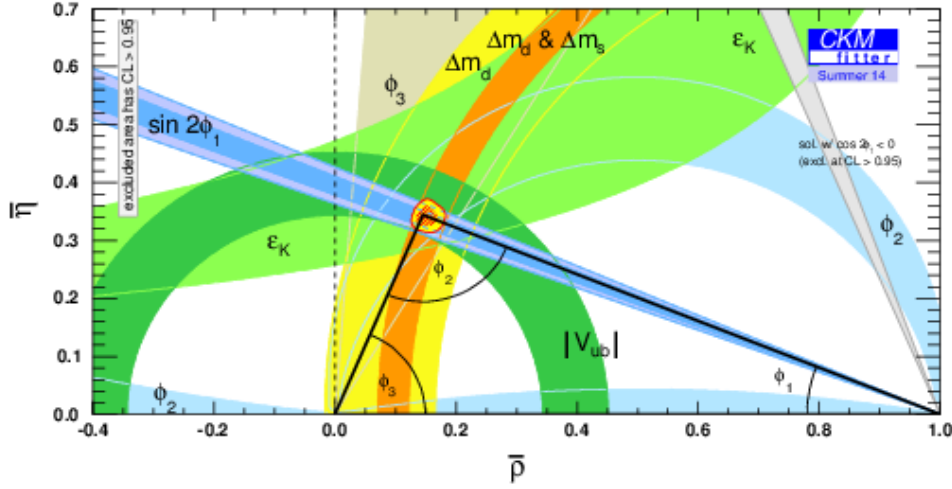
Figure 1.6: The global CKM fit in the small (ρ-bar,η-bar) plane ;with ϕ_1, ϕ_2, ϕ_3 convention [10]

Measuring CP-Violation

There are many possibilities to measure CP-violation in B meson system. To exemplify one process, this thesis will examine the $\overline{B} - B$ mixing and time-dependent CP asymmetry. This method was already used at Belle to show CP-violation and define the parameter ϕ_1 of the CKM-matrix. At KEKB the collision of e^+ and e^- at a resonance of $\Upsilon(4S)$ a pair of entangled $B_0\overline{B_0}$ were produced. As known for entangled particles pairs, if the state of one particle is measured the state of the others is known as well but with different decay rates Δt. Hence the initial state of $\overline{B_0}$ or B_0 is known it oscillates between the states $\overline{B_0}$ and B_0, with the frequency Δm, till the resulting final state of the decay mode $B_0 \rightarrow \frac{J}{\psi} K_s$ is measured (figure 1.7) at the time difference Δt. Thus the ratio A_{cp} is given and therefore the angle $S = \zeta_{CP} sin(2\phi)$, as $\zeta_{CP} = \pm 1$ is the eigenvalue of CP. Of course there are also options to measure directly instead of indirect Cp-violation. An example would be the $B \rightarrow \pi\pi$ decay.

$$A_{cp} = \frac{\Gamma(\overline{B_0} \rightarrow \frac{J}{\psi}K_s) - \Gamma(B_0 \rightarrow \frac{J}{\psi}K_s)}{\Gamma(\overline{B_0} \rightarrow \frac{J}{\psi}K_s) + \Gamma(B_0 \rightarrow \frac{J}{\psi}K_s)}$$
$$= \underbrace{Ssin(\Delta m\Delta t)}_{mixing\ CP\neq 0} + \underbrace{Acos(\Delta m\Delta t)}_{direct\ CP=0} \tag{1.11}$$

Outlook CP-Violations at SuperKEKB

A fascinating fact is that all CP violating effects of the SM are based on the Kobayashi-Maskawa mechanism [21], which leads to only one complex phase in the CKM-matrix. All measured observables which violate CP have been consistent with this theory [24]
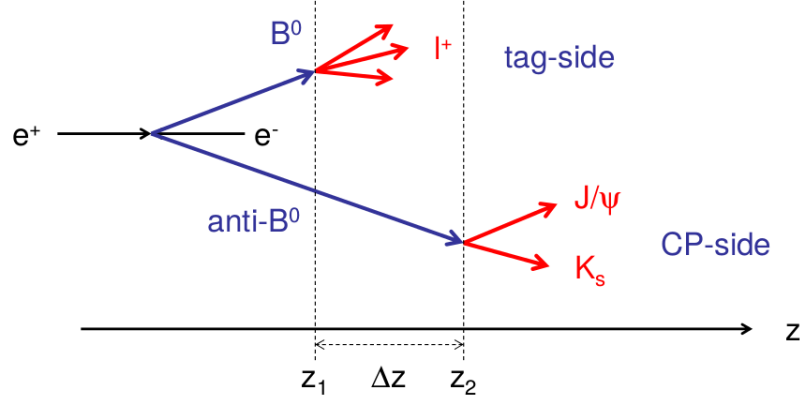
Figure 1.7: $\Delta t = \frac{\Delta z}{\beta \gamma c}$, with $\beta\gamma = 0.28$ at super KEKB [5]

so far. Therefore, the CKM-matrix and its parameter will have a large share in research at Belle II. The $B \to \pi\pi^-$ decay will also be used at Belle II to determine the angle ϕ_2 of the unitary matrix. Therefore, the time-dependent CP-violating parameter of $b \to u\overline{u}d$ decay transitions will be measured. To examine ϕ_2 also $B \to \rho\pi$ and $B \to \rho\rho$ decays can be used, but this thesis will not further evaluate the issue. The predictions of the measurement error for ϕ_2 at a luminosity of $50ab^{-1}$ of the super KEKB are $< 1°$. The angle ϕ_3 is determined through CP phases at D meson intermediate states by measuring interference of decay amplitudes at, for example $B^- \to D^0 K^-$ followed by $D^0 \to K^+ + \pi^-$ and $B^- \to \overline{D_0}K^-$ followed by $\overline{D_0} \to K^+ + \pi^-$. With a combination of analyzing methods the expected error for ϕ_3 at $50ab^{-1}$ is 1,5°. There are a lot more decays which are interesting for proving the SM or revealing new physics but this thesis shall not go into any more detail. For a more extensive elaboration see [3] [5].

1.3 Belle II Sub-Detectors

The Belle II detector consists of many sub detectors which all play their part in the common goal to detect and identify elementary particles and their decays. As shown in figure 1.8 the whole Belle II detector houses components that reach from innermost Interaction-Point chamber to the utmost K_L and Myon detector (KLM). The subsystems will be briefly elucidated in the following sections.

1.3.1 IP Chamber

The interaction-point chamber is the innermost part of the Belle II detector. In this part the two particle spills of the 7GeV electron high-energy ring (HER) and the 4GeV positron low-energy ring collide. The crossing angle of the spills is 83 mrad which helps to place the final focusing quadrupole magnets closer to the IP. The chamber is vacuumed and has a complex system of five superconducting quadrupoles, three permanent quadrupoles, two superconducting compensation solenoids and 32 superconducting cor-
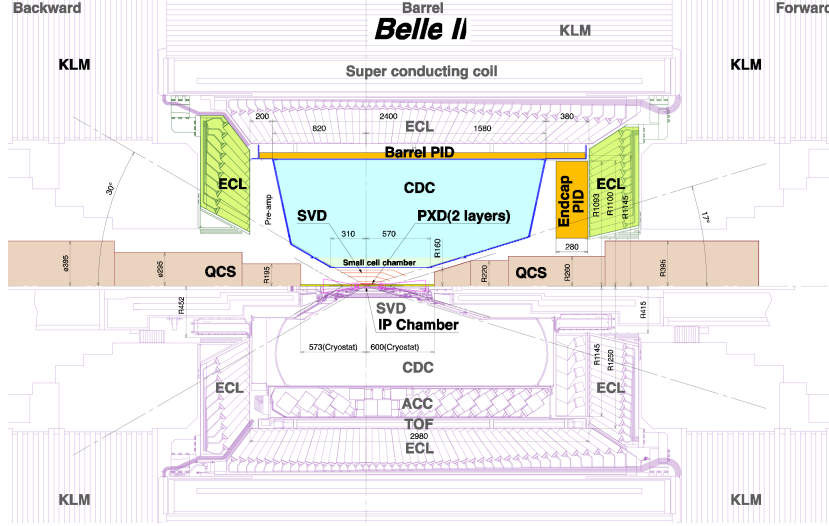
Figure 1.8: Upper part of the picture shows the Belle II Detector; Lower part shows the
previous Belle Detector [2]

rector coils to focus the two beams [2]. The compensation solenoids are aligned in their
field axis to neutralize the 1.5 T field of the of the Belle II solenoid. The radius of the
chamber at the IP is 10 mm which is very small and therefore good for vertex recon-
struction. The central part of the IP chamber is made of beryllium which due to its
atomic number (Z=4) has low scattering effects. The side parts are made of tantalum
to shield against particle shower background.

1.3.2 PXD

The pixel detector (PXD) is the inmost sub detector of Belle II. It is used for tracking
the vertices closest to the IP chamber. The small radius of the IP chamber brings the
problem of extremely high number of events at the desired luminosity close to chamber
radius. Therefore, a special kind of pixel detector (PXD) is used which fulfills the re-
quirements of handling high occupancy and has a thickness that does not tamper the
measurement. The depleted field effect transistor (DEPFET) detector is a semicon-
ductor detector which satisfies the requirements. The DEPFET technology combines
junction field effect transistor (JFET) with a silicon detector substrate, thus amplifier
and detector are combined in one device as shown in figure 1.9a. The "internal gate"
collects the electrons resulting from the external radiation and influences the gate of the
FET depending on the collected charge. The advantage of the DEPFET is that it is
possible to read out the internal gate information multiple times. To clear the DEPFET
gate a "clear FET" is integrated to drain the internal gate. Hence many DEPFETs
arranged in a matrix form the pixel detector (figure 1.9b).

The PXD has two layers of pixel senors with the radial distance to the interaction
point of 14 mm and 22 mm. The half ladders are split into regions by the interaction
point with different pitches and sizes (table 1.6). Since the charge induced by hits does
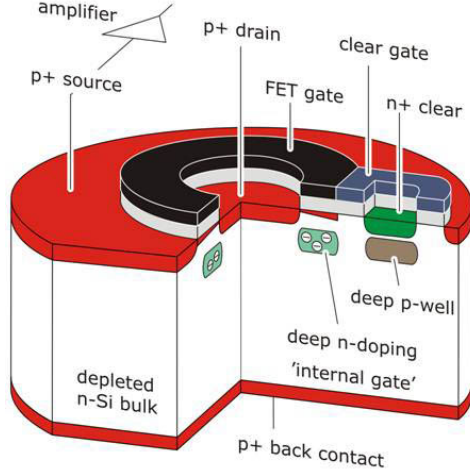
(a) DEPFET structure
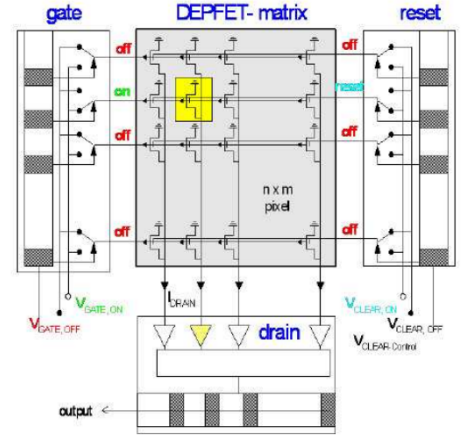
(b) DEPFET matrix with redout control

Figure 1.9: Pixel detector [2]

not spread over too many pixels it results in a better track reconstruction accuracy. The estimated spatial resolution for the Belle II pixel detector is 8 μm [2].

	inner Layer	**outer Layer**
radii	13 mm	22 mm
# of modules	8	12
# of pixels	768 x 250	768 x 250
total pixels	3.072 M	4.608 M
pixel size (reg1)	$55x50\mu m^2$	$70x50\mu m^2$
pixel size (reg2)	$60x50\mu m^2$	$85x50\mu m^2$
sensitive area	$44.8x12.5 \ \mu m^2$	$61.44x12.5\mu m^2$

Table 1.6: PXD ladder quantities

1.3.3 SVD

The silicon vertex detector is a four layer vertex tracking detector next to the PXD as shown in figure 1.8. This subdetector will be discussed in section 1.4

1.3.4 CDC

The central drift chamber(CDC) is a gas chamber detector. The basic function principle is that a charged particle ionizes a gas while passing the gas filled drift chamber. Inside the chamber are taut wires with positive and negative potentials. Nine wires are combined as a cell. Each cell has eight field wires with negative and one sense wire with positive potential. The electrons of the ionized gas drift to the sense wires along the

traversed charged particle marking a two dimensional track. To get a more accurate position the drift time of the electrons from the ionizing point is also being taking into account. The result are circles with the sense wire in the center and the radius of the ionizing point. Each particle track has to be a tangent to this circle. Therefore, combining all the tangents of the sense wire circles lead to the two dimensional track. To get the coordinate in the third dimension there are two different layers of cells. In the axial layers the cells are parallel to the beam direction. In the stereo layer the cells are with a stereo angle to axial cells. With the combination of axial and stereo layer it is possible to reconstruct a three dimensional track. Because of the external 1.5 T field the traversing charged particles are forced into a helix track which makes it suitable to determine the momentum. With this knowledge of the particle tracks we come to the two major tasks of the drift chamber to accomplish in the Belle II detector: The first is the measurement of the momentum of charged particles, the second is to provide trigger signals (level 1) for event recording. The key data of the CDC are summarized in table 1.7.

Radius of inner cylinder	160mm
Radius of outer cylinder	1130mm
# of layers	56
# of sense wires	14336
Gas	$He - C_2H_6$

Table 1.7: CDC quantities

1.3.5 TOP

The time of propagation (TOP) sub detector is a Cherenkov detector set on top of the central drift chamber (figure 1.8). Its purpose is particle identification in the barrel region and therefore it is part of the particle identification system (PID). The TOP detector uses 16 modules placed as an arc around the central drift chamber. Each module consists of two quartz bars with 2.5 m length, an expansion prism with photo arrays at the backward and a mirror at the forward end(1.10a). When a charged particle traverse the quartz bars of module, Cherenkov light is emitted with the angle θ_c. The emitted photons are reflected inside the quartz bars until they find their way to the photo arrays via the expansion prism (1.10b). A photo array consists of 32 Micro Channel Plate Photomultiplier Tubes (MCP-PMT). Each MCP has a 4 x 4 active region with total 512 channels per module to detect each photons position and time of arrival. Since each particle emits photons with θ_c, depending on the velocity or mass with the given track parameters, it is possible to construct a Cherenkov ring image. The ring image can be displayed by plotting the position versus time and is used to identify the different particles.
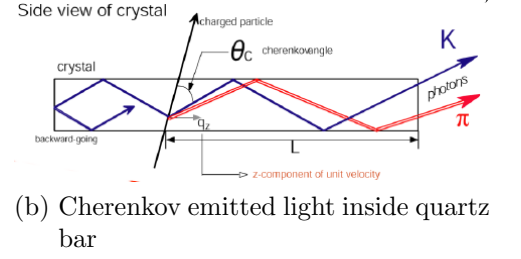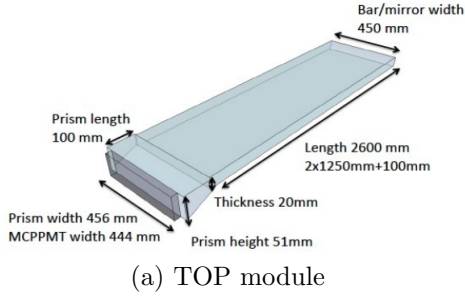
(a) TOP module

(b) Cherenkov emitted light inside quartz bar

Figure 1.10: TOP detector [2] [19]

1.3.6 ARICH

Like the TOP the Aerogel Ring Imaging Cherenkov sub detector uses the θ_c for particle identification. It is positioned at the forward end cap direction of the CDC. For the Belle II experiment it is very important to cover particle identification in forward direction due to asymmetric acceleration of SuperKEKB and the resulting forward boost. The RICH setting uses a focusing aerogel radiator consisting of 2 cm thick layers made of highly transparent hydrophobic silica aerogel and refractive indexes of $n_1 = 1.055$ and $n_2 = 1.065$ [2]. After the radiator an expansion volume allows the photons to form Cherenkov rings which are recorded by a hybrid avalanche photo-detector (HADP) (figure 1.11). The whole front end cap is covered with 420 HADP each with 144 readout channels. The most significant task of both the TOP and ARICH is the improve the $K and \pi$ separation.
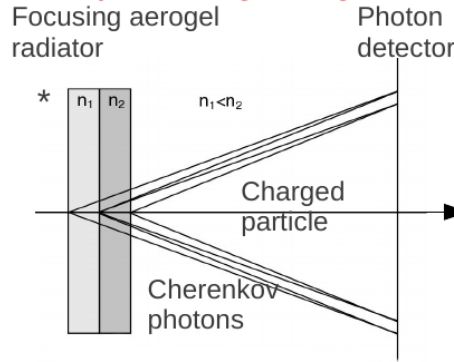

Figure 1.11: ARICH function principle [2]

1.3.7 ECL

The electromagnetic calorimeter is basically the same as used for Belle. CsI(Tl) crystals (figure 1.12a) are used throughout the ECL. Compared to Belle the challenge is to the reduce the noise pileup caused by beam background incidents. Therefore, the electronic

readout is replaced by a sampling waveform readout to get energy and timing. The detector is covered with 8736 crystals as shown in figure 1.12b [2]. In the future it is planned to replace the forward CsI(Tl) with pure CsI crystals to further reduce the noise pileup. The purpose of the ECL is to detect photons which are provided by many B-decays by position and energy. Furthermore the ECL delivers a level 1 trigger for Belle II.
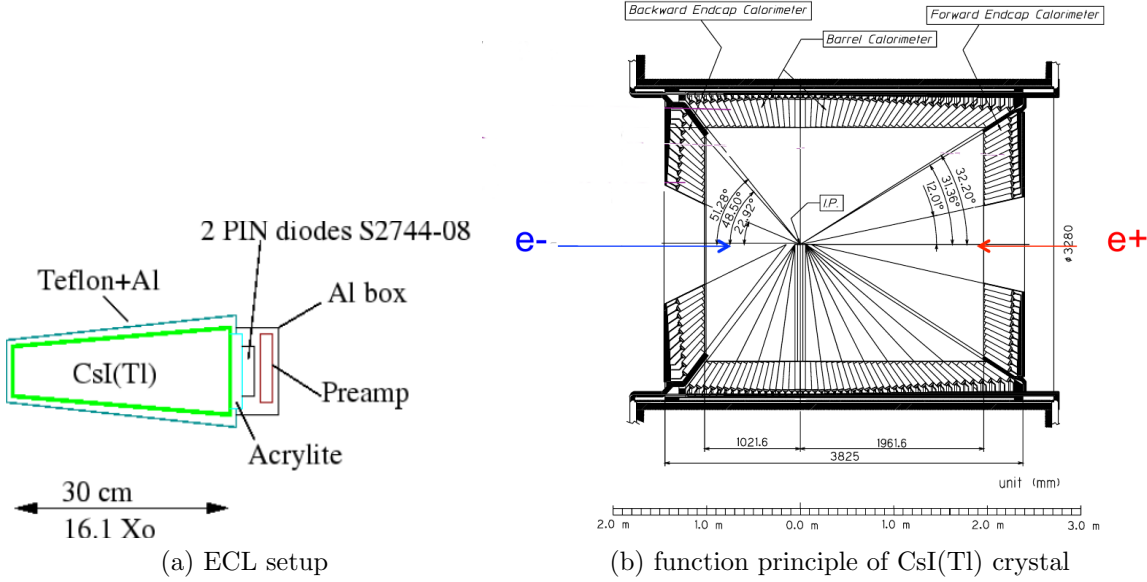

(a) ECL setup

(b) function principle of CsI(Tl) crystal

Figure 1.12: Electromagnetic calorimeter [1]

1.3.8 Iron Yoke and Solenoid Magnet

The previous illustrated sub detectors are coated by the iron yoke and the soleniod magnet. The superconducting solenoid magnet with a diameter of 3.4m and a cylinder volume provide a 1.5 T homogenous magnetic field. The iron yoke acts as feedback path of the magnetic flux of the magnet. It is also an absorber for the KLM and a support for the structure of the detectors.

1.3.9 KLM

The K_L and μ detector (KLM) is a sampling calorimeter (figure 1.8). Its made of 15 alternated layers of iron and resistive plate chambers(RPC) at the barrel and 14 at the end caps. The active detector elements are glass electrode RPCs. Except the end cap RPCs are replaced with scintillators due to the increased background of the SuperKEKB. The function of the KLM is to identify muons and kaons. Muons are identified by extrapolating tracks to hit candidates. Hence it is possible to cluster the hits, also K_L^0 kaons can be identified. It should be mentioned that the clusters only

have information about the direction, not the energy. The resolution can be improved by comparison of nearby ECL clusters. The KLM also provides a trigger signal from muons for calibration and configuration.

1.4 Silicon Vertex Detector

The silicon vertex detector (SVD) is a double sided silicon strip detector (DSSD). Its main purpose together with the PXD is to measure and track B meson decay vertices. Vertices of other decays, such as D-mesons and τ-leptons, are traced additionally. The SVD also helps the PXD to reduce the background by defining a region of interest (ROI) for hit candidates. The vertex tracing devices PXD and SVD of Belle II compared to Belle had to be redesigned and replaced completely. Due to the smaller difference of collision energies the Lorentz boost factor of the center of mass system shifted from $\beta\gamma = 0.425$ to $\beta\gamma = 0.28$, which means less separation of the B vertices. Furthermore the increased luminosity leads to a 30 times larger beam background and a 30 kHz trigger rate [2] that brings a higher occupancy and requires faster readout.

1.4.1 SVD structure

The detector has the shape of a barrel with four different layers. The layers have different radii and length getting smaller from the outermost to the innermost. Each layer consists of a number of ladders (table 1.8). The ladders are the core modules of the SVD. Assembled with 5 to 2 sensors per ladder covering from 17° to 150° of the polar angle. Two terms are influencing the layout as it is: Firstly, to avoid any kind of contact of ladders with its neighbors the ladders are tilt. Secondly, the detector will be in a 1.5 T homogenous magnetic field which deflects, by Lorentz force, the electron/hole pairs (e-h pairs) from the track of the particle, which is their point of origin, the tilt angle of the ladders reduces this effect. Thirdly, the alignment is mostly done by high energy cosmic muons, the rates of which are little. Therefore, an overlap from 2.6 to 17.9% of the sensor area is foreseen in regard to facilitate the software alignment. Fourthly, the forward section of the ladders which is slanted and equipped with trapezoid sensors. This is done because of cost reduction otherwise if implemented parallel to the beam it would have increased the number of wafers significantly. All these pieces of the puzzle lead to the final windmill layout of the SVD shown in figure 1.13b.

Layer	Radius	Ladders	Sensor per ladder
6	135 mm	16	5
5	104 mm	12	4
4	80 mm	10	3
3	39 mm	7	2

Table 1.8: SVD ladder quantities

(a) Schematic configuration showing the three different sensor geometries and the number of APV25 readout chips for each detector.
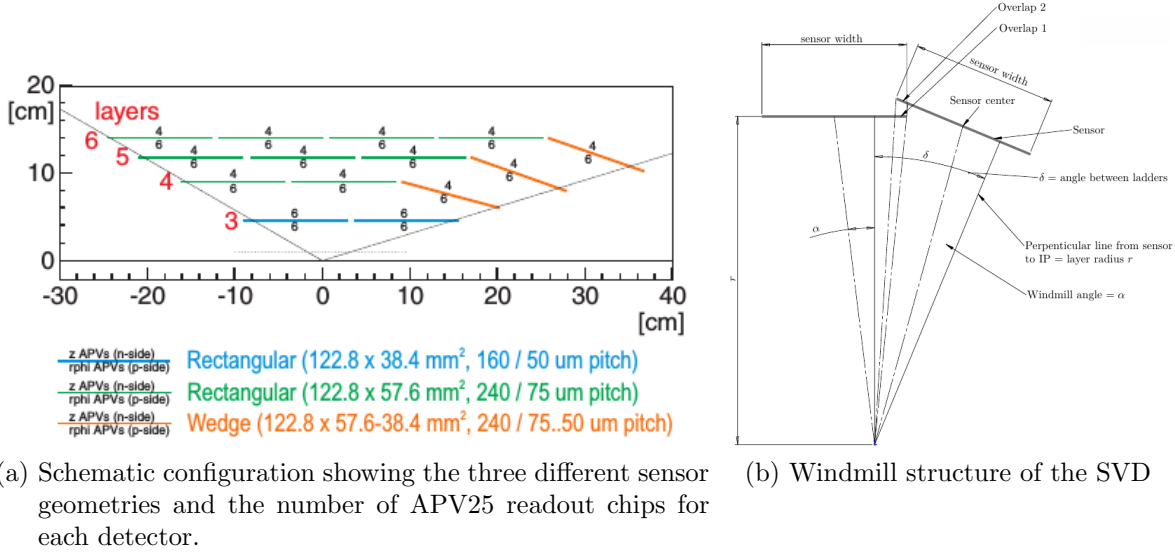
(b) Windmill structure of the SVD

Figure 1.13: SVD layout [2]

1.4.2 Readout

APV25

For readout the APV25 chip is used. This chip was originally designed for the CMS silicon tracker [12], which has the advantage of being a well tested and experienced device. It is a low noise front end preamplifier chip that satisfies the requirement of 50 ns shaping time, necessary to suppress the background from superKEKB. Hence to the radio frequency of SuperKEKB the AVP25 will operate at the frequency of $f_R/16 = 31.8Mhz$ by default. The chip has 128 input channels which when read out convert the charge into a pulse shape with an amplitude correlating with the charge. The processed values are stored in a 192 cell ring buffer. 32 cells can be marked for readout as one. Running in peak mode, the APV25 is able to store one or three shaper-pulse samples. The APV chips are mounted on PCB-hybrids (printed circuit boards). This is appropriate for the sensors on the brink of the acceptance region which are backward and the forward sensors (slanted). For the sensors inside the acceptance region, a flexible printed kapton board (Origami-flex-structure) is used that can be folded over the silicon-sensor.

Readout chain in a nutshell

The Readout chain includes the path of the particle hit information from the APV25 chip to data acquisition(DAQ) system and the monitoring software (slow control) (figure 1.14). After the signal is processed by the APV25 chip the next step is the junction box which connects the cable from the PCBs with the longer ones to the FADC (Flash Analog Digital Converter). Furthermore the power supplies are connected to junction boards. From the junction box the long cables are connected to the FADC board. The FADC board has to digitize the analog data and also process the data for further use.

48 APVs are handled by one FADC board. The data is further sent to Belle II DAQ via the finesse transmitter board (FTP). A sample of the data is diverged from the main data stream to the slow control to monitor the data taking process.[14]
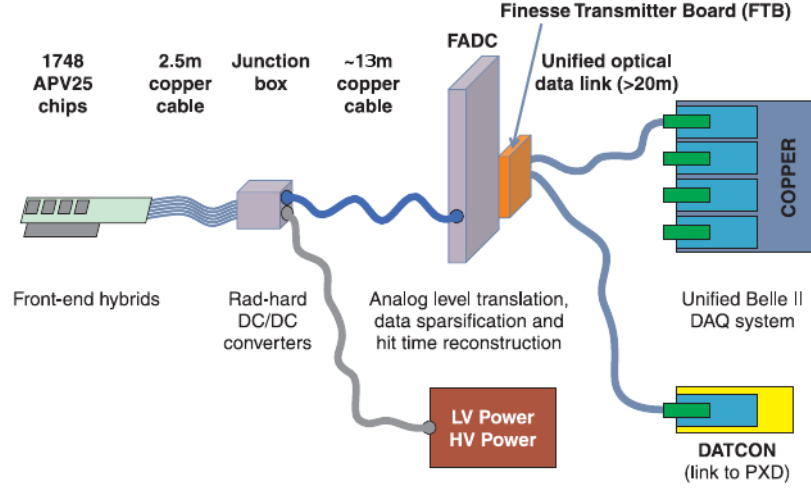

Figure 1.14: SVD readout chain

1.4.3 Double sided silicon micro strip sensors

The double sided silicon micro strip sensors are using well known semiconductor technologies. These sensors are interacting with charged particles by creating electron-hole pairs (e-h pairs). This is possible by combining n- and p-type doped materials. While "n materials" grant excess to electrons, "p materials" grant excess to electron-holes (neutral charges). When these two materials are put together, the so-called depleting region rises to a certain depth. This occurs, because of electrons moving from n-type to p-type and vice versa to a certain equilibrium. One can increase this region by applying a reversed bias. That means connecting a power source with the positive terminal at the n-type and the negative at the p type. The depleton region is so important because it is sensitive to the created e-h pairs when interacting with traversing particles. The depletion depth can be calculated with equation 1.12 [29], where ϵ is the dielectric constant and V_{FD} is the depletion voltage.

$$d_{depth} = \sqrt{\frac{2\epsilon_0\epsilon}{q_e N_{donor}} V_{FD}} \tag{1.12}$$

The depletion voltage is given by formula [4] 1.13, where p is the pitch and w is the width of the sensor strips. $f(\frac{w}{p})$ is a numerical approximation and depends on the w/p ratio.

$$V_{FD,Sensor} = V_{FD,Diode}[1 + 2\frac{p}{d}f(\frac{w}{p})] \tag{1.13}$$

The complete DSSD consists of n-strips, p-strips and n-substrate bulk. The n-strips have a lesser doping concentration than the rest of the n-bulk in such way depleting regions developing on all $n^+ - n$ and p-n junctions with different levels magnitude.The n- and p- readout strips are implemented orthogonal to each other. To make the whole n-bulk sensitive for particles, the depletion zone has to expand,that is why the reversed bias is applied. Further the reversed bias is used to force the e-h pairs to the readout strips (electrodes). The collected charges can be read out via capacitively coupled aluminum strips for further processing. The aluminum strips additionally help to get rid of some parasitic effects, for instance dark current and DC components. Hence the strips are placed above the n and p-type strips insulated by a thin oxide layer. Because of the weaker $n^+ - n$ junction a $p^+ - stop$ is implanted between the $n^+ - strips$ to force the charge carriers into the $n^+ - strips$. For the DSSD of the SVD additionally an inter strip is inserted between the actual readout strips for improving the spatial resolution. These strips read out via capacitive coupling to the neighbor strips
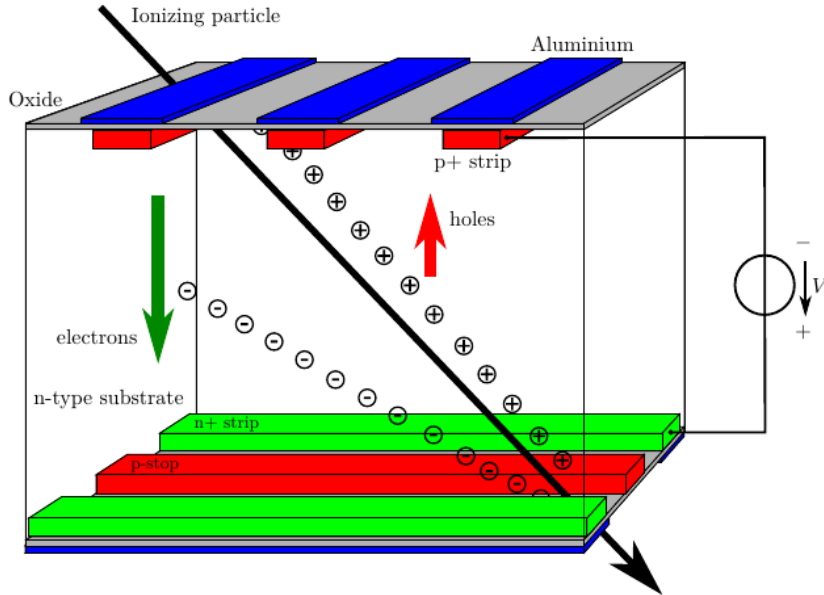

Figure 1.15: working principle of the DSSD with applied V_{FD} to collect the e-h pairs and deplete the n-bulk

The design of the sensors are similar for the Layers 4 to 6 whereas layer 3 differs in size and pitch. All sensors are made of the same geometrical forms that are rectangle and trapezoid. Specifications are shown in table 1.9 and 1.10 [2].

1.4.4 Position of traversing particles

The basic principle of calculating the position with a DSSD is quite simple. If a single horizontal strip and a single vertical strip supply a signal it is easy to calculate the position by knowing the pitch size. Nevertheless, because the traversing particle has

	Layer 4-6	Layer 3
Size (mm^2)	124.88×59.6	124.88×40.3
Active area(mm^2)	122.9×57.72	122.9×38.4
# strips p-side	768	768
# strips n-side	512	768
Pitch p-side (μm)	75	50
Pitch n-side (μm)	240	160

Table 1.9: Quantities and geometries of rectangular sensors

	Layer 4-6
Size (mm^2)	$\frac{60.63+42.02}{2} \times 125.58$
Active area(mm^2)	$\frac{57.59+38.42}{2} \times 122.76$
# strips p-side	768
# strips n-side	512
Pitch p-side (μm)	75...50
Pitch n-side (μm)	240

Table 1.10: Quantities and geometries of trapezoidal sensors

a certain incident angle and generates a charge cloud (e-h pairs) which is collected by several strips, things are quite more complex. Firstly it is necessary to define a cluster which describes how many consecutive strips are supplying a relevant signal in relation to the noise. In addition, the signal height of the relevant strips is important as well. Therefore, one can differentiate between clusters by length. For clusters with 'width equals one' the position can be calculated with the strip number multiplied with the pitch and the resulting precision is the binary resolution:

$$\sigma^2 = \frac{1}{p} \int_{-\frac{p}{2}}^{\frac{p}{2}} x^2 dx = \frac{p^2}{12}$$
$$\sigma...Resolution$$
$$p...Pitch$$

(1.14)

When it comes to cluster widths (CLW) greater than one, the position is calculated by a mean value weighted by the signal height. The condition for using this method is to have a linear spread of charges amongst the strips which results in a uniform distribution. This method is called center-of-gravity (COG)[28]:

$$x_{COG} = \frac{\sum_i x_i S_i}{\sum_i} = x_0 + p \frac{\sum_i i S_i}{\sum_i} = x_0 + p\eta$$

(1.15)

Where x_i is representing the position of the i-th strip of the cluster, S_i the corresponding strip signal. η is the position weighted by the signal. This is a sophisticated way to calculate the position which improves the resolution compared to the binary. The

Layer	Slant angle
4	11.9°
5	16°
6	21.1°

Table 1.11: Slanted angles of the trapezoidal sensors

only problem occurs if a particle traverses the DSSD with an entrance angle close to 90°. In this special case mostly clusters with widths of two or one occur. The problem is that the charge cloud does not spread linearly to the readout strips. This leads to a non-uniform distribution. To solve this the η-correction is used[28]:

$$x_\eta = x_0 + pF(\eta) \ \ with \ F(\eta) = \int_0^\eta \eta' d\eta' \tag{1.16}$$
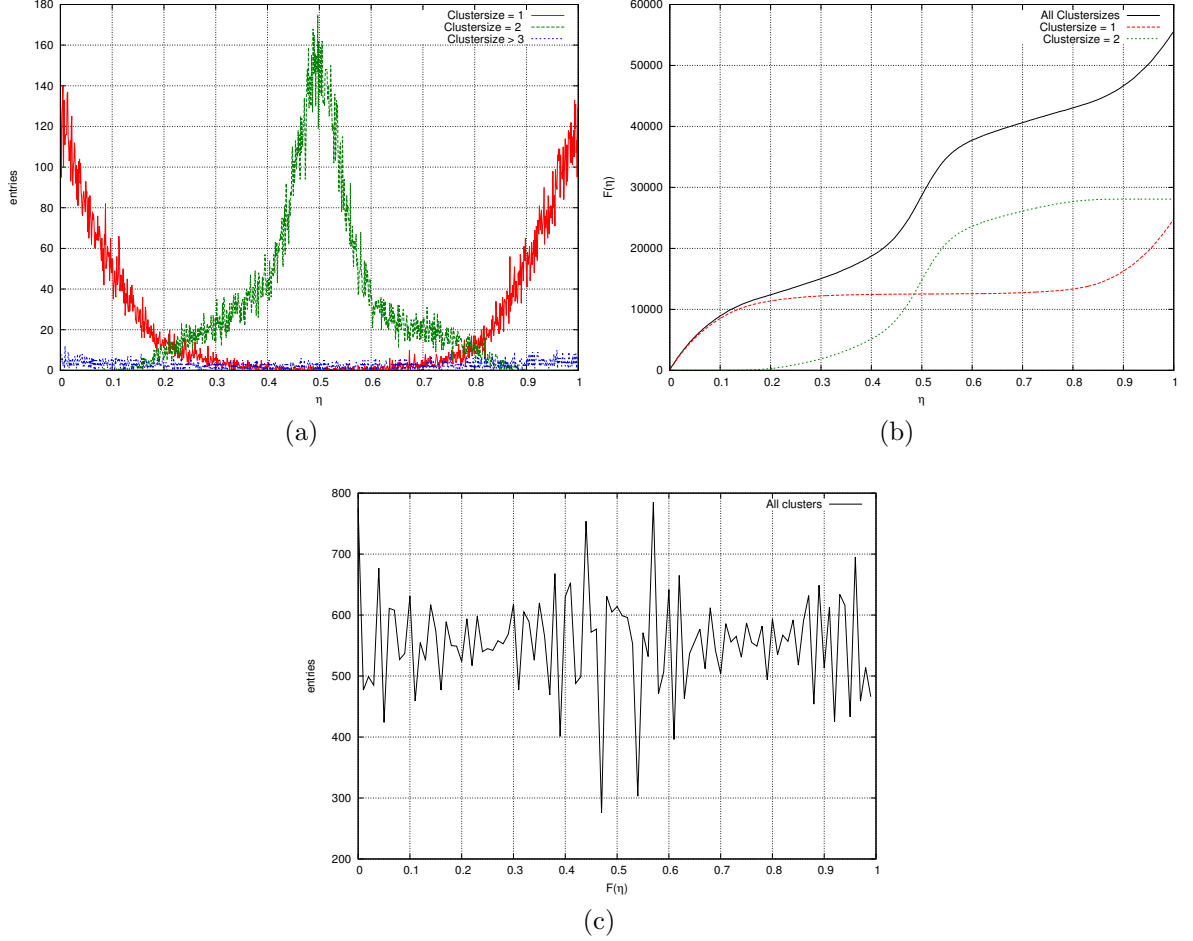
Figure 1.16: (a) Eta distributions of all cluster widths. The red peaks originate from the strips and do not contain additional information. The green peak originates from the intermediate strip and includes additional information throughout the slopes between the two peaks. Clusters > 3 are almost not taken into account, because COG already is the more significant method ; (b) shows $F(\eta)$ over all cluster widths; (c) shows the Eta corrected uniform distribution of all positions. The data was taken at Cern-test-beam by cooled BW module p-side

2 Construction and quality assurance

The Vienna institute of High Energy Physics (HEPHY) is commissioned to construct the ladder of layer 5. As the ladder 5 is a complex and a highly precise component of the SVD, it is necessary to improve and meet a level of quality assurance during the construction process. On the way to the final version of the ladder a lot of tests and adjustments were made. Hence it is also part of this thesis to contribute to this work.

2.1 Layer five ladder

Firstly, here we will highlight the Ladder and its components. The ladder consists of 4 sensor modules, three rectangular and one trapezoidal for the slanted part. Each module is labeled by its acceptance region with BW, CE, -Z and FW. BW and FW are read out through the PCB hybrids which have the APVs mounted. CE and -Z are connected via the origami flex boards. To have a thermal and electric insulation between the sensor module and the origami an Airex spacer is used. An APV has a power dissipation of 350 mW therefore a cooling has to be applied in the region of origami in order not to compromise full functionality and average lifespan of the sensors. To minimize the cooling effort all APVs are aligned in a row, thus a single cooling pipe satisfies the needs. The whole arrangement is placed on support ribs made of a radiation hard foam covered by a carbon fiber layer. With the advantage of less weight and stability the ribs are produced as a studwork structure.
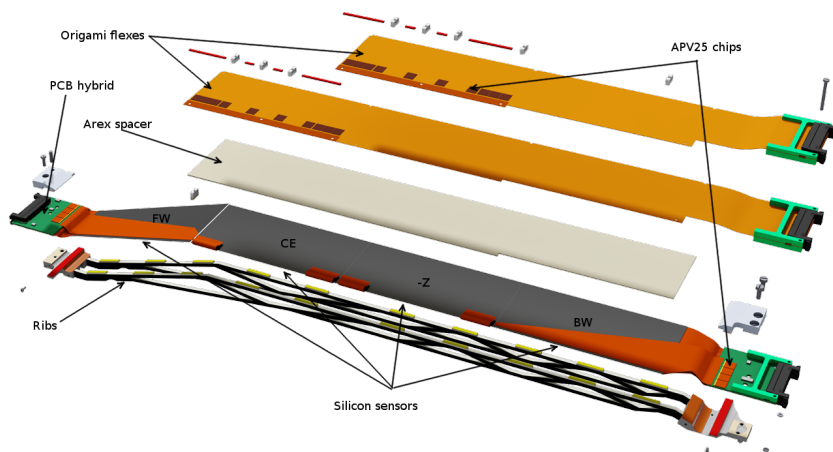

Figure 2.1: This figure shows a Layer 5 ladder explosion chart with all components

2.2 Thermal tests on the origami flex structure

The origami-flex-structure is a flexible printed circuit board especially developed for the SVD to connect to both sides of the sensor modules CE and -Z inside the acceptance region. All the electrical connections from the APV25 chips to the origami-flex-structure are ultrasonic-bonded with aluminum wires which are extremely sensitive to extraneous cause. In its working environment the origami-flex-structure has to endure different temperatures and also the occurrence of changing humidity. In order to guarantee the functionality of the origami-flex-structure itself and its bonded wires under these circumstances,a test over one week (fig. 2.2a)in a climate-chamber was carried out.

- Climate-chamber:
  - Producer : CTS Gmbh
  - Type: C-40/350-

- Supply Voltage : 1000V

- Thermal cycles: 14

- Temperature range: 15-60 °C

- Humidity range: 30%-95%

To test the electrical properties,a 1000V power supply was connected to the origami-flex-structure and the current dependencies were monitored. To verify the tensile strength of the wire-bonds before and after the thermal cycles Pull-tests were made and compared afterwards. Pull-tests are mechanical stress tests. The wire is pulled with a steady increasing force until it breaks.
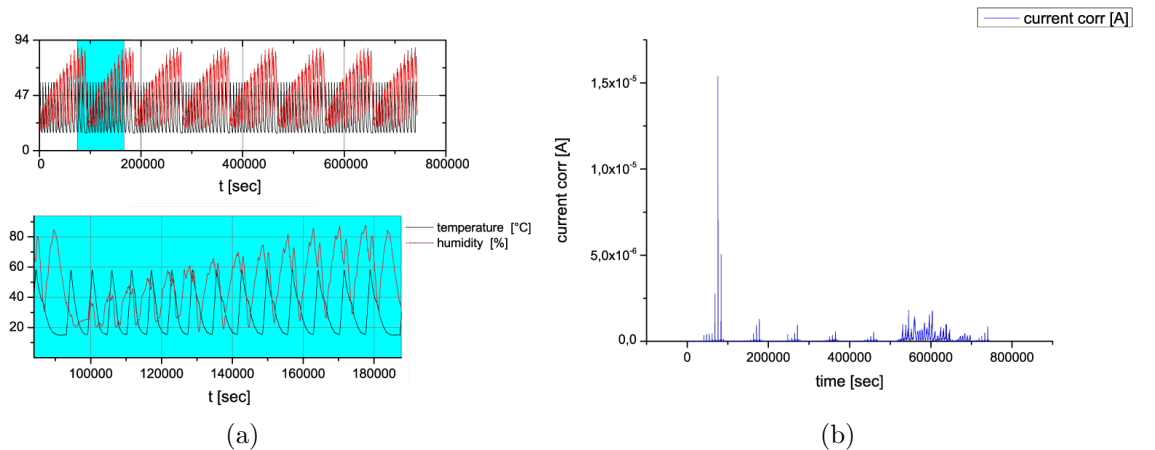

(a)   (b)

Figure 2.2: (a)humidity[%] and temperature [°C] over time, (b) I[A] over time; both diagrams ploted vs the whole test period of eight days

As shown in figure 2.2b throughout the whole measurement no relevant current appeared as expected. The current remained below 11 μA, these observed small currents are leakage currents.

2.3 Pull tests

As shown in table 2.1 there is a slight decrease of 6% in the tensile strength of the wire bonds from a mean value of 8.7g to 8.3g. These values are corrected by a factor which is calculated by equation 2.1. This equation returns the forces f_1 and f_2 2.3b which take effect on the bonds. The factor $a = 0.921$, with $\theta = 32.9°$, is close to one so there is no big deviation. This minor change in the tensile strength of the wire bonds should not affect the functionality of the origami-flex-structure. As shown in 2.2 the electrical functionality is still given.

$$f_1 = f_2 = \frac{F}{2} * \sqrt{1 + (\frac{d}{2h})^2} = \frac{F}{2sin(\theta)} = a * F \qquad (2.1)$$
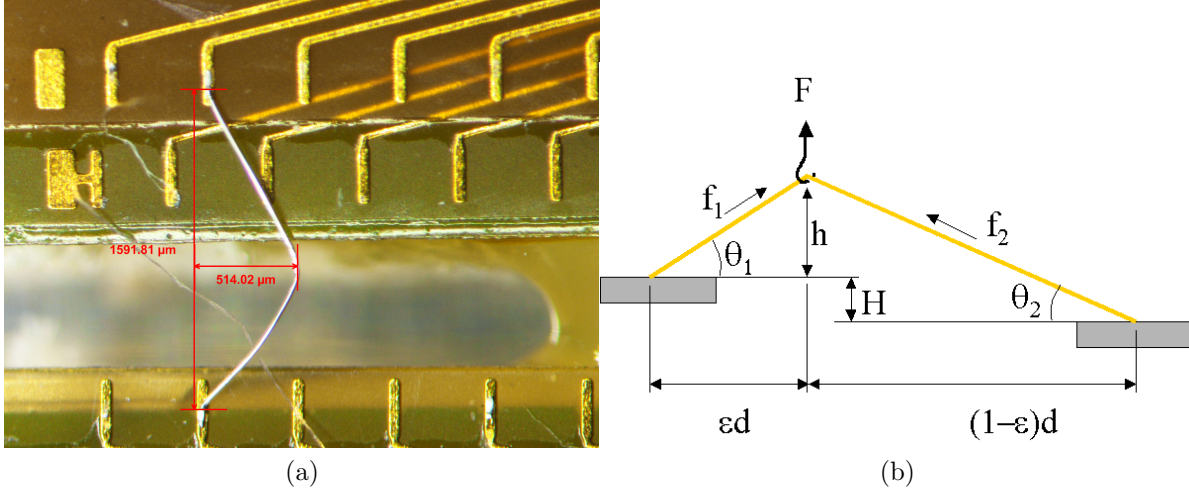
Figure 2.3: (a)dimensions of the aluminum-silicon wire bonds with a thickness of 25 μm (b) force f 1 and f 2

2.4 PCB-Hybrid tests

The PCB-hybrids are the link between the sensor modules FW and BW the cable connected to the ladder. Therefore APV25 chips are mounted on a PCB-hybrids. Each chip has 128 input channels which are connected to the silicon-detector strips via the pitch adapter. The APV chips need also connections for power, GND, I^{2}C Bus communication, I^{2}C address selection, differential analog output, clock, trigger and reset. Further hybrids contain the bias voltage lines for the high voltage, some resistors for line termination and capacitors for decoupling.

pull force [g]	entries		pull force [g]	entries
8	1		8	3
8,5	2		8,5	8
9	5		9	16
9,5	10		9,5	20
10	24		10	5
10,5	8		10,5	2
11	5		11	1
11,5	3		11,5	0
12	1		12	0
12,5	0		12,5	0
13	0		13	0
Total	59		Total	55
mean value	9,5		mean value	9,1
σ	1,5		σ	1,1

Table 2.1: Pullforce values before and after thermal cycles
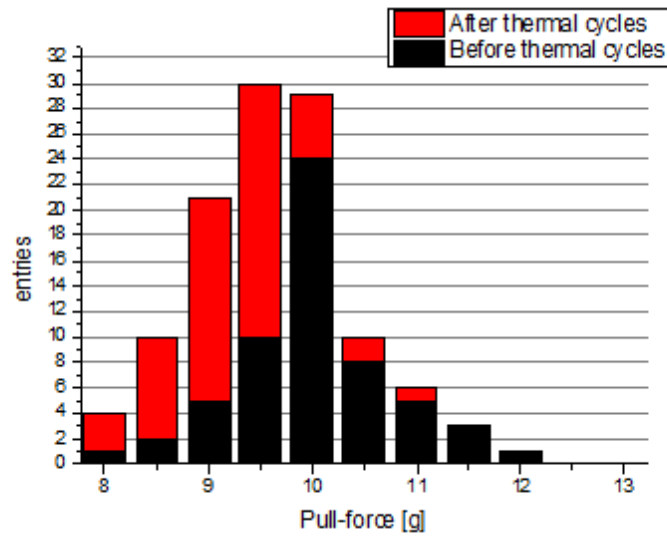
Figure 2.4: Pull-force ranges before and after thermal cycles

According to the side of the sensor module the PCB-hybrid has 4 or 6 APV´s mounted. However, the task was to test every channel of the mounted APV25 chips to check the complete functionality of the PCB-hybrids. To test APV25 chips, the PCB-hybrid is connected to a hardware setup which enables the use of APVDAQ. APVDAQ is a software developed by HEPHY for testing APV25 chips. APVDAQ is able to connect, with its hardware-test-setup, to the APV25 run some basic functionality tests, such as:

- ADC Delay Scan: Finds the optimal ADC (Analog-Digital-Converter) clock phase. The timing of the ADC sampling depends on clock frequency and cable length.

- FIR Calculation: Configures a FIR-Filter which suppresses the disturbances caused by reflections in data cables

- Software (Pedestal Run): Randomly acquires data from the APV25, by triggering its readout. This is used to determine the noise.

- Internal Calibration Scan: Is used to record the shape of the calibration pulse of each strip of the APV25 chip. Therefore the chip has an internal calibration functionality.

- IntCal vs. Vsep: for detecting Pinholes

As long as producing and evolving the PCB-hybrids are an ongoing process a consistent acquisition of data is necessary. Therefore the data acquired is extended and compared as shown in the following diagrams (2.5 - 2.8).

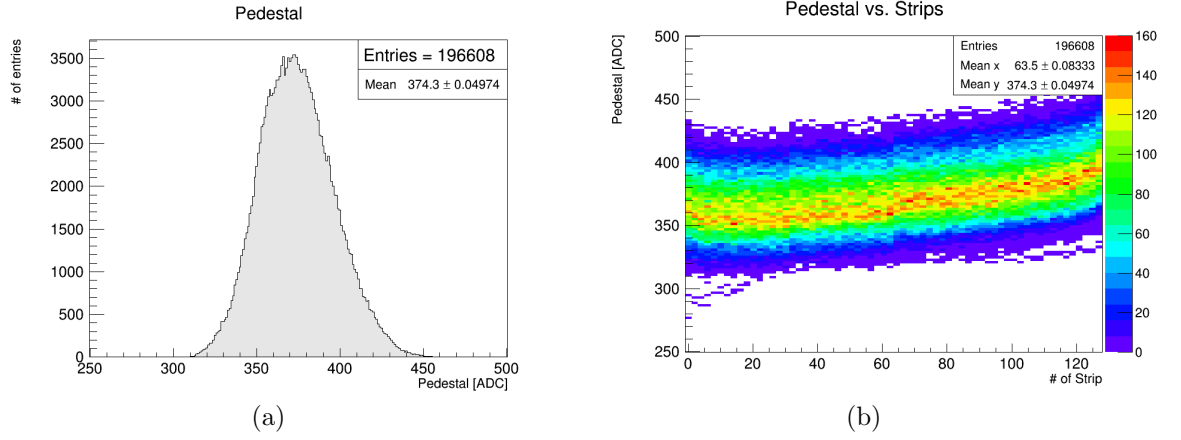Figure 2.5: The Pedestal Values shown in figure (a) are normally distributed.In (b) there is an increase at the higher number of strips which is due to the internal power distribution of the APV25 chips.
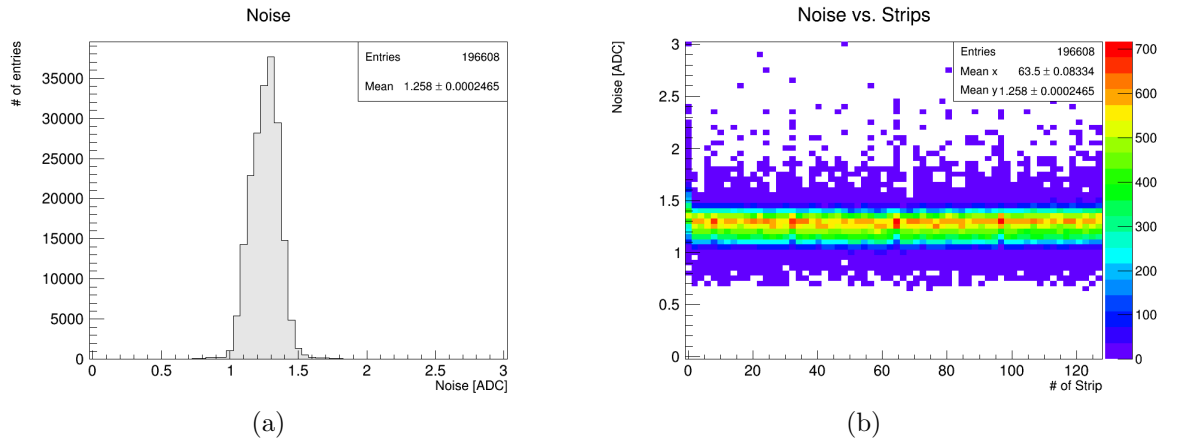

Figure 2.6: (a)The noise histogram shows an expected distribution. (b)The noise vs. strips histogram demonstrates that the mean values of noise are steady with some minor deviation at the strips (0,32,64,18) due to non ideal FIR filter configurations
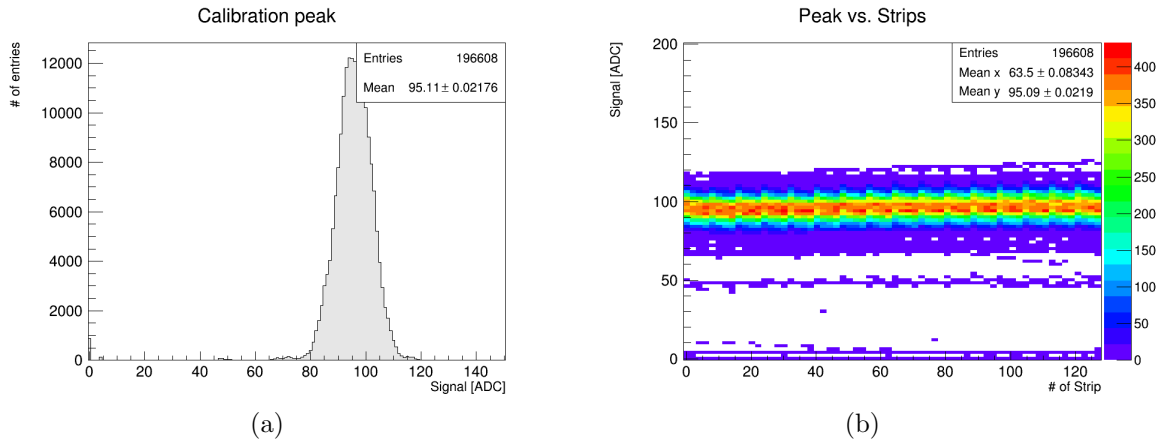
Figure 2.7: (a) Calibration pulse and (b) calibration pulse vs. strips histograms
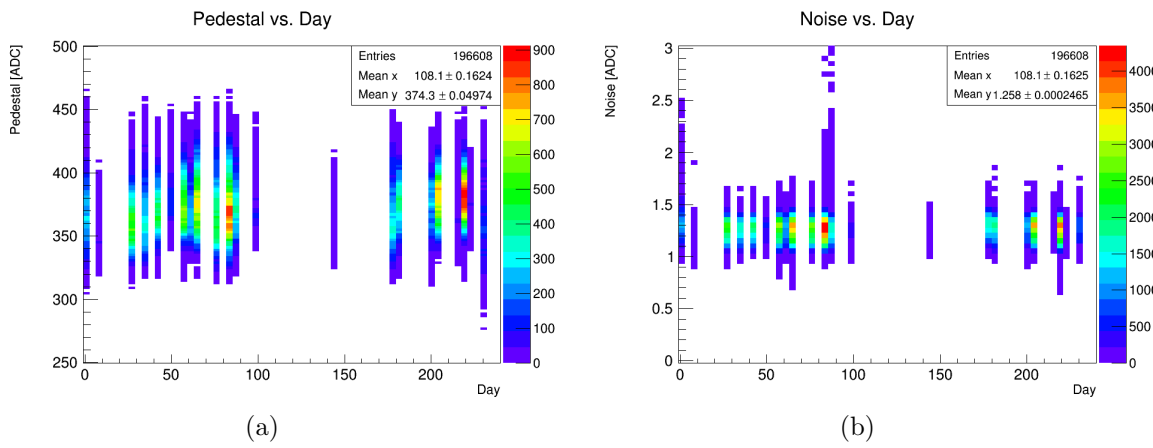
Figure 2.8: (a) Pedestal and (b) noise vs. date histograms, illustrating the performance of the tests throughout the whole construction time

2.5 Ladder test system

In order to fulfill the requirement of a ten year lifetime of the Belle II experiment each component of a ladder is tested carefully before being mounted to guarantee a high reliability. Nevertheless it is also necessary to test the ladder in its final state. Therefore a test setup, called ladder test system (LTS), for a fully assembled ladder has been developed. The requirement for the LTS is to test all strips of all sensor modules of a ladder for proper operation and displaying the measurement. Hence to the received data of the sensor going trough the whole readout chain, the testing of components such as APVs, hybrids, bonds and connectors is implied.

2.5.1 LTS working principle

The best way to test sensor modules is to have actual particle hits. This is why the LTS uses a ^{90}Sr Source which is a beta-emitter. The source is placed in front of the ladder emitting e^- towards the sensors. Behind the ladder a scintillator is attached for triggering the readout. The beam opening of the source has a diameter of 5 mm which is by approximation also the assumed beam diameter. In regard to dimensions of the ladder the beam is not able to cover the whole sensor area. Therefore, the ladder is attached to the movable XY-table using step-motors to aim the beam to any required position on the sensor. To shield the sensors from external influences and make measurements insensitive to particles such as photons, the setup is placed into a black box. The Box (DUT Box) dimensions have been chosen in such a manner to prevent the XY-table inside, including the attached ladder, from touching the surface of the box. That ensures the safety of the ladder while testing it. Moreover, the wire-bonds of the ladder are extremely sensitive to external forces, therefore the ladder is placed in a transport box. Additionally it is suggested to move the unwrapped ladder as little as possible to minimize the risk of any incident. For this reason it is possible to keep the ladder attached to mounting device on one side of the transport box and place it on the xy-table. Therefore the leftover side of the transport box has a diagonal opening to have plain sight of the beam. The attempt to place the whole transport box inside, which would be the safest way to carry out the measurement, failed because its the weight. The step-motors do not have enough power to lift the whole transport box.

For a test run it is important that the xy-table of the step motor moves along a path that covers all n-side and p-side strips. As shown in figure 2.9, the most convenient way is to scan each sensor module diagonally from one corner to the other. Nevertheless, a problem occurs on the edges which is noticeable as very low hit counts compared to positions located closer to the center. This can be explained with the beam profile of the ^{90}Sr source which can be assumed as a circle having an intensity gradient pointing at the origin. The strips on the edges will never fully cover the circle of the beam profile, and therefore the strips on the edges never attain the same intensity as strips closer to the center. The indication "strips on the edge" and "center" is with regard to the beam position. The workaround is to let source scan the path of 2 cm to the edges twice. The analyze tool is the TUXOA [34] which displays the hit-map, the signal to noise ratio
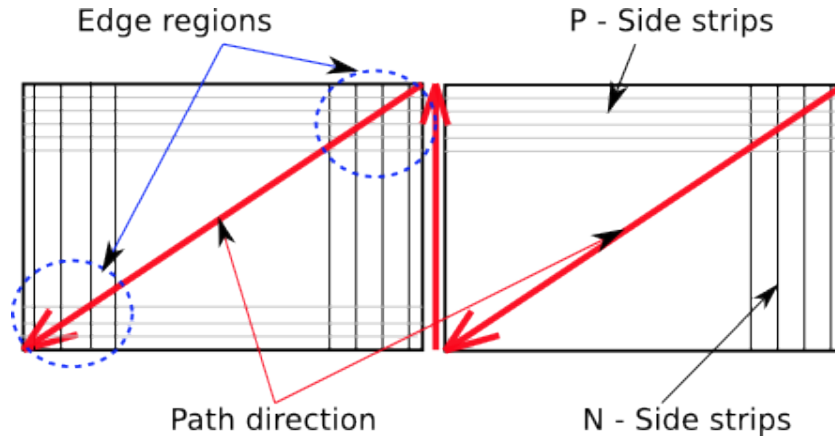
Figure 2.9: This figure illustrates that the beam (blue circle) never covers the same area at the edge then in the center while moving along the path (red arrows) and therefore the hit count is lower then in the center of the sensor

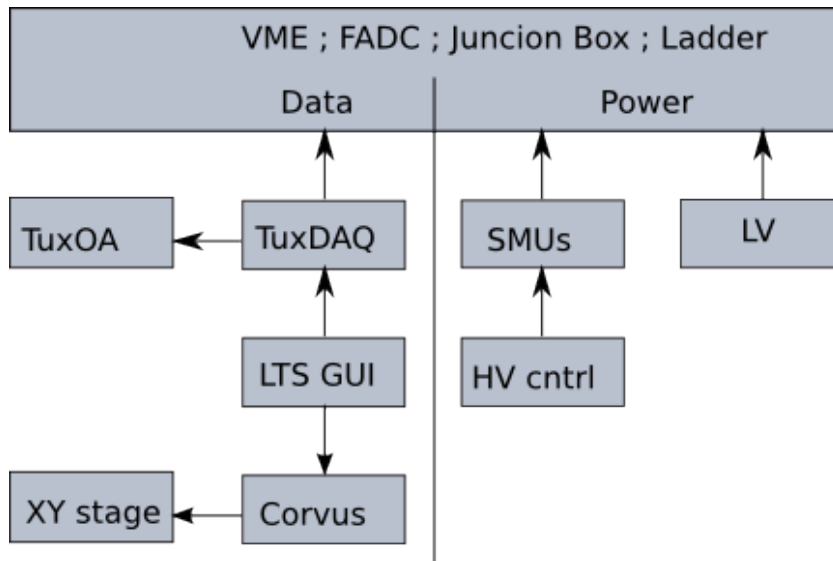(SNR) and the cluster width of each APV.

2.5.2 LTS setup

Figure 2.10: LTS modules; arrows show hierarchy

The Ladder-Test-System consists of multiple independently developed modules. Essentially there are two independent branches of modules which are necessary to run the LTS. The first one is the data taking branch which is responsible for data from the ladder and the readout chain. The readout chain for the LTS consists of a junction box of at least two junction boards for the n side and the p side strips. Furthermore a VME crate is needed which includes FADCs, an FADC-Controller and a buffer board and a

VME-PCI Optical Link Bridge to connect to the LTS PC. Beside the crate it is necessary to have an external trigger because in this test setup we do not have access to the Belle II trigger. In case of the LTS the trigger is given by a scintillator attached in the LTS Box. The trigger defines the data taking rate, but is limited by the data processing time of the TuxDAQ. The typical a trigger rate is about 30 Hz. The 30 Hz mean that 30 events per second are taken. This sounds very low compared to data taking in Belle II, but it is more than satisfying for the purposes of the LTS. Here we use the VME bus instead of COPPER for data acquisition whose transfer rate is limited to a few Mbyte per second. On the LTS PC three autonomous running programs are installed :

1. **TuxDAQ**[34] is data acquisition unit which communicates with the FADC via VME and saves the data into a ".dat" file. The TuxDAQ is capable of several operation modes. Before data taking 3 configuration runs have to be taken. The ADC delay scan determines the optimal phase for each ADC sample clock which corrects the time difference of the APV signals by different cable lengths. Due to dispersions and reflections in long cables error bit signals overlap partly, therefore a FIR filter is used whose coefficients have to determined in the FIR-filter run. The last configurations are determined by the calibration run which is used to find defect strips and to estimate the gain of each strip. All the configuration parameters are written into a configuration file.

2. **TuxOA**[34] is the analyzing and monitoring program. It streams the data from the TuxDAQ and displays the signal from all APVs. Then writes it for further evaluation into a root [7] file.

3. **LTS GUI** coordinates the measurement. That means it calculates the scanning path and sends it to the step motor (Corvus). Additionally it handles the data taking by controlling the TuxDAQ.

All three programs have been developed for Linux and are presently running on Xubuntu. The second branch is responsible for the power supply. The two voltages, needed for running the LTS, are LV (low voltage) and HV(high voltage). While the LV is supplying the APV's 10 V with two linear lab power supplies, the HV is the reverse bias voltage need to power increase the depleting one inside the sensors. To safely apply the HV of -100V/+100V the voltage is slowly ramped. This is accomplished by the program KeithleyRC that controls two source measurement units (SMU) via GPIB (IEEE 488.2). KeithleyRC also monitors the voltage and has the option to record the I-V-curve. The program is developed with CVI which is an ANSI C integrated development environment and engineering toolbox from National Instruments. Nevertheless, the s Linux support from National Instruments is limited and not free, therefore the power supply PC runs with Windows. All power cables are connected to the junction board. The LV power cables are very susceptible to induce noise, thus the pairs of cables are twisted which has proven to be a workaround. The HV uses coax cables with a built-in $1k\Omega$ which raises the input impedance of the junction box side and makes the SMU measurement more reliable.
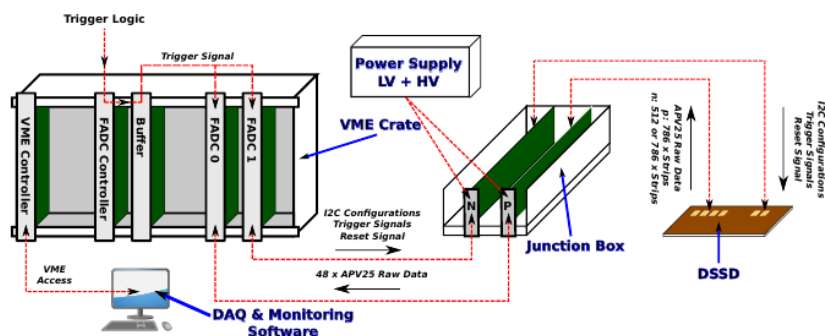
Figure 2.11: LTS readout chain

2.5.3 LTS GUI software

LTS GUI is written in C++ and developed with Qt 5, which is a cross-platform application framework. Nevertheless it is compiled to run on Linux.
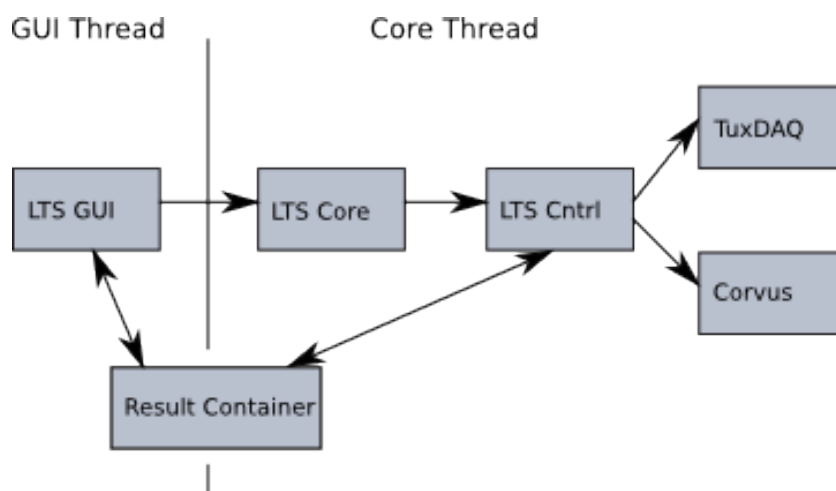

Figure 2.12: Basic objects of the LTS GUI program. The arrows signaling the data flow. The two threads are needed to keep the program operational while waiting for data. The result container is thread safe, so the GUI and the core can exchange data.

The LTS GUI software handles the measurement runs. Therefore, it is the link between TuxDAQ and the Corvus step motor. It communicates with both via TCP/IP in server and client mode. This is necessary because the Corvus always operates in a server mode and it is more reasonable to use the TuxDAQ as client.To create the connections the config file has to be read. It is an XML file 6.1.1 and contains all the crucial data for establishing the TCP connection. Additionally it holds the scanning path information. Under the tag " $< POSITIONS >$ " all vertices of the path are listed with the tag " $< MEASURE >$ ". A corner point consists of three data values x, y and the number of steps. Obviously the first two values are the coordinates of the corner point, the

third value is the number of steps from the actual position to the corner point. That means the program calculates a line from one corner point to the other corner point with "#of steps" positions, for measurements, in between. In consideration of the minimum step-width of the step motor which is $1\mu m$ the ratio, path length to steps should not be smaller. Another parameter of the configuration file is the " $< NrUpdate >$ " which tells the Tuxdaq how many events should be taken for each step of the path. Another important part of the configuration process is the calibration off the xy-table. Therefore, the yx-table moves to the most upper left position until the end switch is are touched. That is the origin for every run. After starting a run the program holds a vector with all measure point coordinates and deletes them after passing one. If an error occurs it writes the vector into a file which can be read after configuring by using the continue option instead of the start one. Thus it is possible to continue a run after a crash. This is advantageous, because of the long run durations which can take up to 4 hours depending on how many steps and events for a measurement run are configured. The programs runs with two threads, which is necessary to keep the graphic user interface (GUI) operational, while the core handles the communication. Therefore, the core is a state-machine, whose states can be changed by switching its transition states. This happens by pressing buttons on the GUI.
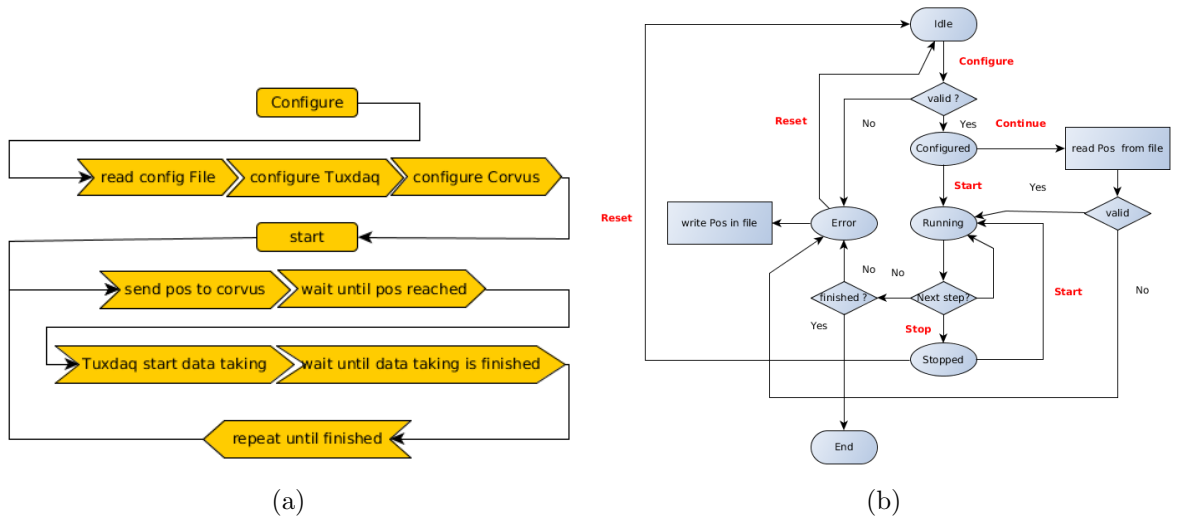

(a)   (b)

Figure 2.13: (a)Program flow of a measurement run without exceptions.(b)Flow chart of the state-machine which runs in the core thread of the LTS GUI. The red labels illustrate buttons.

2.6 Alix Cooling Box Control

In the Belle II experiment the SVD together with the PXD will be cooled by a dual phase CO_2 system. The principle of the CO_2 is used for many particle physics experiments. Nevertheless the idea is using the latent heat of the phase transition from liquid to vapor of first order. Therefore, the CO_2 needs to be in its his liquid phase at the beginning of the cooling process(figure 6.6). The CO_2 needs to be close to the vapor-liquid equilibrium (saturated fluid),in this state where the rate of evaporation equals the rate of condensation. In this condition the liquid vaporizes immediately and is therefore ideal for cooling. Nevertheless, the system is liquid driven [30], that means it is not wanted to vaporize all the liquid, but partly. The vapor quality χ expressed in 2.2 describes the amount of vaporized CO_2.

$$\chi = \frac{m_{vapor}}{m_{total}} \tag{2.2}$$

In the initial state of the cooling $\chi = 0$, which means no vaporization has taken place and the CO_2 is in liquid state. If the $\chi = 1$ the vaporization limit is reached and no CO_2 is in liquid state anymore. At this point the cooling is failing. This could happen, if the mass flow is too low or the heat load too big. The amount of latent heat is defined through the enthalpy of vaporization (figure 6.7). Hence the formula 2.3, where ϕ is the mass flow, H is the enthalpy of vaporization and P the cooling power.

$$P = \phi H \tag{2.3}$$

If we use the CO_2 cooling system in the mixed state, which means $0 < \chi < 1$, H becomes ΔH and consequential the equation 2.3 becomes:

$$\begin{aligned} P &= \phi \Delta H \\ &= \chi \phi H \end{aligned} \tag{2.4}$$

CO_2 is also ideal for cooling detectors, because of its relatively high evaporation pressure in which the cooling can be performed. The pressure keeps the vapor volume small and cares for a very good cooling performance in thin pipes. Additionally it has a large latent heat, which allows a reduced fluid flow. In the Belle II experiment the VXD uses IBBelle, which is a closed CO_2 system with 3 kW cooling power. It was necessary to develop a smaller version to test the cooling pipes during the mounting procedure and to perform tests to determine the signal to noise ratio. The Alix-Cooling-Box-Control (ACBC) is an open CO_2 system. The main reason to develop the ACBC was to test the cooling during the mounting procedure in the final setup.

2.6.1 ACBC setup

The ACBC is designed to be part of test beams, mockup tests and the SVD assembly. The requirements are to cool down to a temperature of to -20 °C, to run stable, to have cooling power at least 100 W, to be as independent from external inputs as possible
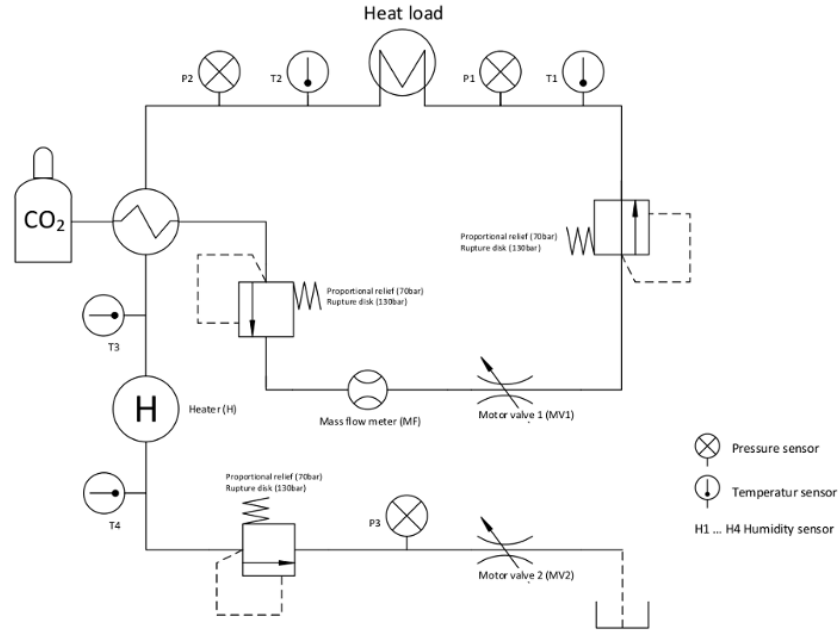
Figure 2.14: Schematic of the ACBC

and to have a good mobility. The whole system is inside a movable aluminum box with connectors for power, compressed air and CO_2. For this reason the ACBC is supplied by CO_2 gas bottles with pressure up to 70 bar. As shown in figure 2.14 the liquid CO_2 streams into a heat exchanger and gets cooled down close to a saturated fluid by exchanging heat with the exhausting CO_2. Further the saturated fluid moves to the first motor valve which in cooperation with the second motor valve regulates the pressure and mass flow for the following device under test (DUT). When it gets to the DUT, the inner diameter of the ACBC pipes of 4 mm is reduced to 1.4 mm of the SVD cooling pipes. At the DUT the saturated fluid gets the heat load. After passing the heat exchanger, the heater is reached which brings the CO_2 with 1200 W back into the vaporized state and,therefore, prevents the exhaust from being iced. The transfer lines to the DUT are 20 m long and isolated to have enough free moving space. In regard of the low temperatures it is reasonable to flood the inside volume of the box with dry air to prevent condensation. Therefore, an air filter membrane is integrated which only requires compressed air. Because of the pressure levels up to 70 bar, the system has safety precautions in terms of pressure reliefs (70 bar) and as backup burst disks (130 bar). The monitoring sensors and the motor valves are controlled by Alix a PC Engine with System-board that can be addressed via TCP/IP. Therefore, a router is installed that can connect to WAN and also handle internal Ethernet, which makes it possible to remote or locally access the ACBC.

2.6.2 ACBC software

The ACBC GUI was developed to control and monitor the cooling process by reading sensors and operate the motor valves (see figure 2.14). It is written in C++ and developed with the same tools as in the LTS software (see 2.5.3). Its concept is to run with two threads to keep the GUI operational while the core is processing data. The class Alix-Com holds the routines to communicate with the Alix which is done by strings. All the sensor and motor valves are addressed and read out by this class. The collected data is written in a result-container. The Alix-Com object is owned by the ACBC-core class which internally runs a state machine. This state machine instructs the Alix-Com class to read or write data to the Alix. Additionally the ACBC core swaps the result containers, once the read/write cycle is over. So it never occurs that the GUI and Alix-com read or writes at the same time. This is crucial for thread safety. The GUI reads the data, provided by the core via the result container and displays it. The GUI owns the ACBC core object and, therefore, is also able to control the state machine by requesting a state transition (e.g. running → stop → stopped). Additionally the GUI has the task to monitor critical values such as pressure, dew point, mass flow and the connection to the Alix. To have a visual signal the LEDs flash red in case a value is outside its boundaries. Additionally an alarm tone appears which has to be turned down manually.

Senor	safe range (green)
T4	>10 °C
Heater	40...140 °C
H1...H4	$< \min(T1...T4)\text{-}5$ °C
Dry air	50...150 l/min
P1...P3	0...50 bar
MV1..MV2	$\|actualvalue - setvalue\| < 1$ V
Box Temp	< 40 °C

Table 2.2: safe ranges for the monitored sensors ; outside the ranges the LEDs switch red and an alarm sounds

As shown in table 2.2 some safety boundaries are necessary to operate the ACBC. T4 > 10 °C is required because of the possibility of an iced exhaust. In this case pressure raises and the cooling fails. Closely tied to this topic is the heater temperature range. The heater is controlled by relay, if switching hysteresis is too big it is possible that T4 drops. That leads to the same issue than before. As we have temperatures below room temperature, care must be taken care of the condensation issue. The pipes inside the box have temperatures of -20 C°. The ice which would appear from the condensate would destroy the sensors and block the motor valves. Therefore, it is important to have the box volume flushed with dry air. On the one hand this is guaranteed, if the volume flow is inside defined ranges (table 2.2), on the other hand it is safer to monitor the dew point as well which has to be below the temperatures T1 to T4. Due to high costs the ACBC does not have real dew point sensors, but it has temperature and humidity

sensors. Hence the GUI calculates the dew point with the two values and the equation 2.5 [27]:

$$Dp(T, H) = \frac{\lambda(ln(\frac{H}{100}) + \frac{\beta T}{\lambda + T})}{\beta - (ln(\frac{H}{100}) + \frac{\beta T}{\lambda + T})} \tag{2.5}$$

with the temperature T,the relative humidity H and the magnus parameter β, λ. Even though this the dew point value is not very precise, it is good enough for this implementation. Pressure is an important value as it is an indicator for the state of the CO_2. The motor valves are the only instruments to control the ACBC. The ACBC GUI can set the motor valves by sending a value. It also can check for the actual value of the valves. So, if the valves are blocked, the difference of the set and actual value appears for a long period of time which also triggers the alarm.

(a)   (b)
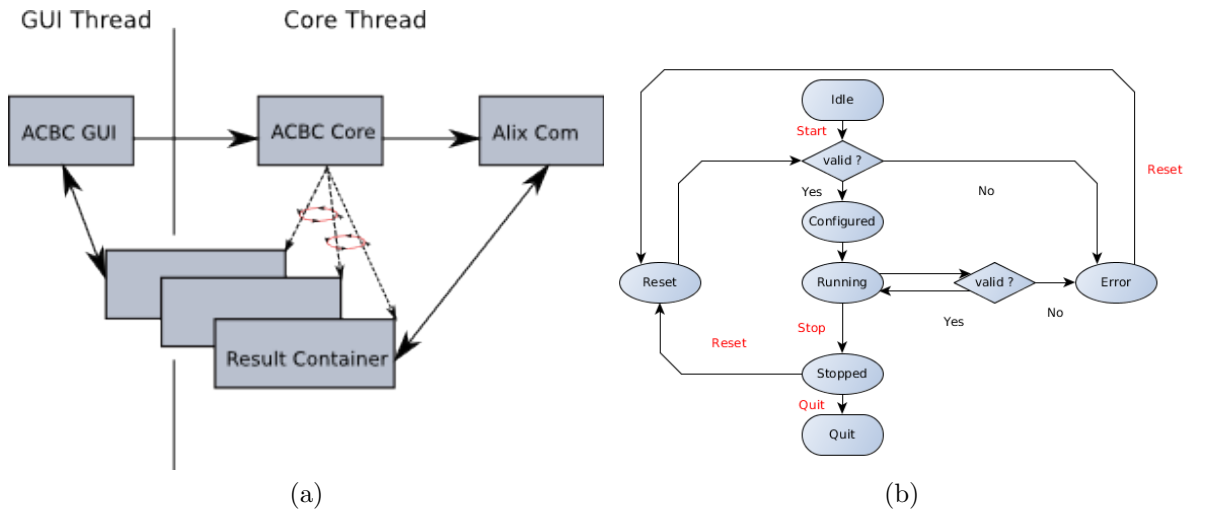
Figure 2.15: (a)shows the classes of ACBC GUI ; The arrows illustrate the information flow, where ACBC core swaps the result containers after a read/write cycle.(b) Chart flow of the ACBC GUI, where the red labels illustrate buttons.

To control the cooling process the mass flow is an important parameter, as equation 2.3 shows. Therefore, to simplify the management of the ACBC, a PID-controller controlling the mass flow is implemented. A PID-controller is realized by equation2.6:

$$y = \underbrace{K * [e}_{Propotional\ term} + \underbrace{\frac{1}{T_n} \int_{-\infty}^{t} e(\tau)d\tau}_{Integral\ term} + \underbrace{T_v \frac{de}{dt}}_{Derivative\ term}]$$

$$e = set\ value - actual\ value...control\ difference$$

$$T_n...reset\ time$$

$$T_v...derivative\ time$$

(2.6)

where T_n and T_v are factors of how fast the impact of the different terms are. Because, it is implemented into a C++ program, the equation has to be discretely approximated. This leads to equation 2.7:

$$
\begin{aligned}
y_i &= K_P e_i + K_I \sum_{m=0}^{m=i} e_m + K_D(e_i - e_{i-1}) \\
K_I &= \frac{T_s}{T_n} \\
K_D &= \frac{T_v}{T_s} \\
&T_s \dots sampling\ rate
\end{aligned}
\tag{2.7}
$$

These equations are easy to realize digitally, therefore implemented in the ACBC GUI. In addition one last modification, due to output range of 0 to 10 V, has to be exercised. As the single terms contribute to the output, depending on the control difference, e_i, y_i would be 0 if the adjusted value were reached. Thus $y = \sum_{i=0}^{m} y_i$ brings the offset of the adjusted value. Besides, the system is quite slow, so we can set the D term to null. Moreover, boundaries for the y and I term of the PID have to be set, otherwise those values might sum up outside the output range.

Parameter	Value
K_P	0.1
K_I	0.01
K_D	0
Output	$0 \leq y \leq 10$ V
I-term	$-1 \leq I \leq 1$ V

Table 2.3: Parameter ranges and values for the PID;

2.6.3 ACBC tests and performance

The test run with the final version of the ACBC was performed at HEPHY. The DUT was a 50 cm long stainless steel cooling pipe with an inner diameter of 1.4 mm. On the DUT a heating wire and a thermocouple were attached. The thermocouple was used to get the actual temperature of the DUT. To prevent losing heat to convection and to obtain realistic data of the heat load, the DUT was covered in Armaflex insulation. For connecting to the DUT the standard 20 m transfer lines with an inner diameter of 4 mm were used. The measurement started after the CO_2 gas bottle had been opened. The mass flow was adjusted to 2 g/s and kept stable during the whole measurement. Once the -20 °C were reached, the heating wire was set to 50W dissipation. The total measurement period took 1h.

In order to estimate the mass flow adjustments for the operators, the following measurements were made: The mass flow was set to 6 g/s with a 50 W heat load. After a
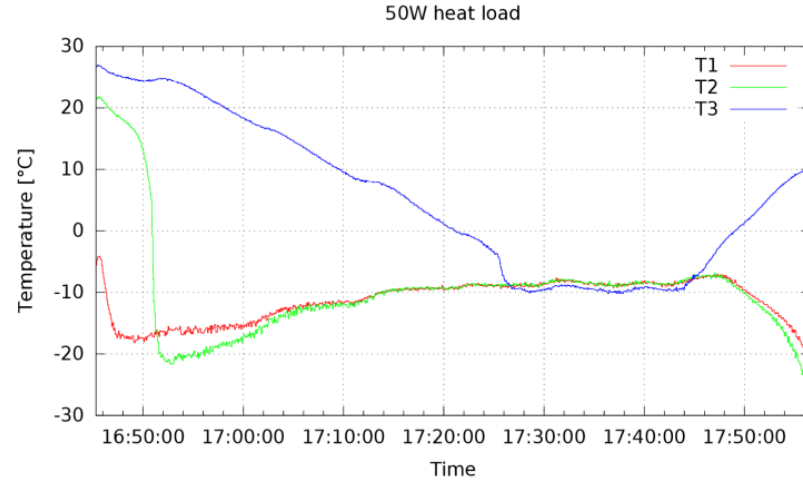
Figure 2.16: as expected the temperature dropped to -20 °C; The delay between T1 and T2 is because of the length of the transfer lines; T3 is delayed heavily due to the heat capacity hot the heat exchanger ; After switching on the heating wire (50W) the DUT temperature stabilized at -10 °C
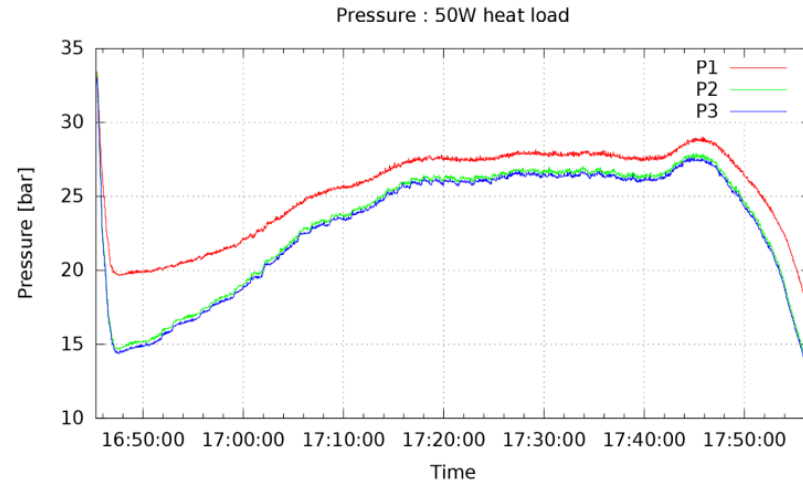

Figure 2.17: When the temperature reaches -20°C, the pressure equals 20 bar which is consistent with the enthalpy diagram 6.6; After turning on the heating wire the vapor quality χ raises what leads to reduced mass flow and a pressure raise; As the mass flow kept stable the pressure stabilized at 27 bar and a DUT temperature of -10 °C which is also consistent with the enthalpy diagram
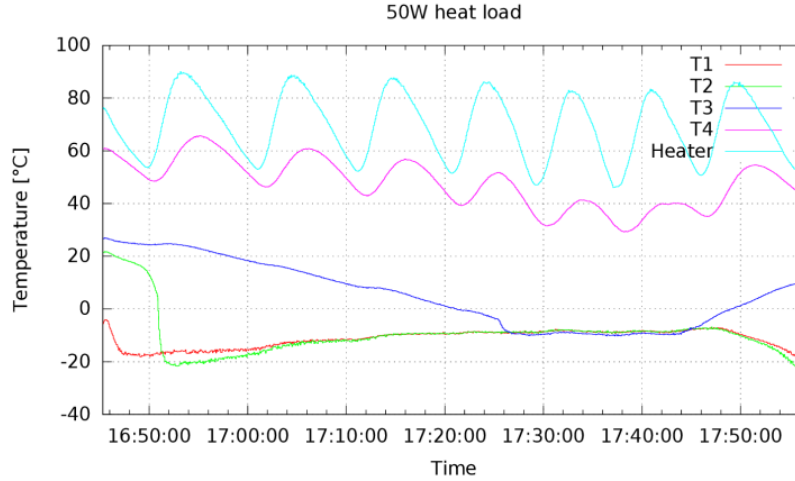
Figure 2.18: In this figure it is shown that the switching-hysteresis of the heater does not correlate with T1 and T2 ; Also T4 does not drop in regions where the exhaust could get iced

stable cooling temperature had been reached ($\sim$ -20 °C) the mass flow was reduced step by step until the temperature had rosen exponentially to approximately 60 C°. This was repeated twice with 100 W and 140 W. The curves were fitted and the intersections at -10 C° determined. The diagram presenting the values and fitted with a straight line serves as good guidance for adjusting the mass flow of a certain heat load.

(a) (b)
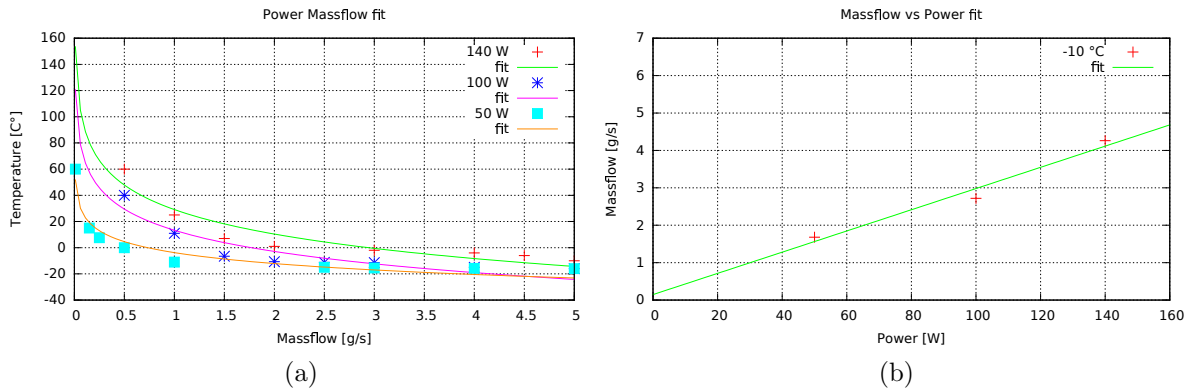
Figure 2.19: (a) shows the three temperature curves by reducing the mass flow step by step; (b) shows the mass flow for T = -10 C° at different powers ; The line does not intersect with the origin, because there is always some heat supply even without external heating

41

3 CERN-Test-Beam

While the construction of the layer five ladder (L5) is ongoing, it is essential to undergo tests in an environment of particle exposure similar to the native one in the Belle II experiment. These tests where held at CERN Super-Proton-Synchrotron (SPS). The SPS is a particle accelerator which reaches energies up to 400 GeV and nowadays also serves as injector for the Large-Hadron-Collider (LHC). This mode of operation allows the SPS to be used as beam provider for fixed target research. The initial SPS beam consists mainly of protons and provided in bunches. At the test site (H6) it is a secondary beam consisting of $\pi^\pm, K^\pm$ and p and it was operated at 120 GeV/c. The test area is separated in two zones: H6A downstream and H6B upstream. In H6B a EU-telescope [11] was used to carry out resolution measurements on the BW rectangular and FW trapezoidal DSSD sensors using the old SVD3 [13] setup. While H6A was hosting the test setup for the fully assembled L5.903. This thesis will focus on the results of latter one.
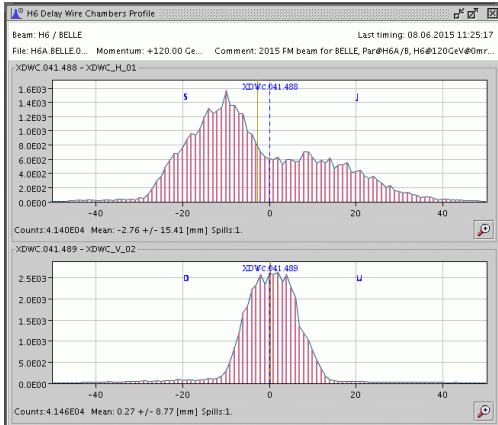
Figure 3.1: Beam profile horizontal and vertical

Parameter	Value
P_{max}	120 GeV/c
Acc	Some $2\mu Sr$
$\Delta p/p_{max}$	$\pm 1.5\%$

Table 3.1: Beam parameter [9]

3.1 Test setup

The H6A test setup was conceived to carry out two measurements at once. The first one was to obtain the readout data from the L5.903 ladder (L5) with high occupancy while the cooling is turned on and off. For the sake of completeness it must be mentioned that L5.903 is a class B- ladder, which differs in the length of the Origami modules, but works electronically perfectly fine. The readout chain applied was the same as in section 2.5.2 (figure 2.11). For receiving data from all sensor modules the L5 was mounted on a XY-table which could be controlled remotely. Additionally the L5 setup was placed inside the DUT-Box. The cooling system attached to the L5 was the ALIX, an old

version of the ACBC (section 2.6). The second measuring was to gain some resolution information on the L5 ladder and necessarily including tracking of particles. That was done by attaching single sensor modules outside the DUT box according to the telescope layout. In order to simulate the SVD, modules of all layers are used. Layer 4- and layer 3-sensors were attached at the front (facing the beam), layer 5 and layer 6-sensors at the back. layer 3 and layer 4 have been swapped in comparison to the original order of the SVD setup. The aim was to have the detector plane with the smallest pitch as close as possible to the DUT in order to get a better spacial resolution for the telescope. To trigger the readout a scintillator was placed inside the DUT box, between L5 and layer 5. To handle the input, 16 hybrid cables to the junction board, 8 flat-band cables from the junction board and two FADC-boards were used. Since the supply voltages must be very stable and riffle free, a dedicated power supply Kenwood N-5097A/B was used which is able to provide high voltage (HV) and low voltage (LV). This power supply was already used in the Belle experiment. It has a GPIB connection and is controllable via EPICS (Experimental Physics and Industrial Control System) based program.
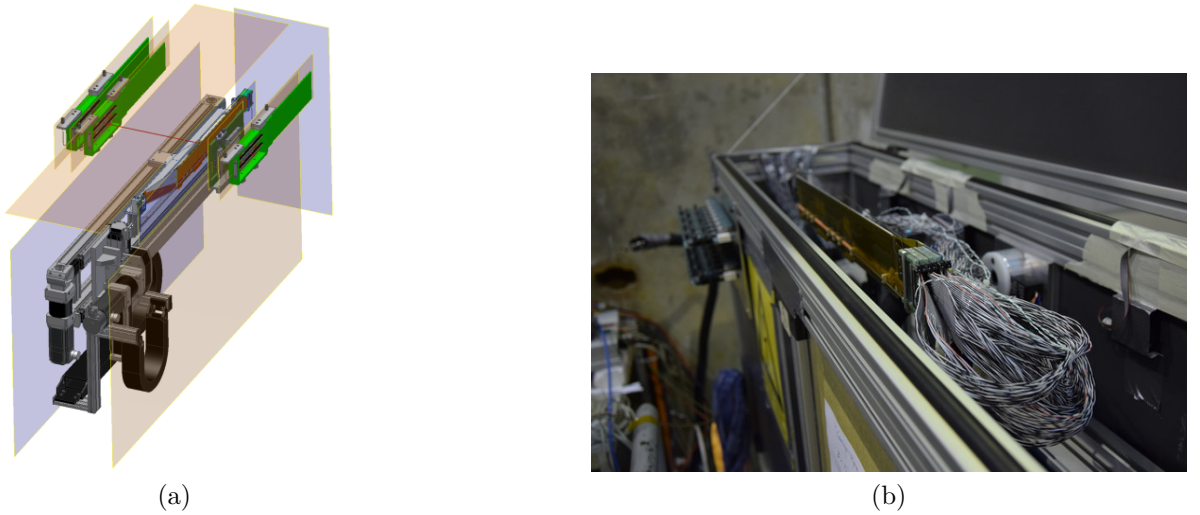

Figure 3.2: (a)"Pseudo-telescope" with single modules in front/back and the L5 ladder.(b) Fully assembled L5 ladder mounted on the XY-table.

The DUT box was placed on a height-adjustable stage and was oriented with a laser towards the beam center. As turned out later, the alignment had not been ideal due to rotations in the XZ-plane. The whole setup was covered by a lightproof sheet to avoid compromising the measurement by photons.

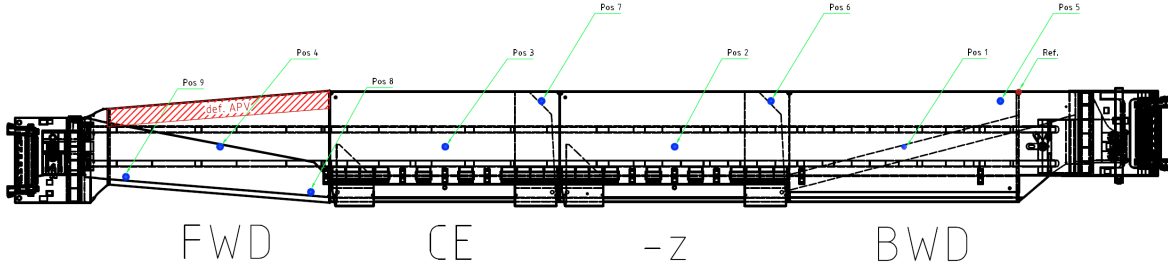## 3.2 Signal and noise measurements

Figure 3.3: This figure shows all measured positions on the L5.903 during CERN SPS test beam 2015. It is used as reference in the following analysis

The aim of this measurement was to to get information about the signal, noise and signal to noise ratio(SNR) provided by the fully assembled ladder (L5.903) with high occupancy from the particle beam. Additionally data was taken, while the ladder was cooled with CO_2 to a temperature of -20C°. As a matter of fact it was the first beam test with the cooling pipes attached to the ladder. Several positions were scanned for the analysis as shown in figure 3.3. The figures below show the data taken from the sensors of the L5.903 without cooling. The data implies that all senors and the readout chain were working properly. The hit maps match the the beam profile (figure 3)which is not obvious in the first place as the hit maps only show a section of the beam profile. The reason for this is the scintillator which triggers the events if a particle passes it. Therefore, the hit maps display the beam profile only in sections of the scintillator's size. The slope of the noise plot (figure 3.7c) is due to the trapezoidal geometry of the FW sensor and the n-side strips getting shorter. The red marked strips at the following figures are bad strips. They are excluded from the measurement once they are above a certain threshold.
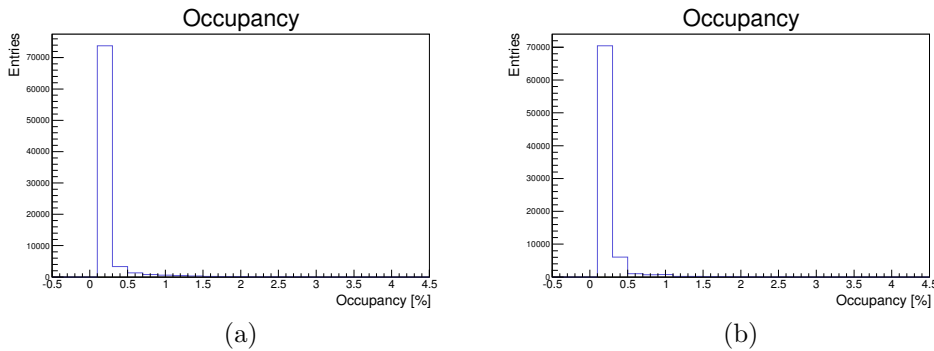

Figure 3.4: Pos 4 ; FW sensor ; (a) n-side and (b) p-side the occupancy is representative for all sensors
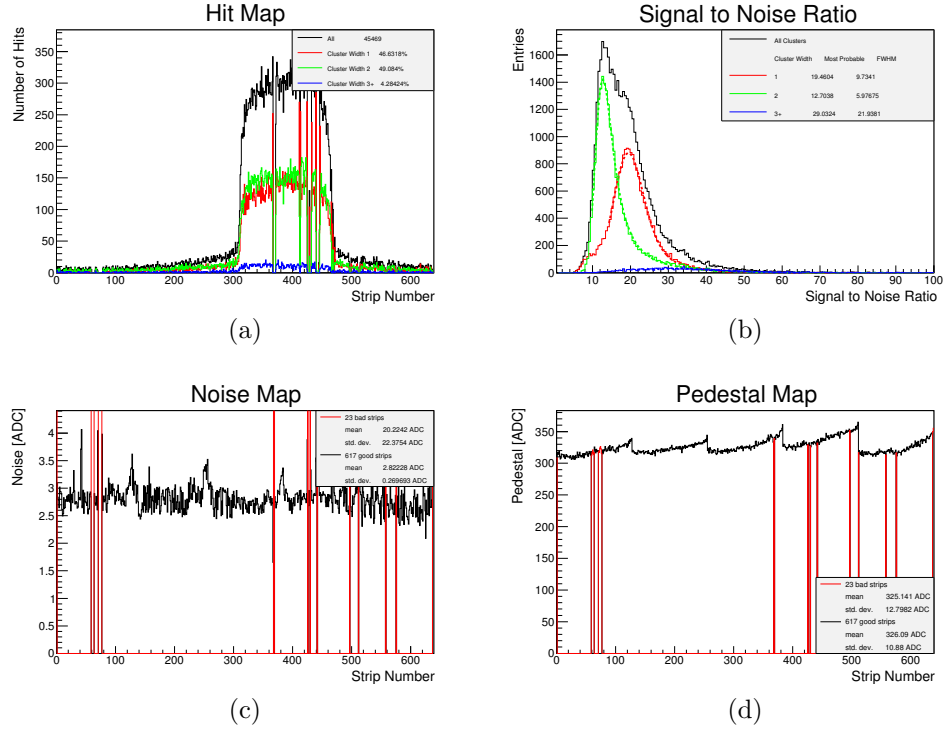
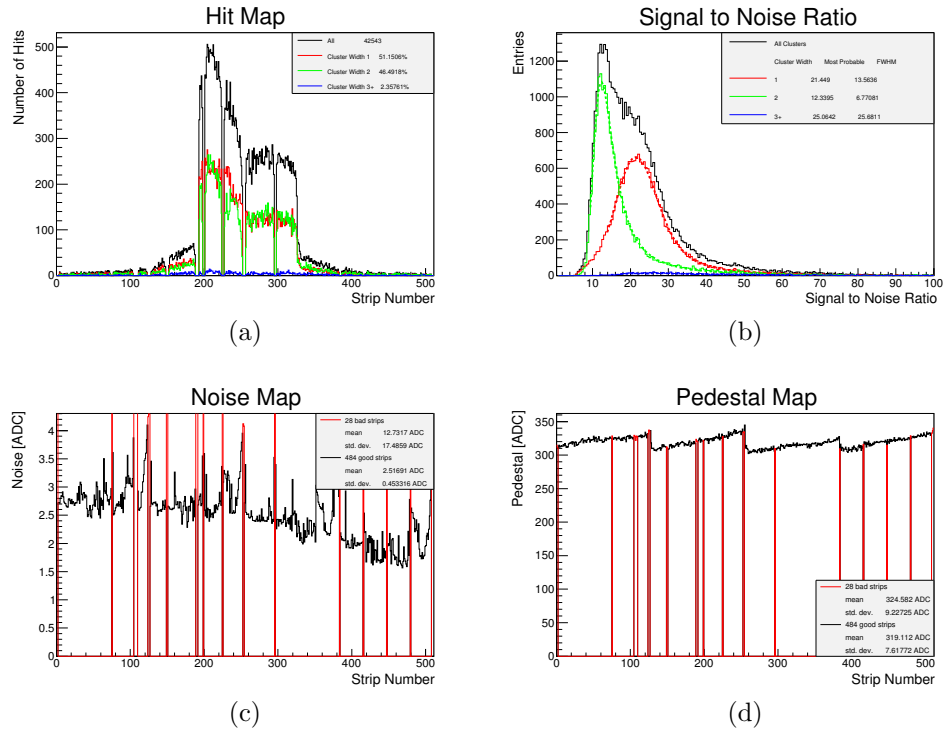Figure 3.5: Pos 4 ; FWD sensor ; p-side ; without cooling

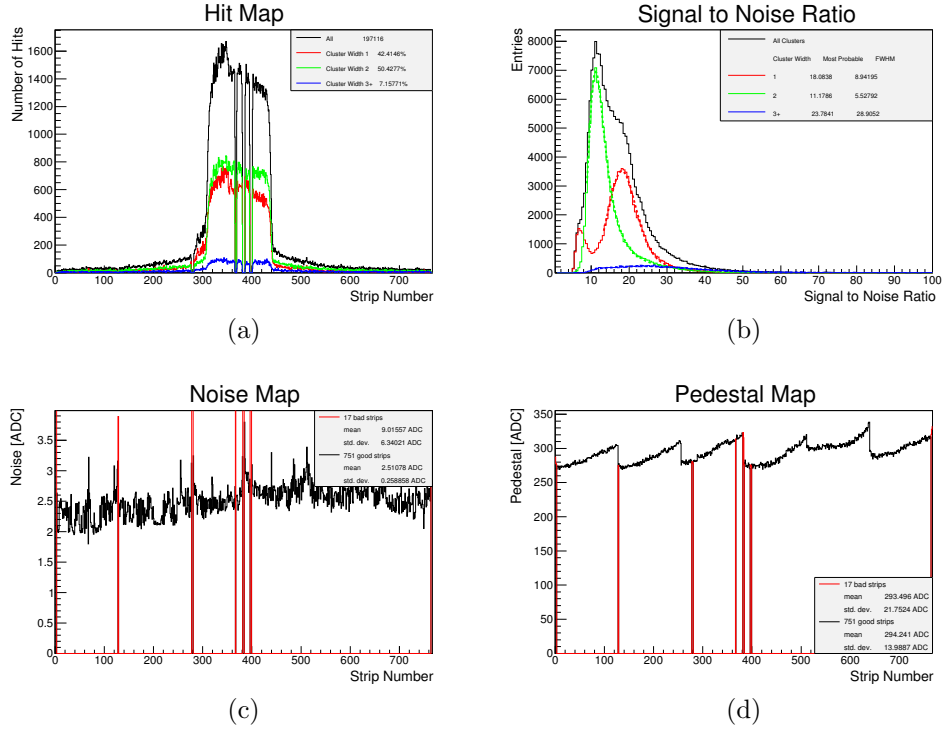Figure 3.6: Pos 4 ; FWD sensor ; n-side ; without cooling

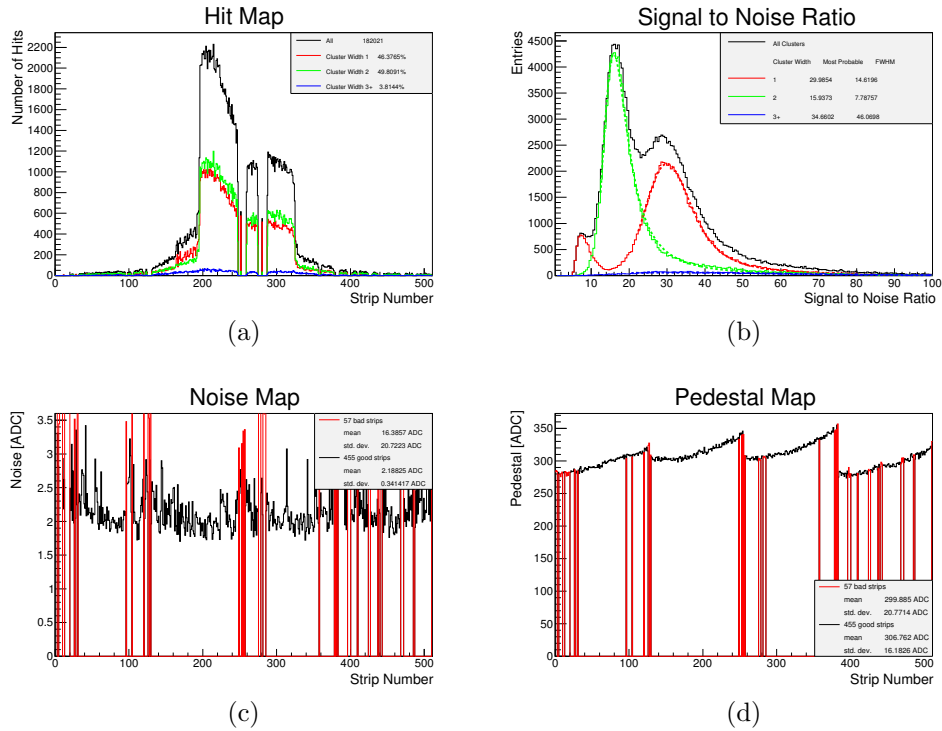Figure 3.7: Pos 3; CE sensor ; p-side ; without cooling

Figure 3.8: Pos 3; CE sensor ; n-side ; without cooling
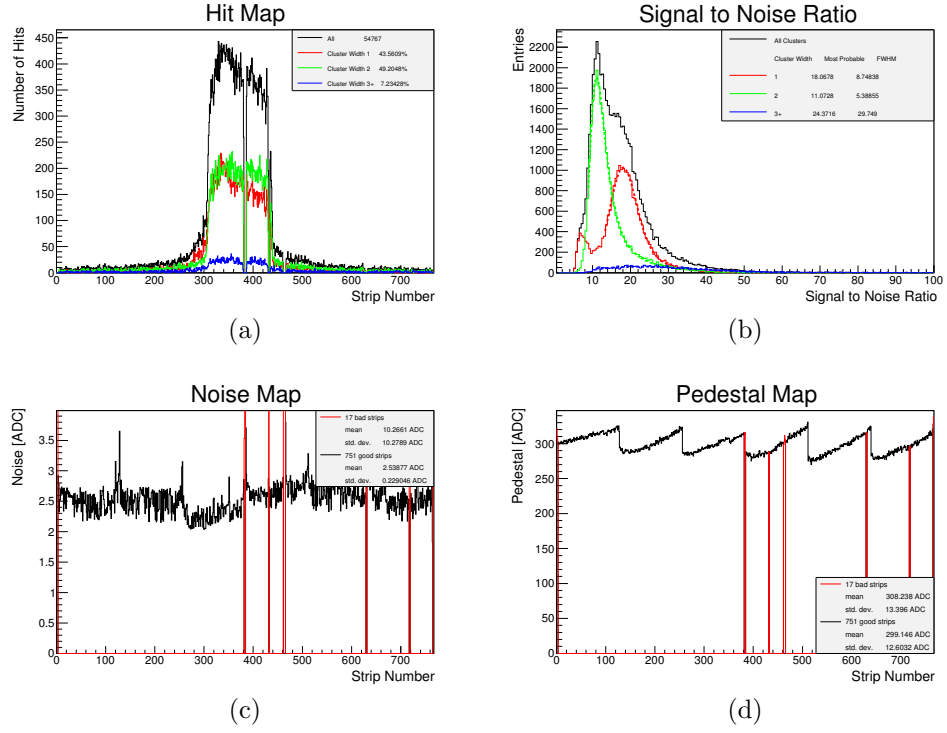
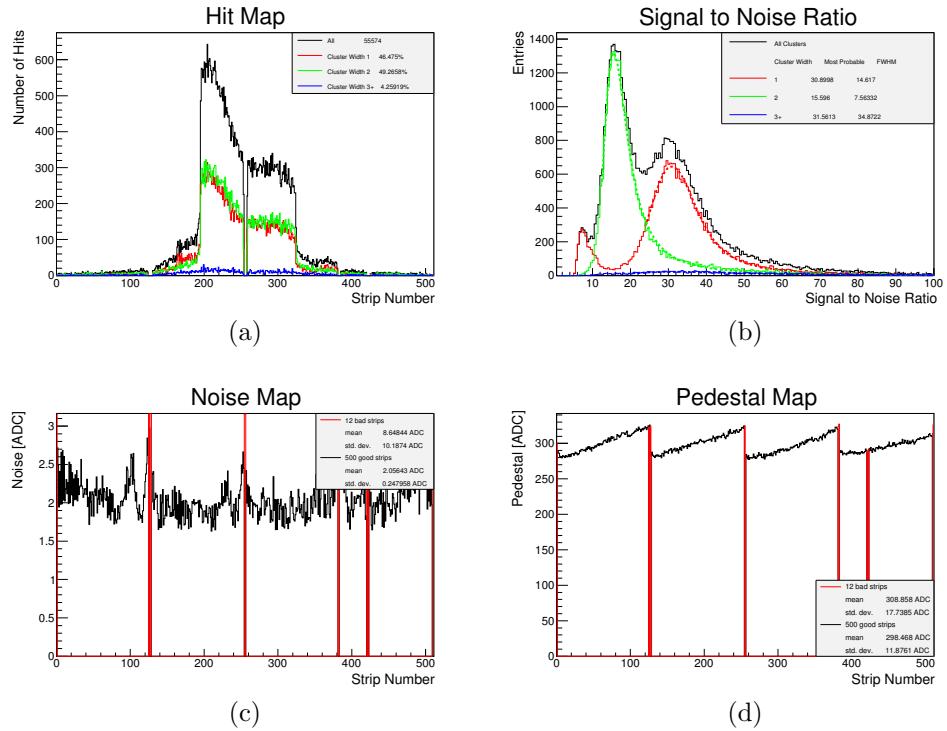Figure 3.9: Pos 2; -Z sensor ; p-side ; without cooling

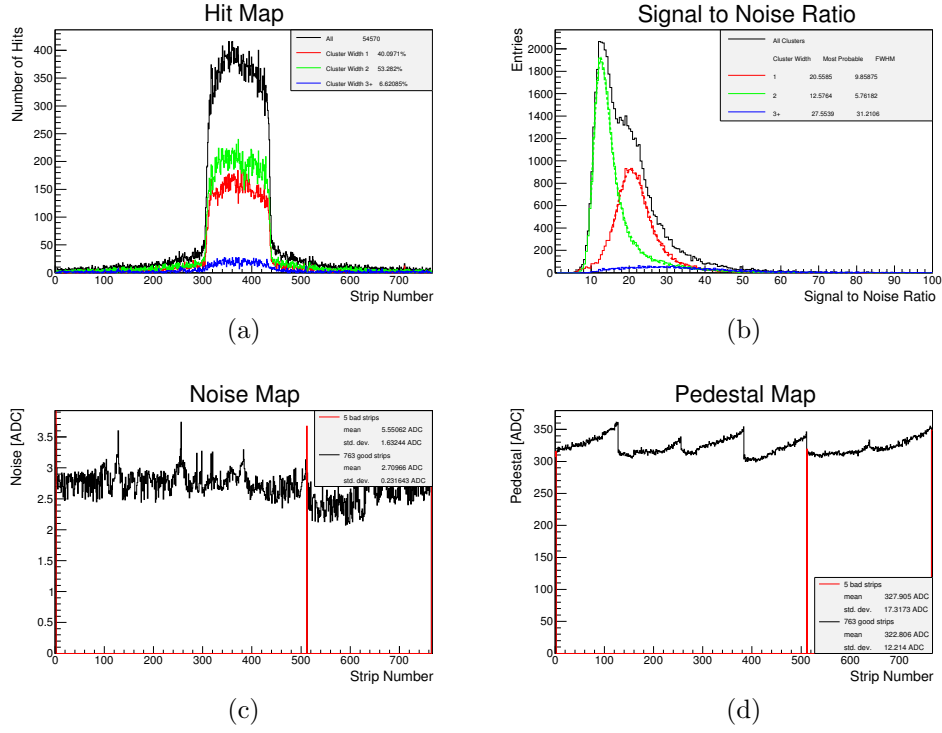Figure 3.10: Pos 2; -Z sensor ; n-side ; without cooling

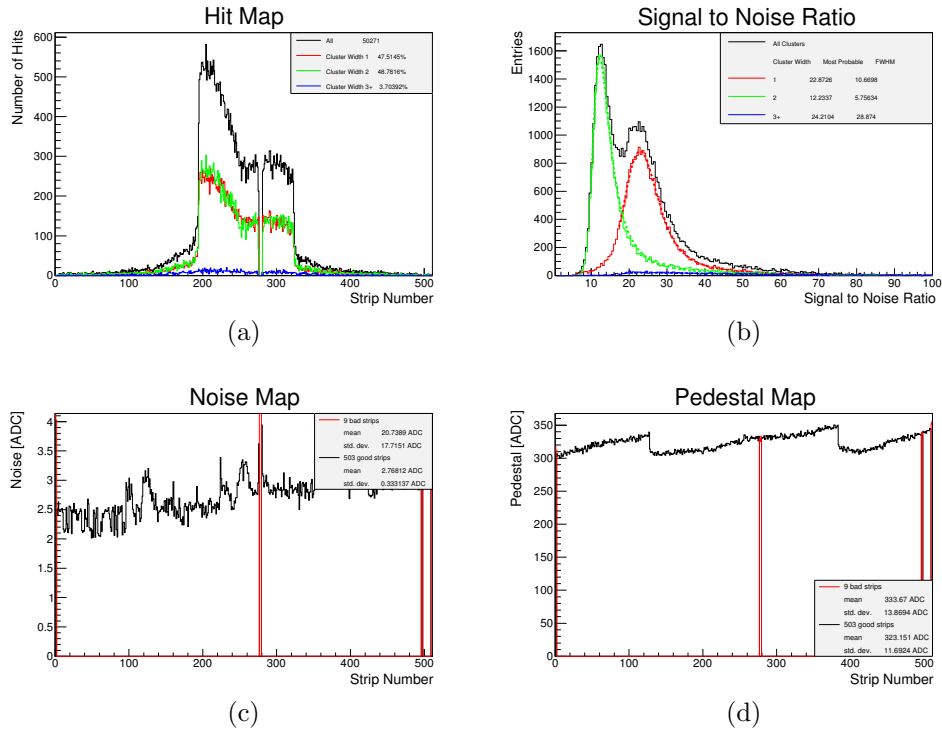Figure 3.11: Pos 1; BW sensor ; p-side ; without cooling

Figure 3.12: Pos 1; BW sensor ; n-side ; without cooling

As shown in figure 3.10b and 3.8b a SNR peak of cluster width 1 appears at about 8-SNR. This peak increased significantly, when the cooling was turned on. As a matter of fact this peak only appeared at the Origami modules (-Z and CE) and could not be ignored, as the filtered signals at < 12 SNR yielded to averaged shaper-pulse shown in figure 3.13c. These isolated signals could be interpreted as particle hits which should not arise at such low SNR. After some investigation it appears that these "phantom signals" always originated at a distance of 32 strips. This, in combination with the FIR filter, led to the ADC delay scan. Due to the fact that exactly the same Cern setup could not be recreated, we started to measure the L5.903 ladder with the LTS by adjusting the ADC-delay very accurately. The result (figure 6.1.5) shows that the 8 SNR peak was gone. Furthermore the peak could be reproduced by setting wrong ADC-delay parameters on purpose. The reason for the higher SNR with the cooling can be explained by noise reduction at lower temperatures.
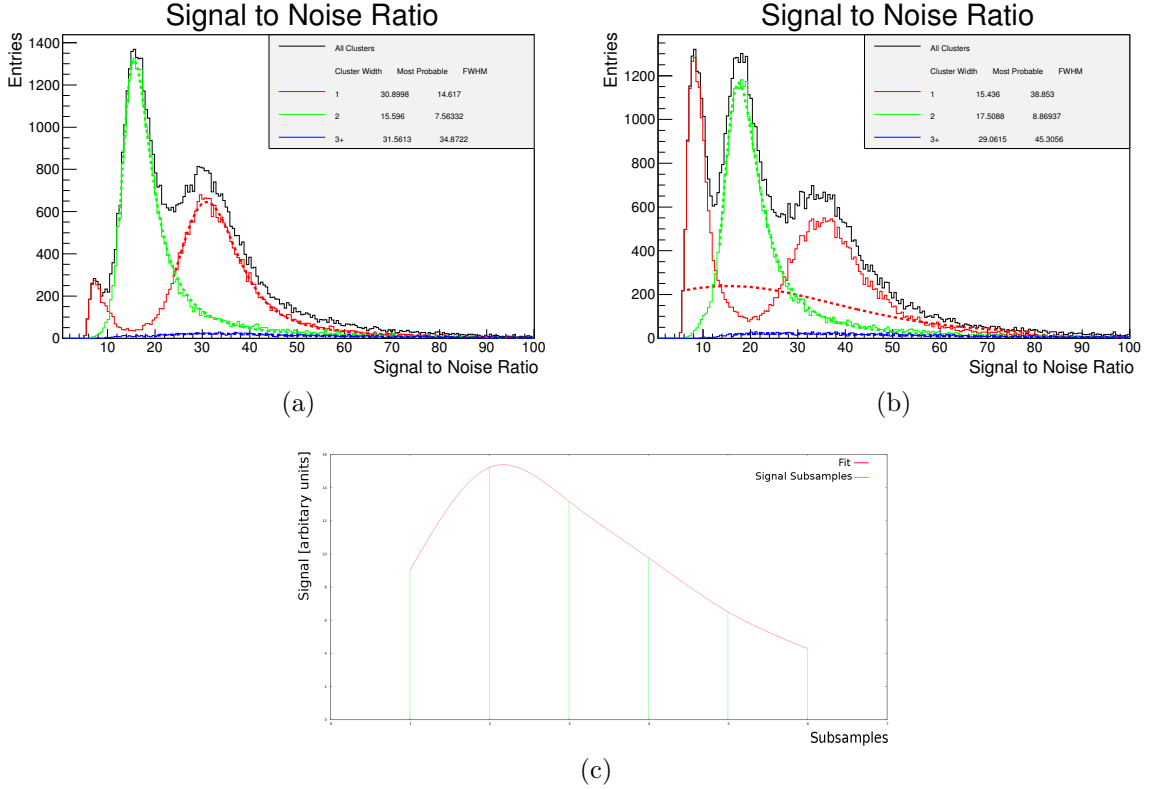

(a)

(b)

(c)

Figure 3.13: (a) shows the 8 SNR peak without cooling at -Z n-side; (b) shows the 8-SNR peak with cooling at -Z n-side which increases to a level causing the Landau-Gauss fit to fails; (c) shows the averaged shape of all signals $<$ than 12 SNR. This can be interpreted as a valid signal

Special attention was paid on the SNR with cooling. One reason to cool the ladder is to extend the lifetime of the semiconductor components to the run time of Belle II. As the SVD has a power dissipation of approximately 602 W in a closed environment. Another reason is to improve the SNR. Figure 3.14 show, that the cooling has the assumed positive effect on the SNR. It improves the SNR of all sensors modules [34], especially of the origami-modules where the cooling pipe is directly attached to the APVs.
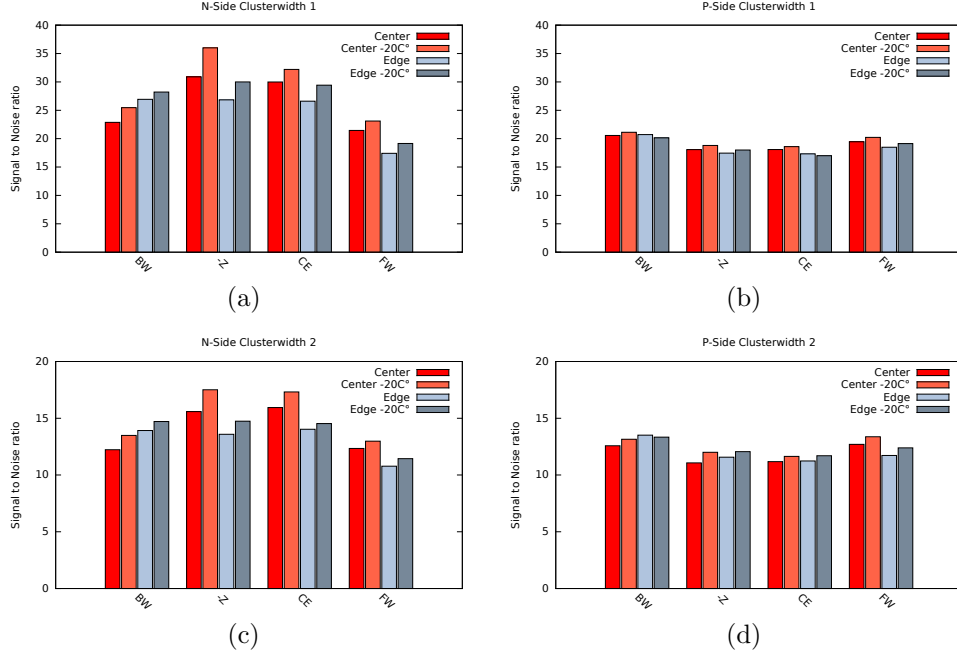

Figure 3.14: Signal to noise ratio of all sensors, cooled and not cooled; Edge represents the position 5-8 and center position 1-4 (see figure 3.3)

3.3 Pseudo telescope

The pseudo telescope was set up to carry out resolution measurements on a fully assembled L5 ladder. Its setup and orientation is adapted from the EU-telescope [11], which is a well known generic pixel telescope developed by DESY. For this reason the EU-telescope-framework was used for the analysis.
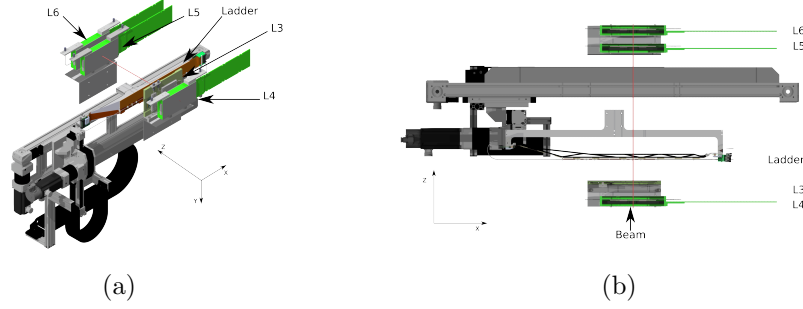

Figure 3.15: (a) oblique projection ; (b) plan view of the "pseudo telescope"

Plane	z-position
L4	0 mm
L3	49.80 mm
DUT	114.62 mm
L5	417.00 mm
L6	463.80 mm

Table 3.2: Distances of the detector planes; L4 is set as origin

3.3.1 Eutel-framework

The Eutel framework is an analysis and track reconstruction tool which is used to process raw data to complex objects such as particle tracks. The telescope consists of symmetric number planes which are used to track particles. It is important that these planes are precisely aligned to each other. Moreover, a Device Under Test (DUT) plane is placed in the center of the telescope planes. The resulting tracks are used to characterize both the telescope itself and any other position sensitive detector such as the DUT. In our setup the L5.903 ladder was used as DUT. The data format used in the EUTel-framework is LCIO (Linear-Collider I/O) [17] which is a multi layer event data model. It was developed in context of the International Linear Collider (ILC) and fits perfectly for storing EUTel data. When using the EU-telescope-framework one calls processors (Marlin) to process the data from a specific LCIO layer and save the processed data in the next higher one. As shown in figure 3.16 the low level objects are not needed in our test beam setup, because they are not compatible with the SVD readout chain.

Nevertheless it is possible to use the DAQ data at the Hitmaker level by providing the hit coordinates in the LCIO format. For this purpose the LCIOconv program was developed. For the sake of completeness i would like to mention that the processors are not uniquely defined. That means, which instance is loaded inside, for instance Hitmaker, is up to the user. The processor Hitmaker in our case using a fitter and a prealign instance, but it is possible to load any needed instance.

Figure 3.16: shows the EUTel framework strategy and the low level processes which are replaced by the SVD readout chain and the TuxDAQ.

LCIOconv

LCIOconv is a program written in C++ which converts the TuxOA data from root to the LCIO format. Furthermore it calculates the x coordinate from the n-side and y from the p-side of the DSSD. For calculating the coordinates it uses COG and Eta correction (see section 1.4.4). When determined, the coordinates of p and n-side are merged to a single detector plane with an x and y position by using the same event number. Moreover, the xy coordinates of all detectors are collected by matching the event numbers and then written into the LICO file. It has to be mentioned that, if one detector plane does not have the matching event number, the entire event will be dumped. That leads on the one hand to a small yield of finally used events, but on the other hand all used events have hits in all planes, i.e:

Additionally the LCIOconv calculates the true coordinates of the FW sensor. This is necessary, because of the trapezoid geometry and the slanted angle of 16°. The calculation is done in 6.3.1.

Detector Plane	ID	% used entries
L4	0	70.18
L3	1	72.11
DUT	10	88.86
L5	2	66.38
L6	3	78.93
All		23.56

Table 3.3: Runnumber 10 BW with cooling and 50K events

Hitmaker

The Hitmaker processer does, in case of the TuxDAQ data, prealign the Detector-planes by using the Gearfile. The Gearfile contains detector ID, geometrical, material and resolution information about the detector planes. Thus, Hitmaker converts the local to global coordinates and further calculates the offset of the planes by using correlation data. Afterward the modified alignment constants are saved in a new prealigned Gearfile. Furthermore hit candidates are sorted out by defined residual limits for the correlation band.

Alignment

The Alignment process takes the prealigned Gearfile and uses a DAF-Fitter to get particle tracks. The Deterministic Annealing Filter (DAF) [16] is an enhancement of he Kalman Filter (KF) [20] by using weighted measurements. A deterministic system can be described with k as discrete time index:

$$\widetilde{\mathbf{x}}_k = \mathbf{F}_{k-1}\mathbf{x}_{k-1} + \mathbf{G}_{k-1}\mathbf{u}_{k-1} + \omega_{k-1}$$
$$\mathbf{m}_k = \mathbf{H}_k\widetilde{\mathbf{x}}_k + \mathbf{v}_k \tag{3.1}$$

$\widetilde{x}_k$ is the true (unknown) state, u the input and ω the random noise vector. F is the propagator and G the input matrix. $\mathbf{m}_k$ is a controllable output (measurement in plane k) vector and $\mathbf{H}$ the projector matrix. The index k is the number of measurements and hence related with time. k is used to differentiate between a expected $\mathbf{x}_k^{k-1}$ and an updated (filtered) $\mathbf{x}_k^k = \mathbf{x}_k$ state. Therefore, the time update function realizes the filter steps.

$$\mathbf{x}_k = \mathbf{x}_k^{k-1} + \mathbf{K}_k \underbrace{(\mathbf{m}_k - \mathbf{H}_k\mathbf{x}_k^{k-1})}_{residual} \tag{3.2}$$

$\mathbf{K}$ is the Kalman gain and indicates how residuals improve. The major aim of the Kalman filter is to minimize the expectation value $E(|\widetilde{x}_k - x_k|^2)$.

$$\frac{\partial E(|\widetilde{\mathbf{x}}_k - \mathbf{x}_k|^2)}{\partial \mathbf{K}_k} = \frac{\partial \operatorname{tr} \mathbf{C}_k^k}{\partial \mathbf{K}_k} = 0 \tag{3.3}$$

$\mathbf{C}_k^k$ is the covariance matrix of estimation $\mathbf{x}_k^k$. To improve $\mathbf{x}_k^k$ a smoother can be applied which runs through all KF filtered states and updates them by using the collected data ([15]). Hence the KF does not have the capability to choose or reject measurement, an enhancement has been implemented. The DAF uses weighted measurements $\mathbf{m}_k^i$ for the same k (i.e. many hits at one plane in the same event) combining it into effective $\overline{m}_k^i$.

$$\overline{\mathbf{m}}_k^i = \overline{\mathbf{V}}_k \sum_{i=1}^{n} p_k^i (\mathbf{V}_k^i)^{-1} \mathbf{m}_k^i$$

$$p_i = \frac{\phi(\mathbf{m}_i; \mathbf{H}\mathbf{x}; \alpha V)}{c(\alpha) + \sum_j \phi(\mathbf{m}_i; \mathbf{H}\mathbf{x}; \alpha V)} \tag{3.4}$$

ϕ takes the residuals into account and $c(\alpha)$ includes cut off parameter. Without deriving the weighting factor p_i further, there are two parameters, the χ_{CUT}^2 and the T annealing factor, which adjust the DAF. Where χ_{CUT}^2 affects the distance and T the measurement errors. Thus T smooth the probability of assigning a measurement with a defined χ_{CUT}^2. Firstly, DAF runs a Kalman filter with a smoother, then recalculates the weights in respect of the distance of an estimated smoother and the real measurements. This has to be done iteratively because the initial information of the state vector may be insufficient. The actual alignment process is using the Millepede II (MPII) algorithm [6]. It is based again on solving a least square problem with the difficulty of having two sets of parameters, both, local and global. The local one holds information about a single detector plane, while the global parameters have a set of information valid in all planes. Neglecting one set leads to a loss of accuracy in the alignment. For this reason MPII simultaneously "least-square-fits" all global and all local parameters. This yields to minimize χ^2, where $\mathbf{r}_i$ are the residuals and σ_i the predicted resolution, with $\mathbf{p}_0$ as initial alignment and $\mathbf{p}$ as alignment parameter:

$$\chi^2 = \sum_{i \in tracks} \left(\frac{\mathbf{r}_i}{\sigma_i}\right)^2$$

$$\chi^2(\mathbf{p}) = \chi^2(\mathbf{p}_0) + \left.\frac{d\chi^2(\mathbf{p})}{d\mathbf{p}}\right|_{\mathbf{p}=\mathbf{p}_0} \underbrace{(\mathbf{p} - \mathbf{p}_0)}_{\Delta\mathbf{p}} \tag{3.5}$$

$$\Rightarrow \frac{d\chi^2}{d\mathbf{p}} = 0$$

To simplify the notation the dependence of χ^2 on the track parameter $\mathbf{x}$ is not written in equation 3.5. Nevertheless, this requires solving the number of tracks equations packed

into matrix $\mathbf{C}$. $\mathbf{C}$ includes : $n \times n$ matrices C_{Global}, $m \times m$ matrices C_{Local} and $n \times m$ matrices $H_{\text{Local to Global}}$. The basic matrix equation is:

$$\underbrace{(\mathbf{J}^T \mathbf{V}_i^{-1} \mathbf{J})}_{C} \underbrace{\Delta \mathbf{p}}_{\Delta \mathbf{p} =} = \underbrace{\mathbf{J}^T \mathbf{V}_i^{-1} \mathbf{r}_i(\mathbf{p}_0)}_{\mathbf{b}} \tag{3.6}$$

$$\underbrace{\begin{pmatrix} \sum_{i \in tracks} \mathbf{C}_i^{Global} & \cdots & \mathbf{H}_i & \cdots \\ \vdots & \ddots & 0 & 0 \\ \mathbf{H}_i^T & 0 & \mathbf{C}_i^{local} & 0 \\ \vdots & 0 & 0 & \ddots \end{pmatrix}}_{C_{total}} \times \begin{pmatrix} \Delta \mathbf{p}^{global} \\ \vdots \\ \Delta \mathbf{p}^{local} \\ \vdots \end{pmatrix} = \begin{pmatrix} \sum_{i \in tracks} \mathbf{b}_i^{Global} \\ \vdots \\ \mathbf{b}^{local} \\ \vdots \end{pmatrix}$$

$$\tag{3.7}$$

$\mathbf{J}$ is the Jacobi matrix. To calculate the inverse martix $\mathbf{C}^{-1}$ in order to get $\Delta \mathbf{p}$. MPII splits the large matrix $\mathbf{C}$ into sub matrices by using the Schur-complement. These matrices are smaller and faster to calculate. After the alignment constants are calculated they are written into a new Gearfile.

Track Fitter

Track fitter uses the final Gearfile and runs the DAF-fitter again.

3.3.2 Resolution measurements

The ambition was to achieve resolutions that are better than the binary resolution(sec 1.4.4) of the sensors. The reason for improving the resolution is the $\eta - correction$ for cluster-width < 2. To resolution is measured via residuals (see 3.3.1) which show the difference between true hits and fitted track hits.Hits with Cluster-width > 2 are ignored because the current version of the TuxDAQ does not provide the signal height of the individual strips inside the cluster. This would, however, be necessary to apply the COG. Nevertheless, this does not have too much impact on the resolution, as the number of hits with cluster-width > 2 is small(see figure 3.23). A more sincere problem was the mechanical alignment which had not been paid much attention to as the intention was to eliminate the flaws with the software alignment. The problem was that there were no precise initial values to feed the MPII. This is particularly noticeable in small anti-symmetries of the residual. The precision of the alignment also increased with a bigger number of events to process. Finally all measured residuals were within the range of the expected values as shown below 3.17 - 3.20 (units in mm).

The $\eta - correction$ improves the resolution depending on the signal to noise ratio. The cooling improves the signal to noise ratio, thus, the resolution. Moreover, the signal to noise ratio is lower on the edges of the sensors (section 3.2).

$$\sigma \propto \frac{p}{SNR} \tag{3.8}$$

Detector Plane	$\sigma_N[\mu m]$	$\sigma_{Nbin}[\mu m]$	$\sigma_P[\mu m]$	$\sigma_{Pbin}[\mu m]$
BW	43.22	69.2	18.28	21.6
-Z	41.75	69.2	17.3	21.6
CE	41.14	69.2	18.27	21.6
FW	51.16	69.2	19.26	21.6...14.4

Table 3.4: Binary and measured resolution

Figure 3.21 shows the deterioration of the resolution on position 5(3.3) without cooling compared to position 1 with cooling.
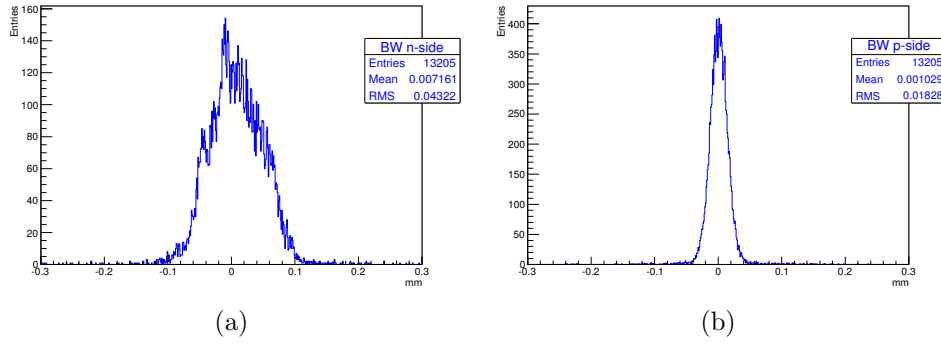

Figure 3.17: a and b position 1 BW sensor with 50k events
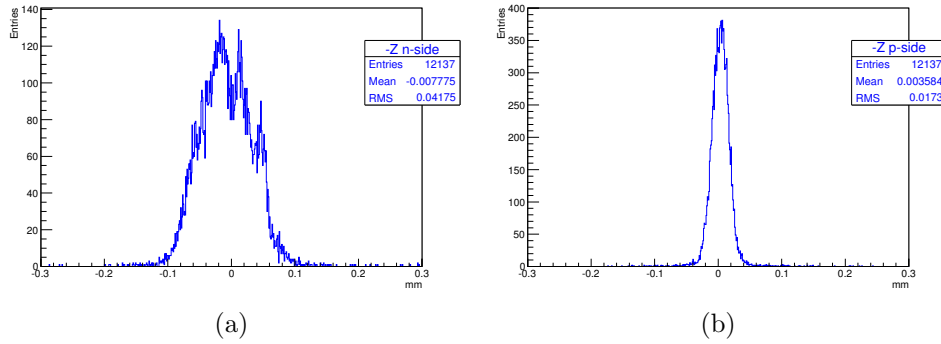
Figure 3.18: a and b position 2 -Z sensor with 50k events
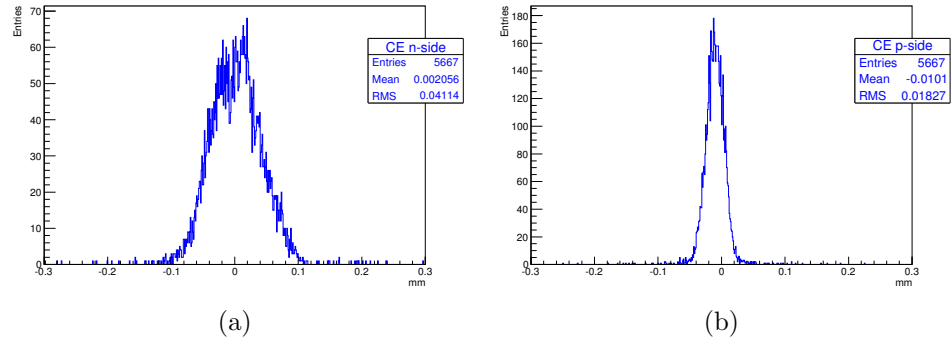
Figure 3.19: a and b position 3 CE sensor with 30k events
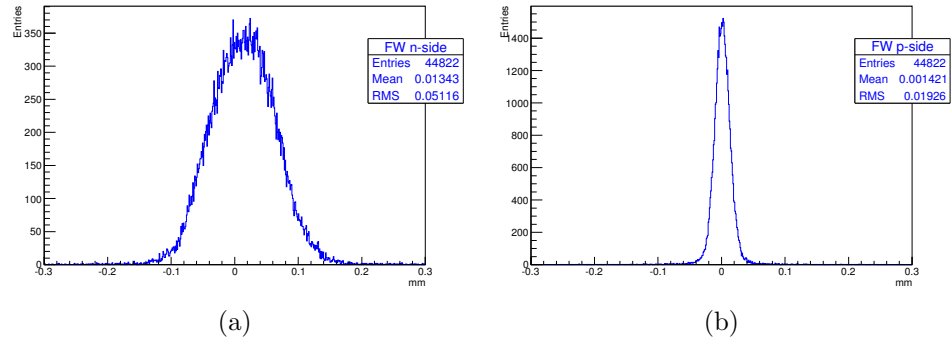
Figure 3.20: a and b position 4 FW sensor with 224k events
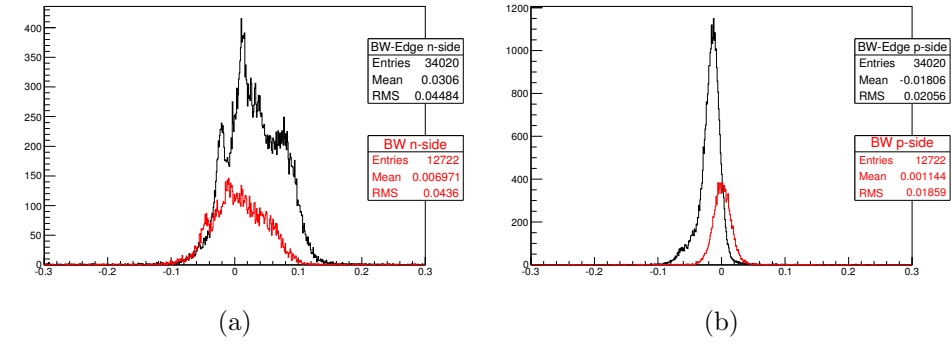
Figure 3.21: Residuals of BW Position 1 with 50k events, cooled, and BW-Edge position 5 with 200k events, not cooled; shows the dependence of resolution from SNR; The Edge residuals are still slightly misaligned.

3.3.3 Ghost-hit detection
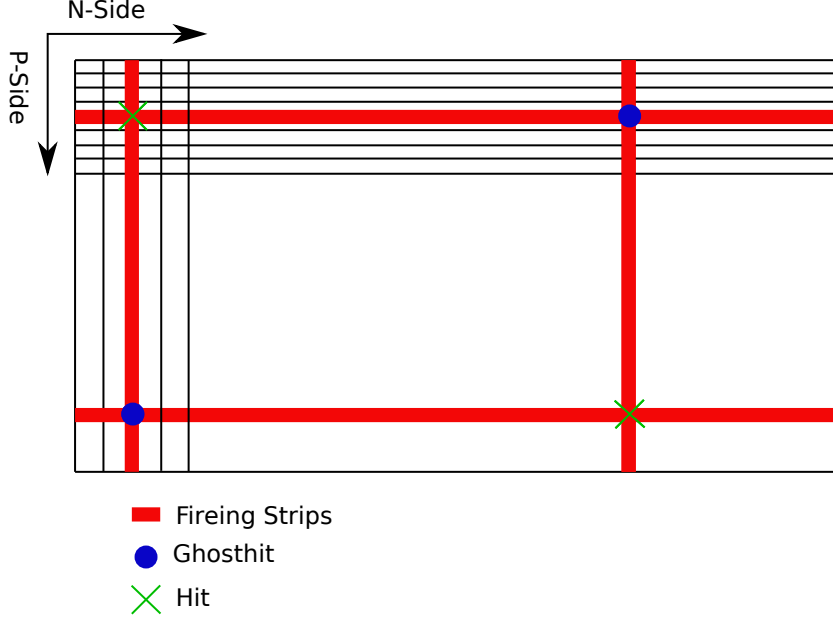
Figure 3.22: Illustration of the ghost-hit effect with two true hits.

With rising occupancy the probability of detecting two or more particles at the same trigger event is also increasing. If, for example, two simultaneous hits, that means two n-strips and p-strips firing at same time, are detected. This results in four strips crossings which leads to four hit coordinates (see figure 3.22) from which only two are true hits and the rest are ghost-hits. The number of ghost hits equals:

$$N_{ghost} = \sqrt{N_{Hits}} \tag{3.9}$$

N_{Hits} is number of hits. To resolve this problem there are two approaches[29].

- **Track fitting**: Sophisticated Track fitting algorithm such as the DAF-Fitter sort out hit candidates with a cutoff criteria.

- **Energy loss**: The signal of the hit is proportional to the charge created by the traversing particle in the silicon sensor. Therefore, it depends on the energy loss of the particle. Hence, the hits with the highest strip signals should be the true hits.

The ambition at this was to implement the energy loss approach into LCIOconv and test it. The algorithm combines all n- and p-side hits per event and sorts them by the signal. The signal value is calculated as mean value of both sides of the detector plane (e.g. BW). As shown in table 3.5 it is not possible that the two hit candidates with the highest signal are the true hits, because true hits can not have identical coordinates. The reason for this is that the energy differences between CW> 1 and CW= 1 is quite

significant. If a sensor plane has both types of CW and is merged, the hit with the bigger CW generally has more impact on the mean value which results in having the same coordinate with the highest signal values. Nevertheless, the hit with the highest signal still can be interpreted as a true hit. Comparing its coordinates with the rest, by using the criteria that true hits can not have identical coordinates, leaves only one possible hit. This approach is implemented into LCIOconv and has satisfying outcome as shown in figure 3.25.

Detector ID	Event #	X [mm]	Y [mm]	Z [mm]	Signal	# of Combinations
10	101	81.439	31.2272	0	43.5156	4
10	101	81.439	43.65	0	42.5059	4
10	101	75.6	31.2272	0	37.8528	4
10	101	75.6	43.65	0	36.8431	4

Table 3.5: Real data example from merged n and p-side by LCIOconv
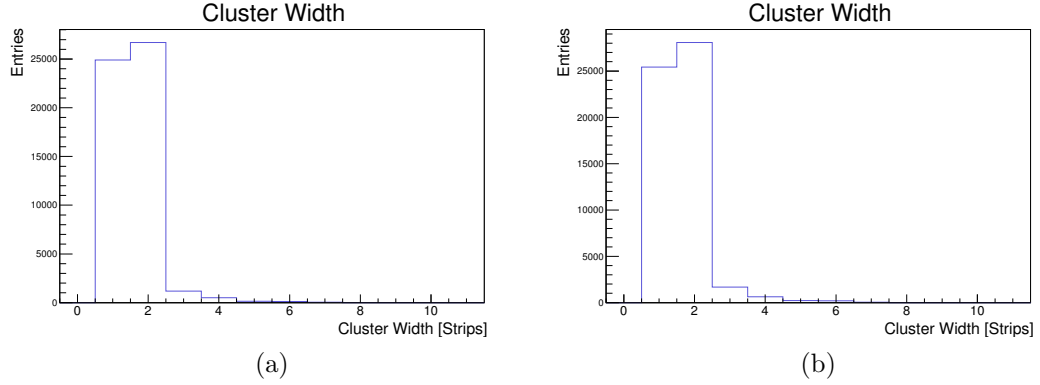
Figure 3.23: (a) BW n-side and (b) BW p-side ; shows the distributions cluster-widths; cluster-width 1 means only 1 strip is firing ;cluster-width = 2 is dominant; cluster-width > 3 reach a share of $\sim 3.9\%$ of total hits; these figures are representative for all sensor planes

The comparison of the energy loss with the tracker fit method yield to $\Delta\sigma_N = 0.38\mu m$ and $\Delta\sigma_P = 0.31\mu m$ which indicates a good, but not ideal success rate in reducing ghost-hits. An advantage is the reduced number of hits which could reduce the processing duration.
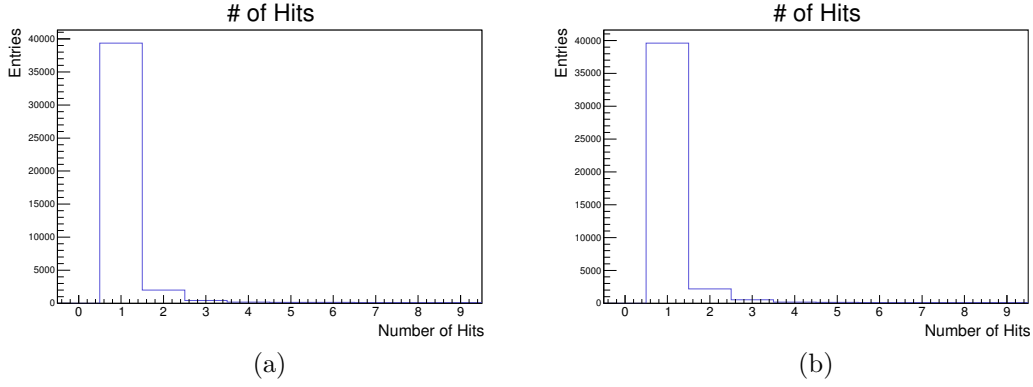
Figure 3.24: (a) BW n-side and (b) BW p-side ; shows the distributions of simultaneously detected hits; single hits are dominant; # of hits > 2 reach a share of ∼ 4% of total hits; this figures are representative for all sensor planes
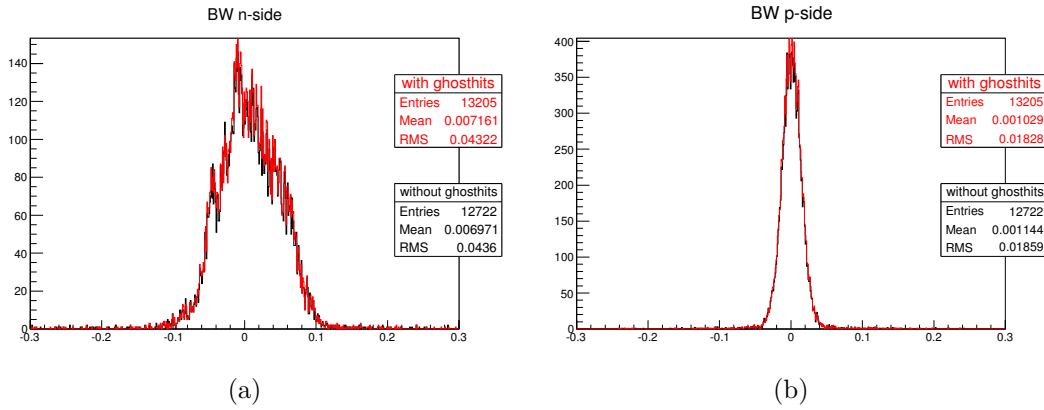

Figure 3.25: Comparison of energy loss (ghost-hit) and track fitter approach

4 Conclusions and outlook

The SPS test beam at Cern has been a success as it has proofed that the fully assembled ladder and the readout chain work as expected. The cooled ladder L5.903 had an improved signal-to-noise ratio. Furthermore, the Pseudo-Telescope was a test for tracking with original SVD detector parts and an assembled ladder. The results of the analysis show that tracking works, even if the setup is elementary. Due to alignment issues the resulting resolutions are improvable, but still inside of the expected ranges. The poor mechanical alignment of the pseudo-telescope planes are best seen at the FW sensor. The hit projection of the FW sensor which should be calculated (eq 6.1) with the slanted angle of 16° instead the best resolution is gained at 14°. This means we have a minimum deviation of 2° towards the beam. The comparison with the results of the measurements in H6B which used a conventional Mimosa Telescope with six telescope planes [33] shows, that better resolutions can be achieved. At the Mimosa Telescope the telescope planes are mechanically precisely aligned. Furthermore, the Mimosa planes are Mimosa26 pixel detectors with a pitch of $18.4\mu m$, thus they have naturally a better resolution than the SVD strip sensors. Nevertheless, the results of the resolution are comparable. The deviation between the two measurements of the Pseudo- and the Mimosa-telescope is $\Delta\sigma_N \approx 2\mu m$ and $\Delta\sigma_P \approx 5\mu m$ at the rectangular sensor.

The ghost hit detection algorithm works fine, but does not have a 100 percent success rate by using the energy loss approach. This is indicated by the slight deviation of the residuals (see figure 3.25). The advantage is the reduced number of hits. It is planned to implement the algorithm into BASF II to speed up the processing time of tracking particle by reducing the number of hit candidates.

Nevertheless the test beam revealed some minor issues such as the old experimental cooling system ALIX, which was difficult to handle and had insufficient cooling power. For that reason the ACBC was built. The ACBC has a cooling capacity of O(100 W) with 1 g/s mass-flow and 20 meters transfer lines. The ACBC GUI has many monitoring tools and keeps the cooling power at the needed level automatically. As soon as the tests had proven that the ACBC fulfilled the needed requirements it had been shipped to KEK for the ladder mounting in spring 2017.

After the SPS test beam in May 2016, a VXD test beam at DESY Hamburg was performed. All ladders of all layers of the SVD and PXD were mounted with a realistic geometry and cooled by Marco. Marco is a cooling device with a closed CO_2 system with less cooling power to the final Belle 2 cooling system. Its analysis is still ongoing as it was the first time PXD and SVD joined for a test beam with the collective data acquisition and monitor systems.

Furthermore, the ladder production at HEPHY is an ongoing process and recently reached the final class A quality standard. The LTS is already in use to test the func-

tionality in the assembled state. For the LTS it would be useful to create a config file writer to make the handling easier. The LTS could also be used for all ladder productions as a concept for testing fully assembled ladders.

5 Acknowledgement

Firstly, I am immensely grateful for DI Dr. Markus Friedl´s and Doz. DI Dr. Christoph Schwanda´s support. Being my supervisors, they have given me the opportunity to work on a truly interesting albeit, challenging topic and providing me with enriching and valuable feedback in the course of my research.

Furthermore, I would like to thank the the HEPHY-Team, especially Florian Buchsteiner, Hao Yin and Richard Thalmeier for the inspiring discussions, for the sleepless nights at test-beams, and for all the fun times we have had for the last two years.

My warmest thanks belong to my parents for their dedication and the many years of support. Without them I would not have been able to finish my studies.

Last, but not least, I would like to thank Jenny for her understanding, encouragement and her unconditional support throughout this thesis and life in general.

6 Appendix

6.1 LTS

6.1.1 Configuration file
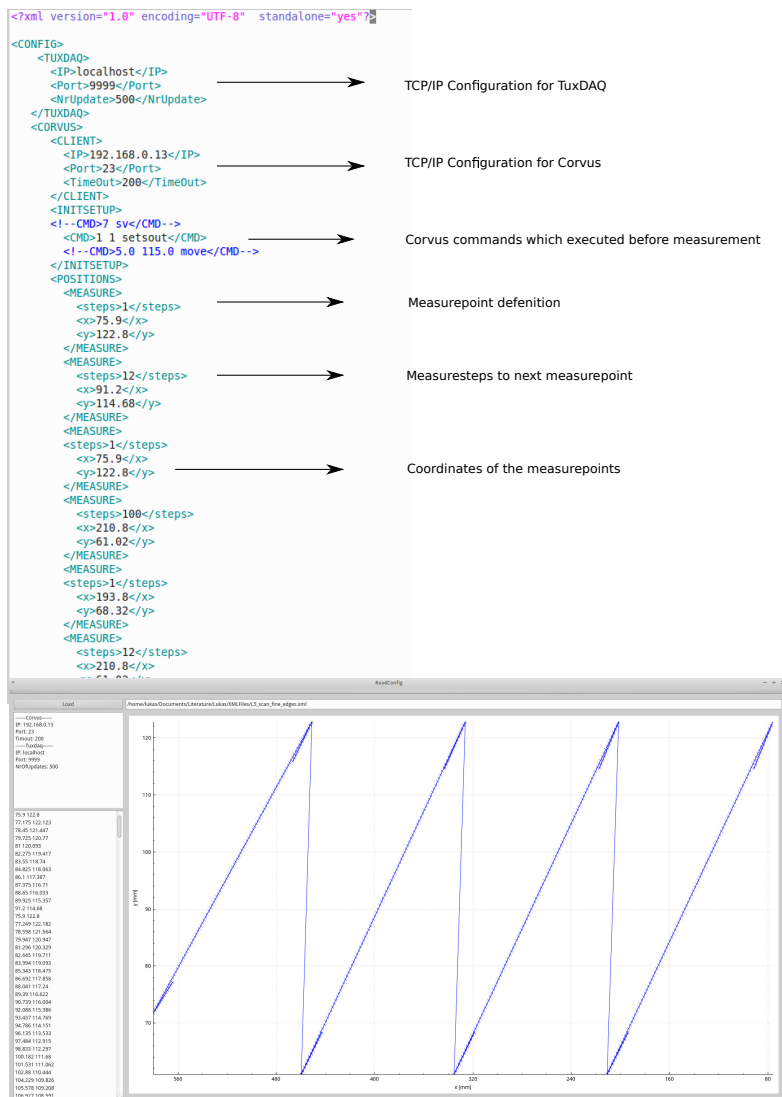
Figure 6.1

6.1.2 Corvus commands

LTS GUI communicates with strings to the Corvus. The terminating character after a command is carriage return linefeed. The set of commands for the Corvus is called VENUS.

- Activate the joystick: 1 j

- Set break : 1 1 setsout

- Release break : 1 0 setsout

- calibration moves to the origin : cal

- move to x = 10 y = 10 : 10 10 move

- returns the the actual position: pos

6.1.3 TuxDAQ commands

LTS GUI communicates with unsigned 32 bit integers to the TuxDAQ.

- CONFIGURE = 0x10000000;

- ACK = 0x11000000;

- EXECUTE = 0x20000000

- PERFORMED = 0x21000000

- FINISH = 0x30000000

- STOP = 0x40000000

- ERROR = 0x50000000

6.1.4 Full ladder runs

Full ladder runs with L5.903 with *L5_scan_fine_edges.xml*.
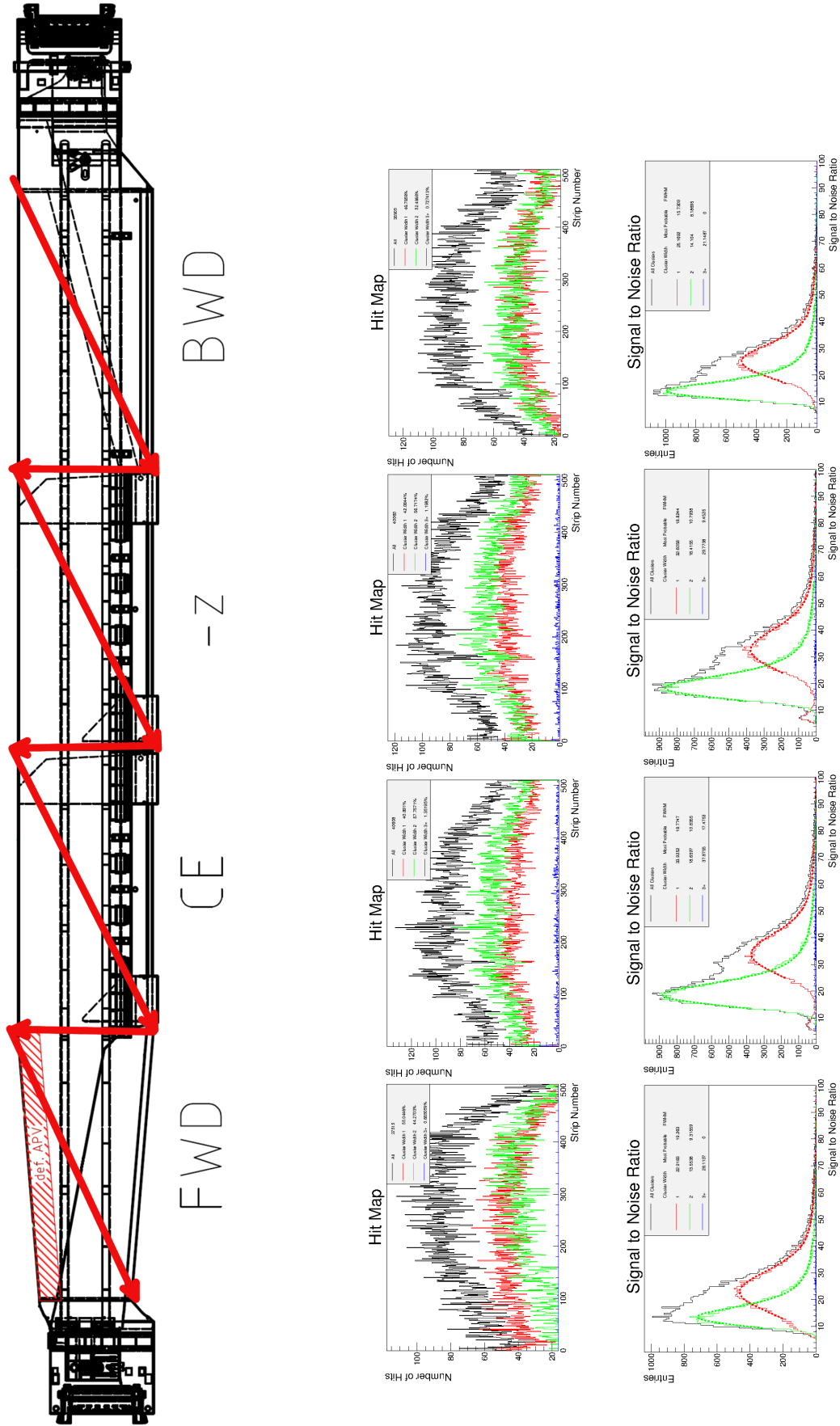
Figure 6.2: *L*5.903 N-side
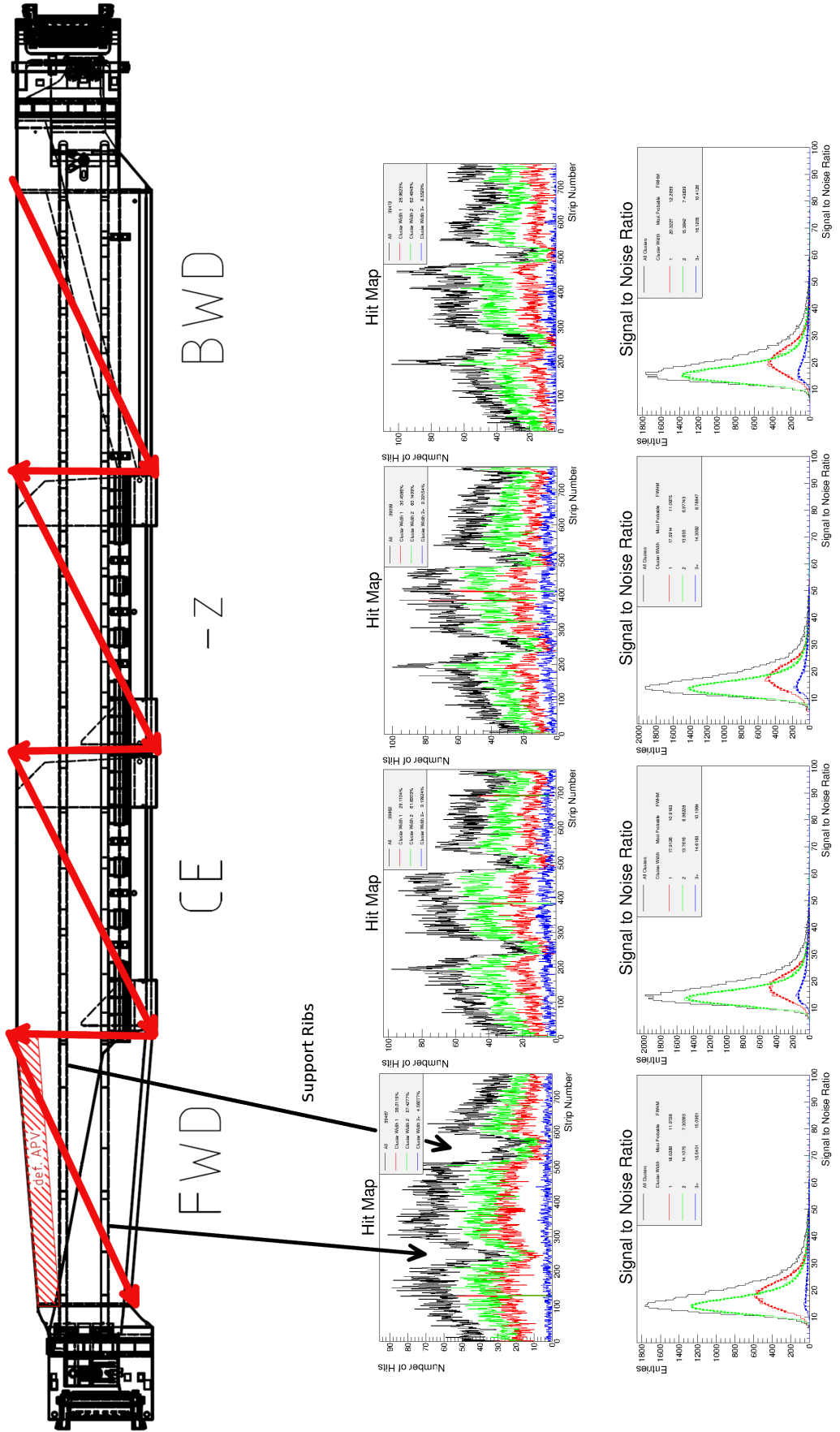
Figure 6.3: L5.903 P-side; The gaps in the hitmap are a shadow of the support ribs.

6.1.5 ADC-delay test runs
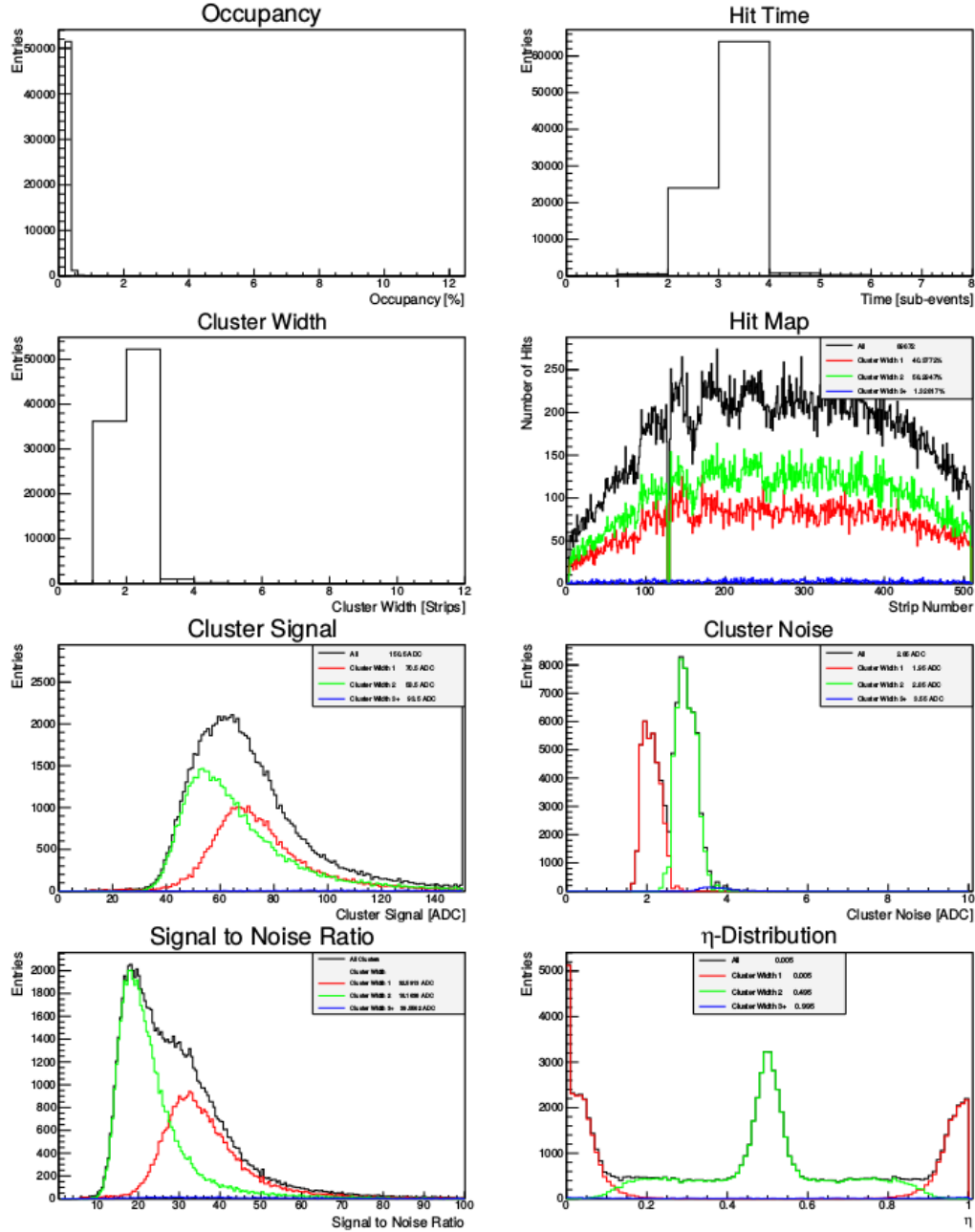
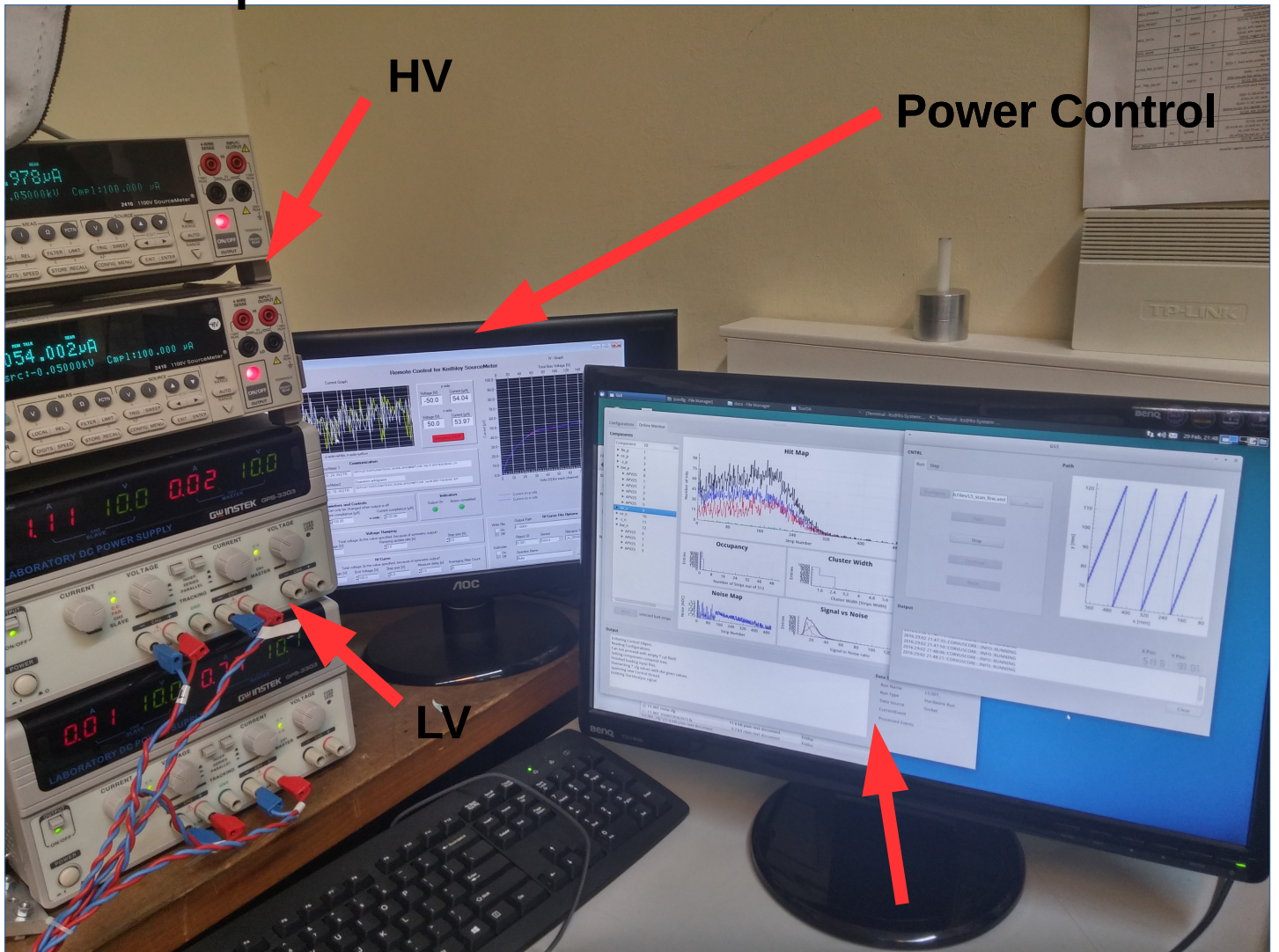Figure 6.4: L5.903 n-side measurement with LTS; 10000 events with 10 steps
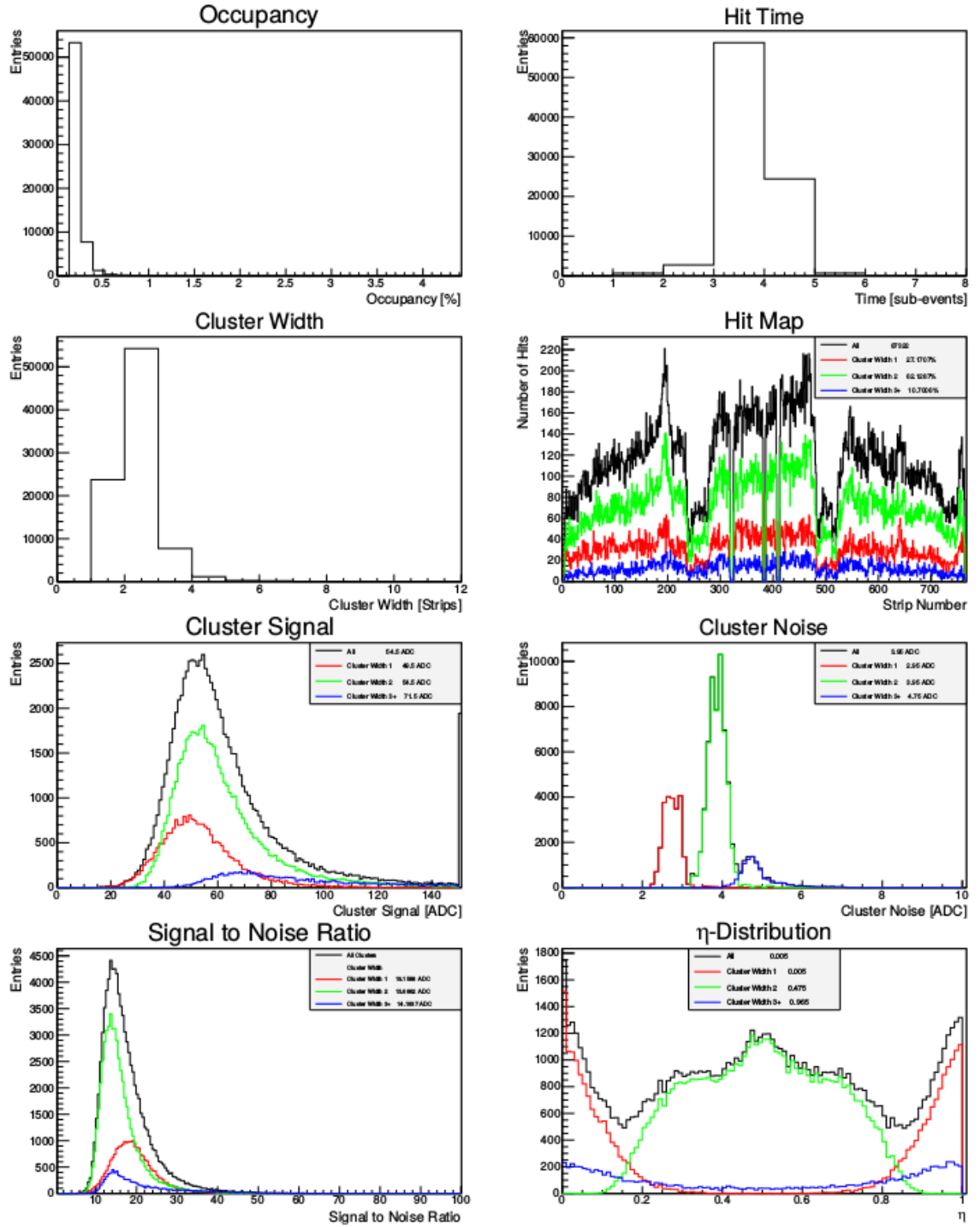
Figure 6.5: L5.903 p-side measurement with LTS; 10000 events with 10 steps

LTS Setup:

HV

Power Control

LV

LTS, TuxDAQ, TuxOA

^{90}Sr Source

Remaining ladder transport case

Ladder

Scintillator
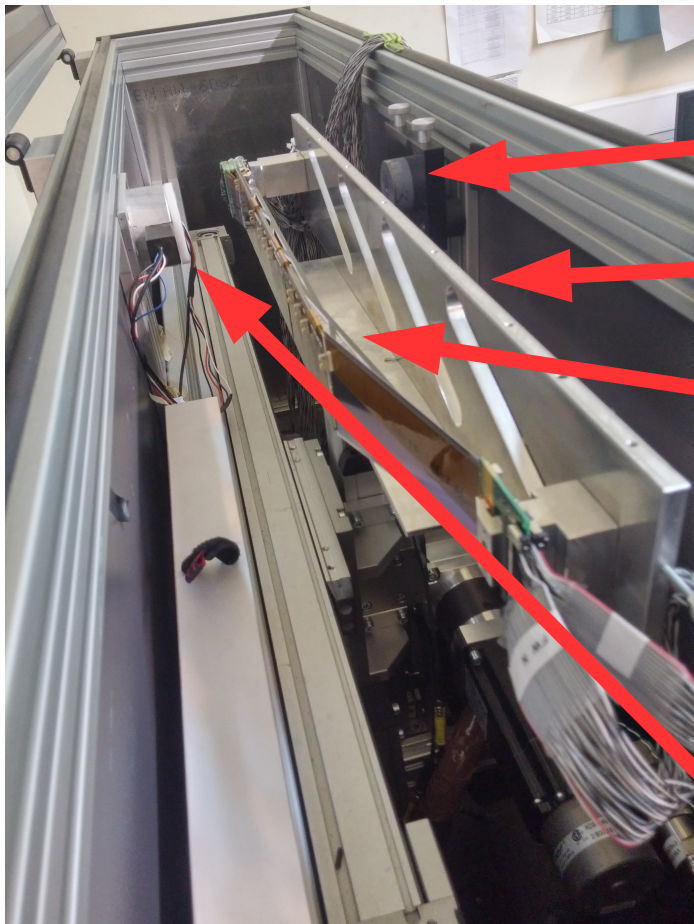
6.2 ACBC

6.2.1 CO_2 **diagramms**
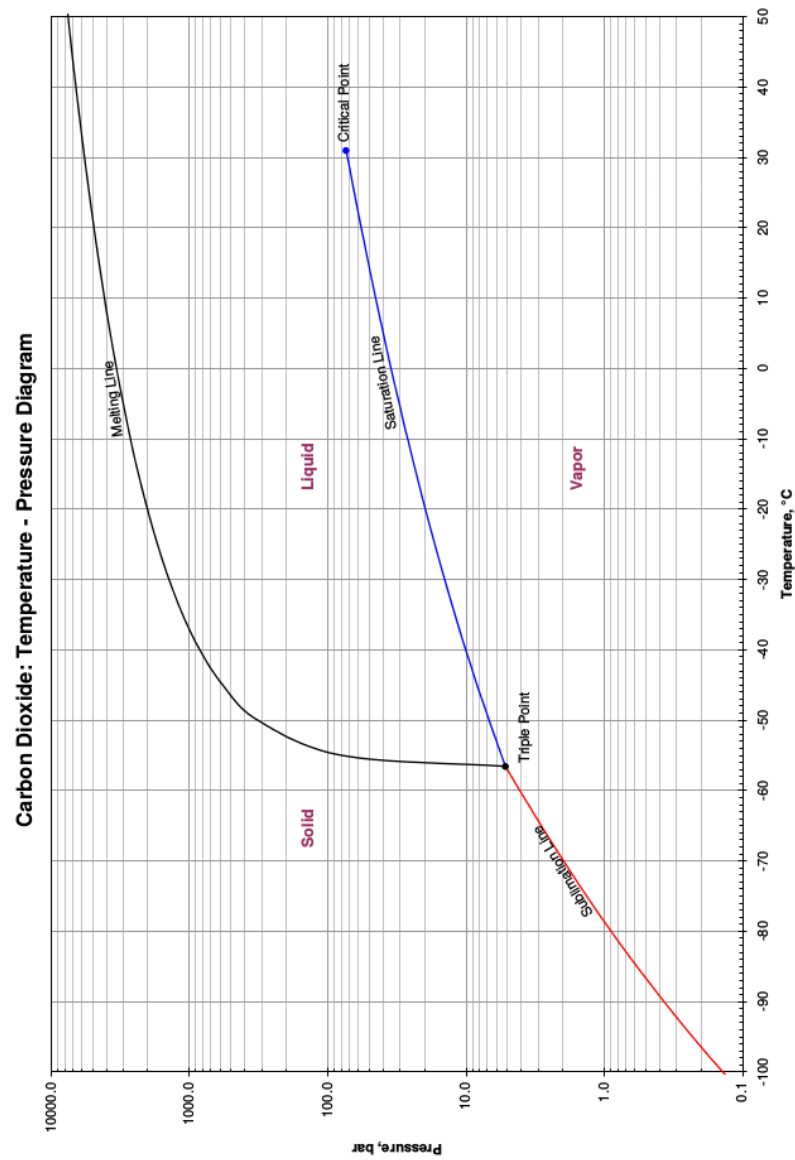
Figure 6.6: CO2 P-T diagramm
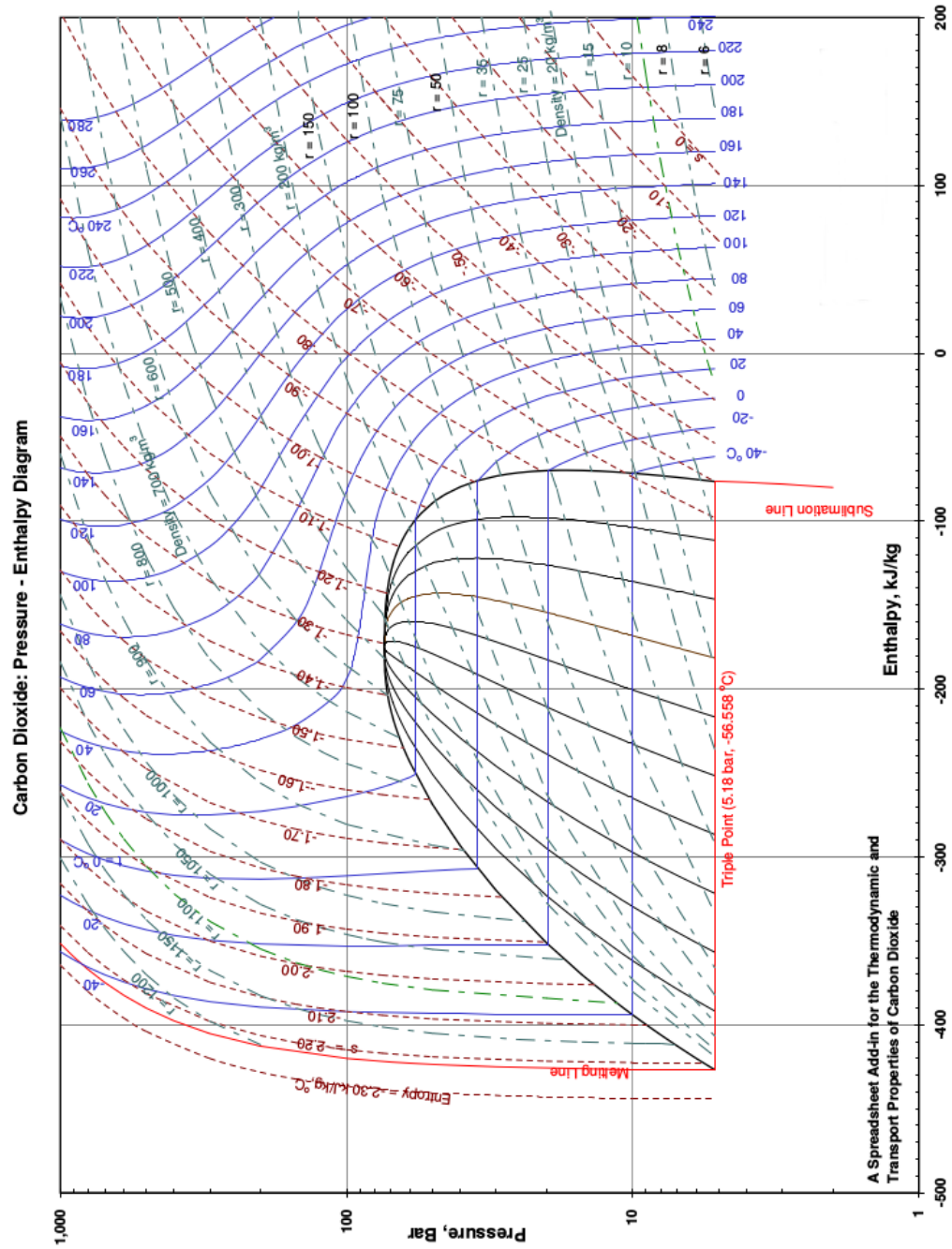
Figure 6.7: CO2 Mollier chart

6.2.2 ACBC GUI
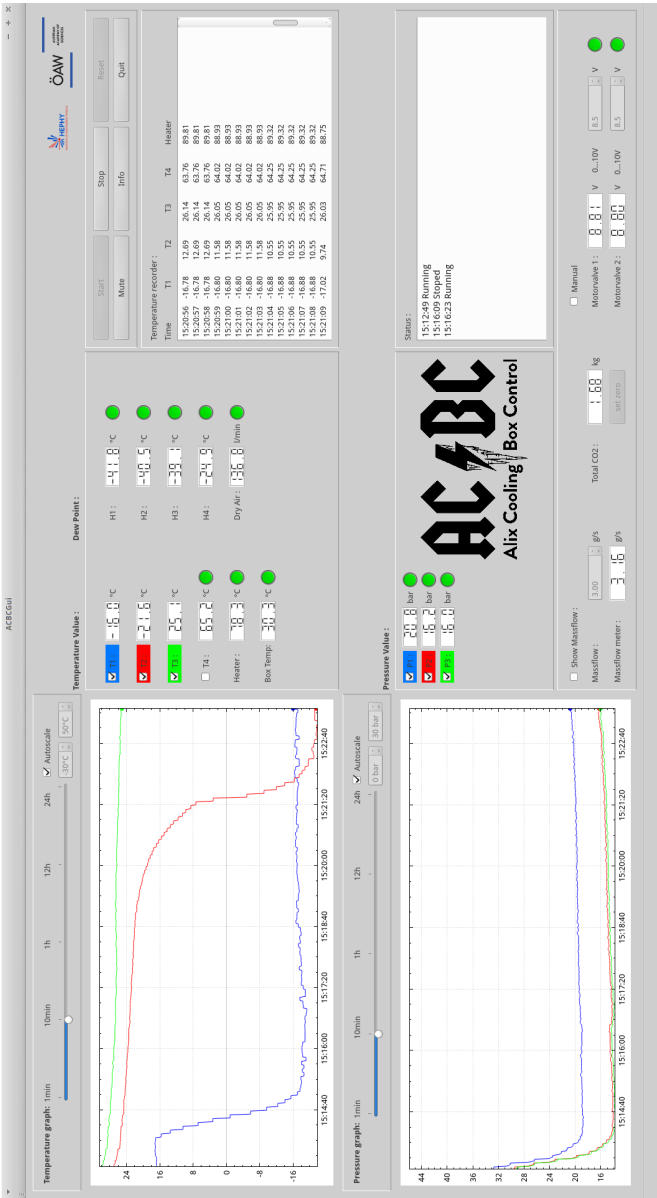
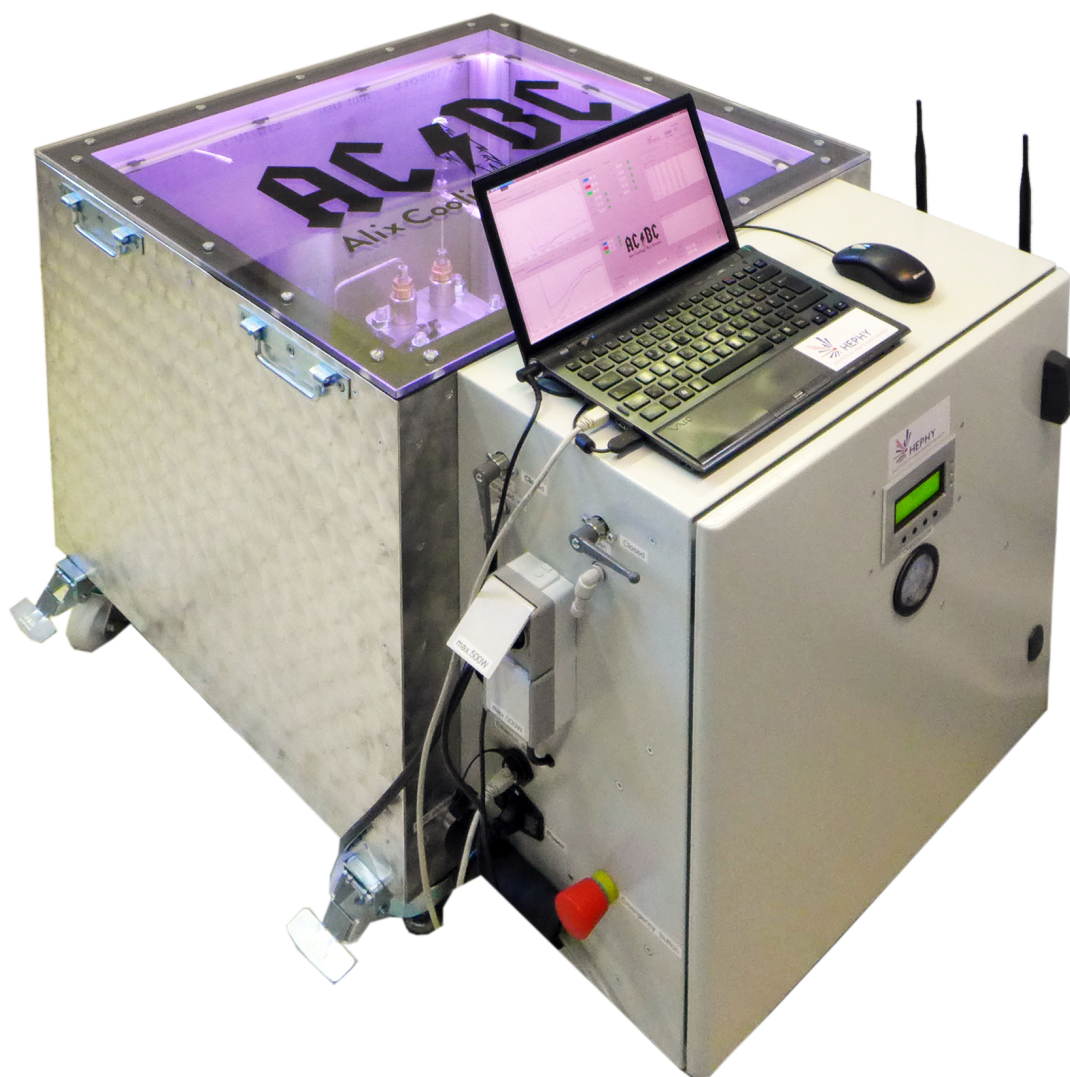
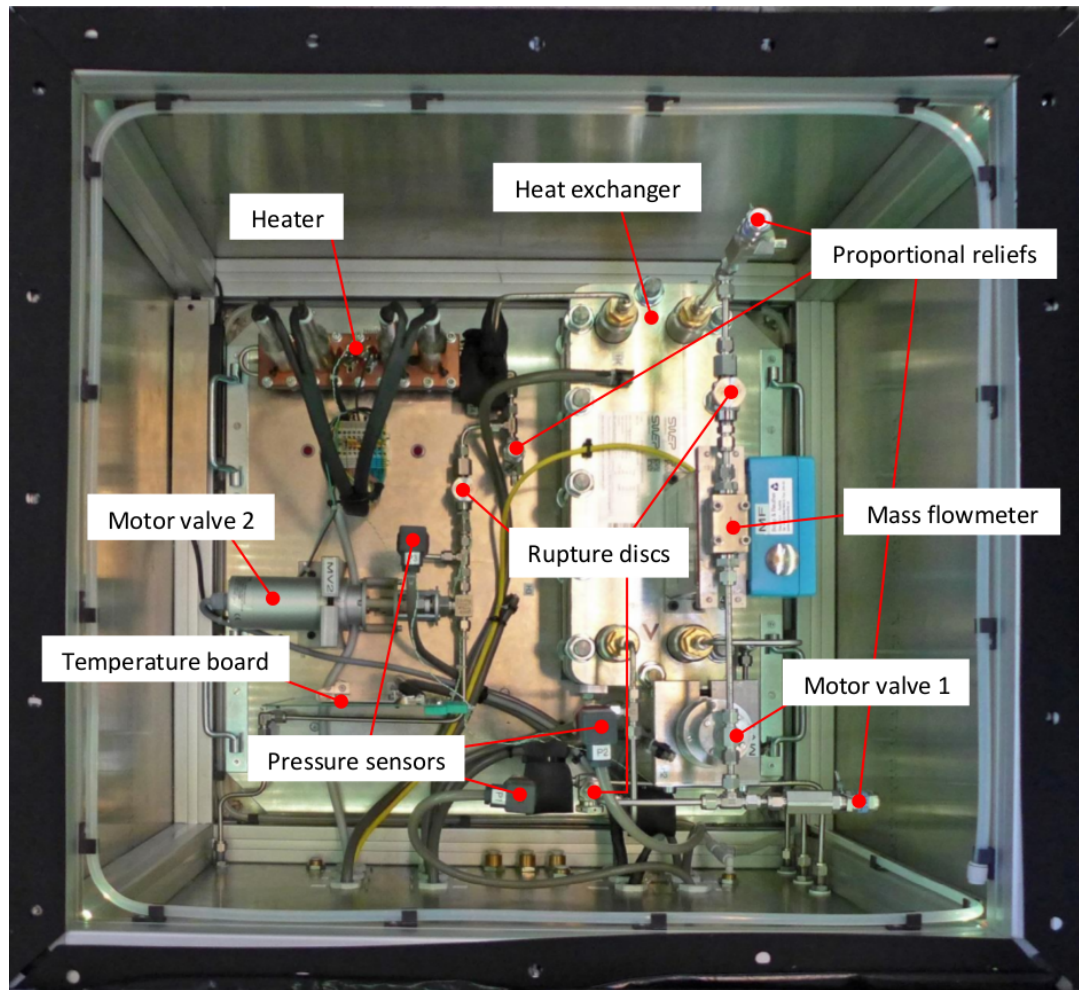Figure 6.8: GUI of the ACBC while running a test

Figure 6.9: ACBC

Figure 6.10: ACBC view inside the cooling box with components

6.3 CERN-Test-Beam
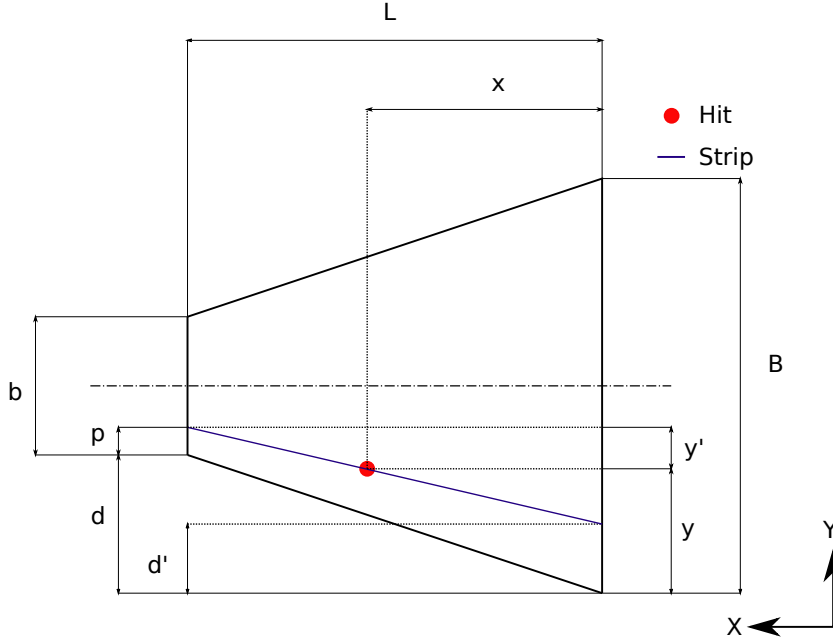
6.3.1 Trapezoidal coordinates

Figure 6.11

$$p \leq \frac{b}{2} \ :$$

$$tan(\alpha) = \frac{y'}{L-x} = \frac{d+p-d'}{L}$$

$$\Rightarrow y' = (d+p-d')\left(\frac{L-x}{L}\right)$$

$$d' = \frac{Pitch_{big}}{Pitch_{small}}p = \frac{3}{2}p \tag{6.1}$$

$$y = d+p-y' = d+p-\left(d-\frac{p}{2}\right)\left(1-\frac{x}{L}\right)$$

$$p \geq \frac{b}{2} \ :$$

$$y = d+p+y'' = d+p+\left(\frac{p}{2}-d\right)\left(1-\frac{x}{L}\right)$$

Projection to the plane orthogonal to the beam direction with the slant end angle γ:

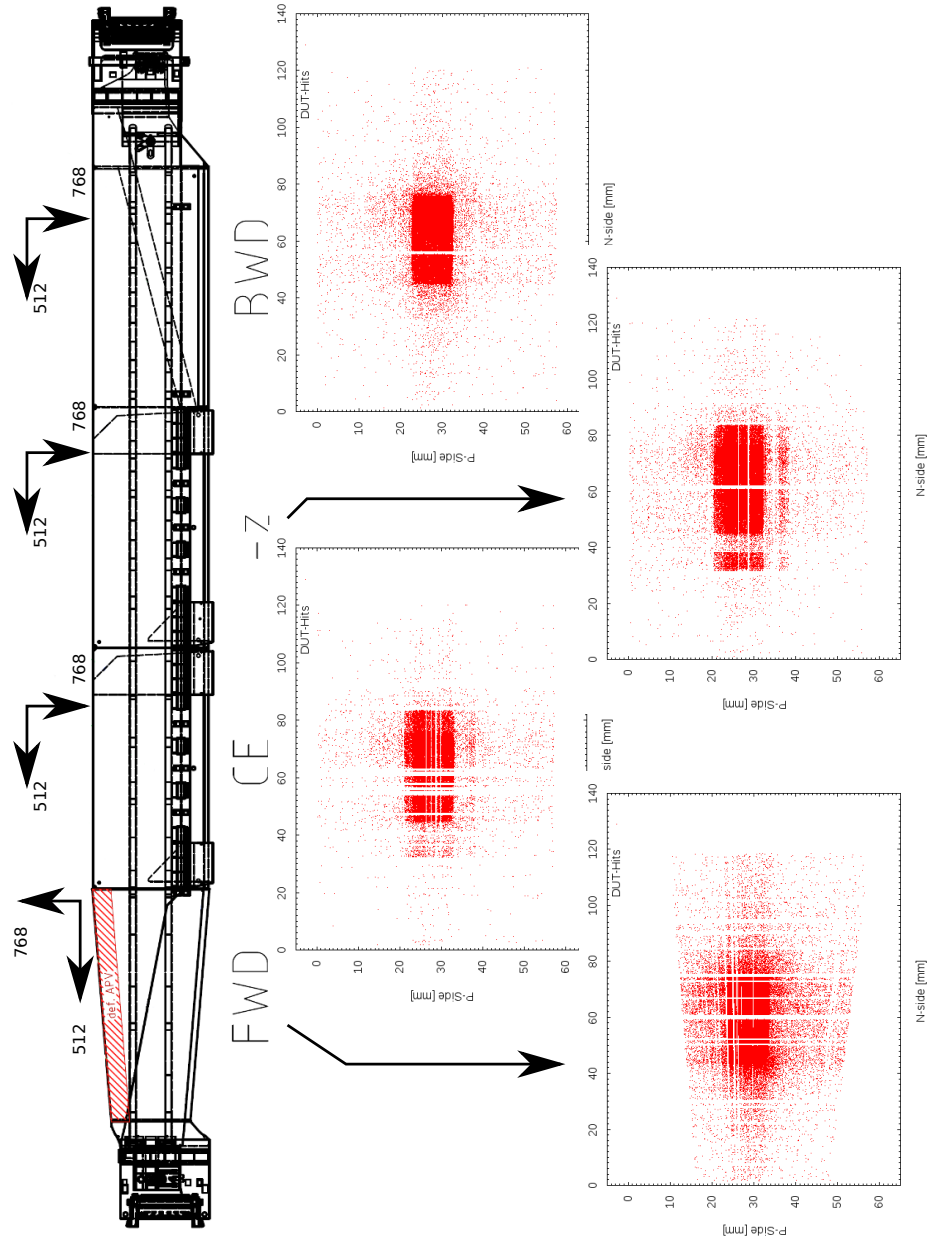$$cos(\gamma) = \frac{x_{projected}}{x_{true}} \tag{6.2}$$

6.3.2 Beam hit-maps

Figure 6.12

The hit-map area is small because of the scintillator size of the trigger. The size of the scintillator is $10 \times 20mm$.
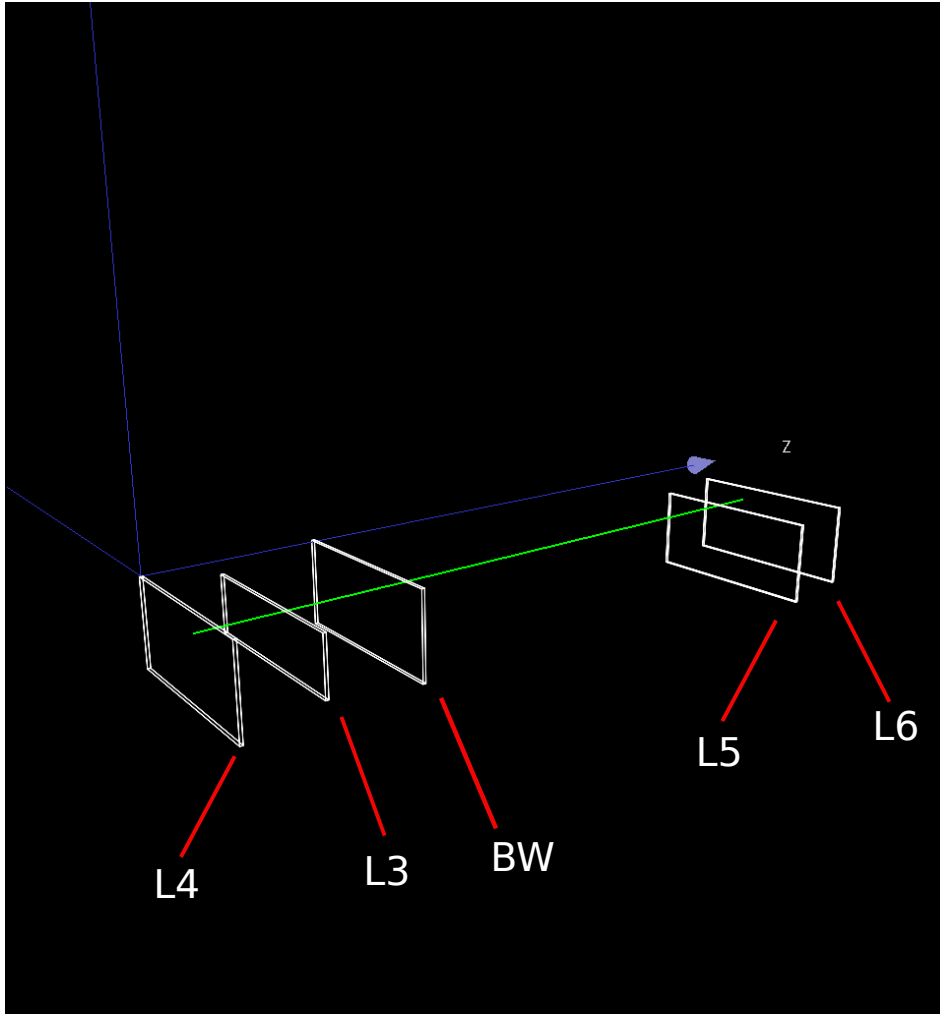
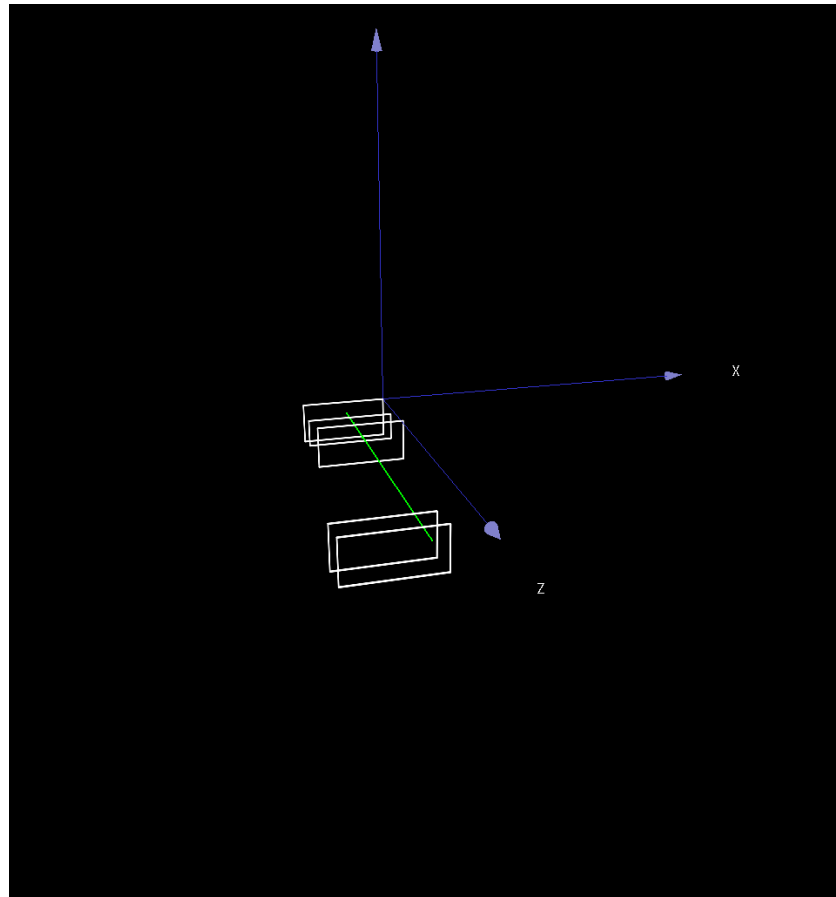Figure 6.13: Shows a track reconstructed from the "pseudo" telescope

Figure 6.14: Shows a track reconstructed from the "pseudo" telescope in BW direction

Bibliography

[1] A Abashian, K Gotow, N Morgan, L Piilonen, S Schrenk, K Abe, I Adachi, JP Alexander, K Aoki, S Behari, et al. The Belle detector. *Nuclear Instruments and Methods in Physics Research Section A: Accelerators, Spectrometers, Detectors and Associated Equipment*, 479(1):117–232, 2002.

[2] T Abe, I Adachi, K Adamczyk, S Ahn, H Aihara, K Akai, M Aloi, L Andricek, K Aoki, Y Arai, et al. Belle II technical design report. *arXiv preprint arXiv:1011.0352*, 2010.

[3] T Aushev, W Bartel, A Bondar, J Brodzicka, TE Browder, P Chang, Y Chao, KF Chen, J Dalseno, A Drutskoy, et al. Physics at super B factory. *arXiv preprint arXiv:1002.5012*, 2010.

[4] E Barberis, N Cartiglia, C LeVier, J Rahn, P Rinaldi, HF-W Sadrozinski, R Wichmann, T Ohsugi, Y Unno, H Miyata, et al. Capacitances in silicon microstrip detectors. *Nuclear Instruments and Methods in Physics Research Section A: Accelerators, Spectrometers, Detectors and Associated Equipment*, 342(1):90–95, 1994.

[5] AJ Bevan, B Golob, Th Mannel, S Prell, BD Yabsley, H Aihara, F Anulli, N Arnaud, T Aushev, M Beneke, et al. The physics of the B factories. *The European Physical Journal C*, 74(11):1–928, 2014.

[6] V Blobel. Millepede II linear least squares fits with a large number of parameters. *Institut f ur Experimentalphysik, Universit at Hamburg*, 2007.

[7] R Brun and F Rademakers. ROOTan object oriented data analysis framework. *Nuclear Instruments and Methods in Physics Research Section A: Accelerators, Spectrometers, Detectors and Associated Equipment*, 389(1):81–86, 1997.

[8] N Cabibbo. Unitary symmetry and leptonic decays. *Physical Review Letters*, 10(12):531, 1963.

[9] CERN SPS, http://sba.web.cern.ch/sba/. *Short Introduction to the use of the H6 beam*, 2000.

[10] ckm fitter group. CKM 2014 conference. In *Preliminary results as of Summer 2014*, 2014.

[11] DESY, http://eutelescope.web.cern.ch/. *EUTelescope, A Generic Pixel Telescope Data Analysis Framework*, 2012.

Bibliography

[12] M Friedl. *The CMS silicon strip tracker and its electronic readout.* PhD thesis, Wien TU, 2001.

[13] M Friedl, H Aihara, T Arakawa, Y Asano, T Aso, A Bakich, M Barbero, T Browder, MC Chang, Y Chao, et al. Belle silicon vertex detector for the super B factory. *Nuclear Instruments and Methods in Physics Research Section A: Accelerators, Spectrometers, Detectors and Associated Equipment*, 569(1):37–40, 2006.

[14] M Friedl, T Bergauer, A Frankenberger, I Gfall, C Irmler, and M Valentan. The Belle II silicon vertex detector readout chain. *Journal of Instrumentation*, 8(02):C02037, 2013.

[15] R Frühwirth. Application of kalman filtering to track and vertex fitting. *Nuclear Instruments and Methods in Physics Research Section A: Accelerators, Spectrometers, Detectors and Associated Equipment*, 262(2):444–450, 1987.

[16] R Frühwirth and A Strandlie. Track fitting with ambiguities and noise: a study of elastic tracking and nonlinear filters. *Computer Physics Communications*, 120(2):197–214, 1999.

[17] F Gaede, T Behnke, N Graf, and T Johnson. LCIO-A persistency framework for linear collider simulation studies. *arXiv preprint physics/0306114*, 2003.

[18] SL Glashow and S Weinberg. Breaking chiral symmetry. *Physical Review Letters*, 20(5):224, 1968.

[19] T Hayakawa et al. Performance tests of a full scale prototype of the Belle II TOP counter with cosmic muons and 2.1 GeV/c positron beam. *Nuclear Instruments and Methods in Physics Research Section A: Accelerators, Spectrometers, Detectors and Associated Equipment*, 766:255–258, 2014.

[20] RE Kalman. A new approach to linear filtering and prediction problems. *Journal of basic Engineering*, 82(1):35–45, 1960.

[21] M Kobayashi and T Maskawa. CP-violation in the renormalizable theory of weak interaction. *Progress of Theoretical Physics*, 49(2):652–657, 1973.

[22] J Maxwell. A dynamical theory of the electromagnetic field. *Philosophical transactions of the Royal Society of London*, 155:459–512, 1865.

[23] MissMJ. Standard model of elementary particles — wikipedia, the free encyclopedia, 27 June 2006. [Online; accessed 15-July-2015].

[24] Y Nir. 13. CP-violation in the quark sector.

[25] E Noether. Invariante variationsprobleme, nachr. d. könig. gesellsch. d. wiss. zu göttingen, math-phys. klasse (1918) 235–257. *English Reprint: physics/0503066, http://dx. doi. org/10.1080/00411457108231446*, page 57, 1918.

[26] AD Sakharov. Violation of CP invariance, C asymmetry, and baryon asymmetry of the universe. *JETP lett.*, 5:24–27, 1967.

[27] SENSIRION AG, SENSIRION AG Laubisruetistrasse 50 CH-8712 Staefa ZH Switzerland. *Application Note Dew-point Calculation*, 2006.

[28] R Turchetta. Spatial resolution of silicon microstrip detectors. *Nuclear Instruments and Methods in Physics Research Section A: Accelerators, Spectrometers, Detectors and Associated Equipment*, 335(1):44–58, 1993.

[29] M Valentan. *The Silicon Vertex Detector for b-tagging at Belle II*. PhD thesis, Wien TU, 2013.

[30] B Verlaat and AP Colijn. CO2 cooling developments for HEP detectors. In *18th International Workshop on Vertex detectors,(VERTEX-2009), The Netherlands, PoS*, volume 31, 2009.

[31] L Wolfenstein. Parametrization of the Kobayashi-Maskawa matrix. *Physical Review Letters*, 51(21):1945, 1983.

[32] CS Wu, E Ambler, RW Hayward, DD Hoppes, and R Pl Hudson. Experimental test of parity conservation in beta decay. *Physical review*, 105(4):1413, 1957.

[33] B Wuerkner. Beam test data analysis and resolution studies for the Belle II silicon vertex detector. Master's thesis, Vienna University of Technology, 2016.

[34] H Yin. Readout software for the Belle II silicon vertex detector and test beam data analysis. Master's thesis, Vienna University of Technology, 2016.